

Multi-axis compliant mechanism-based nanopositioner for multi-mode mechanical testing of carbon nanotubes

by

Kevin Lin

B.S., Mechanical Engineering  
University of California, Berkeley, 2003

Submitted to the Department of Mechanical Engineering  
in Partial Fulfillment of the Requirements for the Degree of  
Master of Science in Mechanical Engineering

at the

Massachusetts Institute of Technology

February 2006

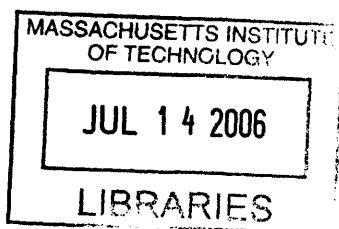
© 2006 Massachusetts Institute of Technology  
All rights reserved.



Signature of Author: .....  
Department of Mechanical Engineering  
December 20, 2005

Certified by: .....  
Martin L. Culpepper  
Rockwell International Assistant Professor of Mechanical Engineering  
Thesis Supervisor

Accepted by: .....  
Lallit Anand  
Chairman, Department Committee on Graduate Students



*This page is intentionally left blank.*

Multi-axis compliant mechanism-based nanopositioner for multi-mode mechanical testing of carbon nanotubes

by

Kevin Lin

Submitted to the Department of Mechanical Engineering on  
December 20, 2005 in Partial Fulfillment of the  
Requirements for the Degree of Master of Science in  
Mechanical Engineering

## **ABSTRACT**

This thesis documents the design of a multi-axis nanopositioner that addresses a need for carbon nanotube (CNT) instrumentation that is capable of multiple modes of mechanical testing. This nanopositioner is a solution to the need to quantify the mechanical properties of CNTs with the appropriate modes of testing, such as simultaneous bending and tensile loading. This information is important as it is required to test and better understand the properties of CNTs before and after they are used in micro/nano-structures. The multi-axis nanopositioner will be integrated as one of the core components in a new CNT instrument that is presented in this thesis.

The nanopositioner is a compliant mechanism-based device designed that is to induce precise nanometer-level deformations in CNTs within a scanning electron microscope (SEM). The design presented in this thesis is a 4-axis prototype of a 6-axis version. The 4-axis nanopositioner was able to demonstrate over one micron range of motion in multiple axes with 10 nm resolution and repeatability. The nanopositioner was specifically designed to fit inside an SEM like an ordinary sample.

Thesis Supervisor: Martin L. Culpepper III

Title: Rockwell International Assistant Professor of Mechanical Engineering

*This page is intentionally left blank.*

# ACKNOWLEDGEMENTS

I would like to first start by thanking the wonderful graduate students who make up the Precision Compliant Systems Laboratory at MIT. You have helped me and challenged me in ways that have made me wiser, stronger, and overall, a better person. In the process, we have developed a life-long friendship.

A special thank you goes to my dearest friend Sungyon who never gave up on me even when I had. Thank you for being there for me during difficult times.

I would like to thank Professor Martin Culpepper for giving me this opportunity to grow in an environment that produces character. You have pushed me and challenged me more than ever before in my life, and from that, I have learned more than I could have ever imagined about engineering, life, and myself.

I would like to thank my mother who never failed to help me make sense of my life and to see the bigger picture. Her happiness rests in my wellbeing, and I will always cherish that love she gives me.

Most of all, I would like to thank my father, who never asked anything from me except that I listen to my heart and live my life with passion. He has since passed on, but I still keep my promise. Thoughts of him are never far from me.

*This page is intentionally left blank.*

# TABLE OF CONTENTS

ABSTRACT.....	3
ACKNOWLEDGEMENTS.....	5
TABLE OF CONTENTS.....	7
LIST OF FIGURES.....	11
LIST OF TABLES.....	17
1 INTRODUCTION.....	19
1.1 Purpose of this research.....	19
1.2 Background.....	24
1.2.1 Carbon Nanotubes.....	24
1.2.2 Compliant Mechanisms.....	24
1.2.3 CNT Instrumentation.....	26
1.3 Hypothesis.....	33
1.4 Contributions.....	36
2 Design Requirements for 6-Axis SEM-Compatible Positioner.....	39
2.1 Design Constraints.....	39
2.2 Functional Requirements.....	41
2.3 Design Strategies.....	44
2.3.1 Motion Mechanism Design Strategy.....	45
2.3.2 Actuator Selection.....	46
2.4 Design Conception and Selection.....	49
2.4.1 Six-Axis Compliant Mechanism Design.....	49
2.4.2 Compliant Transmission Mechanism Design.....	54
2.4.3 Actuation Tab Constraint Design.....	55
2.4.4 Component Interface Design.....	56
2.5 Summary of Design.....	59
3 Modeling, Simulation, and Optimization of Selected Concepts.....	61

3.1	Constructing an Error Budget for Concept Verification.....	62
3.2	Compliant Transmission Mechanisms (Mechanical De-amplifiers) .....	65
3.2.1	Out-of-Plane Compliant Transmission Mechanism.....	66
3.2.1.1	Diamond-Shaped De-amplifying Mechanism .....	66
3.2.1.2	Bent Out-of-Plane Transmission Flexure .....	69
3.2.2	In-Plane Compliant Transmission Mechanism.....	69
3.3	System Stiffness Analysis and Modeling .....	70
3.3.1	Out-of-Plane Stiffness.....	70
3.3.1.1	Transmission Mechanism Stiffness .....	72
3.3.1.2	Contact Stiffness .....	72
3.3.2	In-Plane Stiffness .....	75
3.4	Dynamic Modeling of the System .....	77
3.5	Summary of Design .....	79
4	Fabrication and Assembly of a Prototype .....	81
4.1	Fabrication Method Selection.....	81
4.2	Waterjet Cutting.....	83
4.3	Assembly.....	84
5	Performance Characterization .....	87
5.1	Review of Performance Metrics .....	87
5.2	Metrology System Design.....	88
5.3	Experimental Procedure.....	92
5.4	Metrology Limitations and Issues.....	93
5.4.1	Mechanical Limitations .....	93
5.4.2	Environmental Limitations .....	94
5.4.3	Electrical Limitations.....	96
6	Performance Characterization of Nanopositioner .....	99
6.1	Initial Results for Completely Assembled Nanopositioner .....	99
6.2	Out-of-Plane Module Results .....	100
6.2.2	Hysteresis.....	101
6.3	In-Plane Module Results.....	104
6.3.2	Range .....	104



6.3.3	Resolution and Repeatability .....	107
6.3.4	Accuracy .....	110
6.4	Assembled Nanopositioner Results .....	110
6.4.1	Performance Results .....	110
6.4.2	Dynamic Behavior .....	112
7	Research Contributions and Future Work .....	113
7.1	Research Impact.....	113
7.2	Future Work.....	114
	REFERENCES .....	116
	Appendix A.....	119
	Appendix B.....	129
	Appendix C.....	131

*This page is intentionally left blank.*

# LIST OF FIGURES

Figure 1.1 : Labeled diagram of different components of proposed CNT testing instrumentation. .....	21
Figure 1.2 : Potential CNT-based micro-CM four-bar structure that requires multi-axial testing to fully characterize its mechanical properties.....	23
Figure 1.3 : Diagram of (a) SWCNT structure [3] and (b) TEM image of SWCNT that is bent $110^\circ$ [4]. .....	24
Figure 1.4 : Examples of micromechanical devices that take advantage of CMs to achieve their motion: (A) Bi-stable micro-CM [14] and (B) Micro-HexFlex.....	25
Figure 1.5 : CNT testing methods/equipment demonstrated by Dong et al. that used multiple AFM probe tips to measure mechanical CNT properties [19].....	30
Figure 1.6 : MEMS CNT testing instrument developed by Williams et al. that used compliant flexures as gauge springs to measure CNT deformation [23].....	31
Figure 1.7 : Physik Instrumente's smallest nanopositioner that has sub-nanometer resolution and three-axis motion. The nanopositioner's height is about 50 mm tall (Courtesy of PI (Physik Instrumente), <a href="http://www.pi.ws">www.pi.ws</a> ).....	32
Figure 1.8 : CAD model of assembled positioner in isometric view.....	35
Figure 1.9 : CAD model of positioner in exploded view.....	36
Figure 2.1 : Diagram of simultaneous actuation forces in the tangential direction and in the out-of-plane direction at a single actuation tab on the HexFlex.....	50

Figure 2.2 : Diagram of potential sliding and misalignment problems when actuating a single tab using two orthogonal piezo-electric actuators. .... 51

Figure 2.3 : Schematic of HexFlex component and its in-plane motion produced by three grounded nodes and three in-plane displacements at actuation tabs..... 53

Figure 2.4 : Schematic of out-of-plane CM component placed in series with in-plane deamplification CM. The in-plane displacement input produces an out-of-plane output displacement. .... 54

Figure 2.5 : Diagram of compliant out-of-plane transmission mechanisms. The transmission mechanism consists of two perpendicular components: (1) diamond-shaped CM and (2) half diamond CM. .... 55

Figure 2.6 : Diagram of in-plane flexures that allow the actuation tabs of the HexFlex to move unconstrained in the radial direction while transmitting tangential displacements from the actuators. .... 56

Figure 2.7 : Close-up view of HexFlex actuation tab to the in-plane module interface. The actuation tab is a triangular slot that constrains the dowel pin in in-plane directions. .... 57

Figure 2.8 : Close-up view of actuator to device interface using a precision ground dowel pin to ensure consistent and proper preloaded installation of the actuator. .... 58

Figure 3.1 : 2-D Diagram of the different coordinate systems (CSs) used to represent the different critical components of the system for the error budget. The first half of the error loop starts from the nanopositioner’s end-effector (CS9) and traces through the different CSs to the e-beam lens (CS1). The second half of the error loop starts from target sample (CS10) and traces back to the e-beam lens (CS1). .... 63

Figure 3.2 : Plot of the error budget results for 100 simulation trials. The results plot the error vector components from end-effector to target sample..... 65

Figure 3.3 : Labeled diagram of the rigid link model for the diamond-shaped shaped mechanism.  
..... 67

Figure 3.4 : Plot of the transmission ratio as a function of the primary internal quadrant angle of the rigid link diamond-shaped mechanism and of the FEA model..... 68

Figure 3.5 : Network of springs representing the stiffness of components involved with out-of-plane motion of the system. .... 71

Figure 3.6 : Diagram of Hertzian line contact that includes the variables used in Equation 3.9 to 3.13..... 73

Figure 3.7 : Network of springs representing the stiffness of components involved with in-plane motion of the system. The corresponding equivalent stiffness is also shown. .... 76

Figure 3.8 : Diagram of the mass-spring system used to approximate the first mode resonant frequency of the device. The mass represents the in-plane motion layer of the device and the springs represent the out-of-plane flexures used to transmit out-of-plane motion to the in-plane motion layer. .... 78

Figure 3.9 : Bode plot of the mass-spring-damper model of the device. The Bode plot reveals the first mode resonant frequency at the peak, and also shows the dynamic response at different frequencies. .... 79

Figure 4.1 : Photograph of waterjet cutting of aluminum in-plane motion component for the nanopositioner. The smallest cut feature size is the same as the waterjet beam diameter..... 84

Figure 5.1 : Photograph of metrology system conducting experiments on the nanopositioner. The system includes the capacitance probes, the capacitance probe stages, the target piece, the capacitance probe driver, and the data acquisition system. .... 89

Figure 5.2 : Drawing of (a) the metrology stage used to position the 6 capacitance probes to measure 6-axis motion and (b) the triangular target piece with chamfered corners.....	90
Figure 5.3 : Schematic of the capacitance probes relationship with respect to the target piece and to the global coordinate system: (a) top view of in-plane probes and target piece, (b) side view of out-of-plane probes and target piece.....	91
Figure 5.4 : Photograph of the thermally insulating box that covered the metrology system and the nanopositioner during experimentation. ....	95
Figure 5.5 : Comparison of temperature fluctuation with and without the thermally insulated box. The fluctuation is reduced to $\pm 0.2$ C using the box and the mean value is stabilized. ....	96
Figure 5.6 : Observed electrical noise from the metrology system that followed a random distribution with a standard deviation of 4.1 nm at the high resolution setting.....	97
Figure 5.7 : Observed difference between desired input voltage and actual input voltage. ....	98
Figure 6.1 : Measured out-of-plane range data from a stepping actuation cycle of 10 V increments at 2 second intervals. The hysteresis is a function of increasing/decreasing applied voltage and magnitude of applied voltage. ....	102
Figure 6.2 : Overlapped hysteresis curves from two sources: (1) range data, and (2) smooth ramp actuation function. The hysteresis is confirmed by this plot to be function of applied voltage and voltage history.....	103
Figure 6.3 : Displacement motion in X-axis and associated parasitic errors.....	105
Figure 6.4 : Displacement motion in Y-axis and associated parasitic errors.....	105
Figure 6.5 : Displacement motion in $\theta_z$ -axis and associated parasitic errors. ....	105

Figure 6.6 : Close-up picture of surface finish of target piece after waterjet cutting and hand polishing.....	108
Figure 6.7 : Raw capacitance probe data from two in-plane probes that show the response to an increasing staircase input function.....	109
Figure 6.8 : Resulting x-direction response after transforming the capacitance probe data into the global coordinate system.....	109
Figure 6.9 : Diagram of taper due to waterjet cutting in the half-diamond flexure that produces large parasitic errors in the global x and y-directions.....	111
Figure 6.10 : Resonance test data that was sampled at 1 kHz transformed to the frequency domain using FFT.....	112
Figure A.1 : Engineering drawing of out-of-plane motion component layer. ....	120
Figure A.2 : Engineering drawing of in-plane component layer. ....	121
Figure A.3 : Engineering drawing of half-diamond flexure used for out-of-plane motion. ....	122
Figure A.4 : Engineering drawing of support flexures for guiding out-of-plane motion. ....	123
Figure A.5 : Engineering drawing for HexFlex device that was adapted for the nanopositioner. ....	124
Figure A.6 : Engineering drawing of main metrology stage component.....	125
Figure A.7 : Engineering drawing of bottom component of target piece. ....	126
Figure A.8 : Engineering drawing of top component of target piece. ....	127

Figure A.9 : Engineering drawing of assembled nanopositioner..... 128

Figure B.1 : (Top) Photograph of the completely assembled nanopositioner. (Bottom) Photograph of the in-plane and out-of-plane sub-assemblies..... 129



# LIST OF TABLES

Table 1.1 : Performance-related functional requirements for high resolution nanopositioner that will provide the necessary multi-mode testing data required for integrating CNTs into nanomechanical devices.....	22
Table 1.2 : List of four successful CNT instruments that have characterized mechanical CNT properties. All four used an AFM probe as an end effector to manipulate individual CNTs to setup the experiment, while Yu and Dong also used the AFM to conduct the experiments. ....	28
Table 1.3 : Summary of the advantageous and disadvantageous methods after assessing CNT instruments and nanomanipulators for the purpose of this research.....	33
Table 2.1 : Table of major design constraints for precision positioner. ....	40
Table 2.2 : Nanopositioner design functional requirements listed with their specifications and the reasoning for them. ....	42
Table 2.3 : Pugh chart comparing potential motion mechanisms for the nanopositioner. Conventional rigid link mechanism was used as the baseline. ....	44
Table 2.4 : Pugh chart that compares different potential actuators to be used in compliant mechanism based system. ....	45
Table 2.5 : Key technical data for chosen stacked piezo-electric actuator from Physik Instrumente. ....	48
Table 3.1 : Summary of the different input errors and their parameters to calculate the error budget.....	64

Table 4.1 : Pugh chart comparing the three most feasible fabrication methods for making the nanopositioner..... 82

Table 5.1 : Review of performance metrics and their experimental bench top approach. .... 88

Table 6.1 : Range of motion and accompanied parasitic error motion (non-bold) associated with actuation in each of the four-axis. The parasitic errors are comparable, or larger than, the desired actuation range. The range of motion in the actuation axis is in bold. .... 100

Table 6.2 : Summary of the measured performance of the independent out-of-plane module that was separated from the in-plane module. The desired metric values are adjusted for the range and resolution due to the absence of flexure supports ..... 101

Table 6.3 : Experimental data obtained from the in-plane module using 6 capacitance probes.104

# CHAPTER 1

## 1 INTRODUCTION

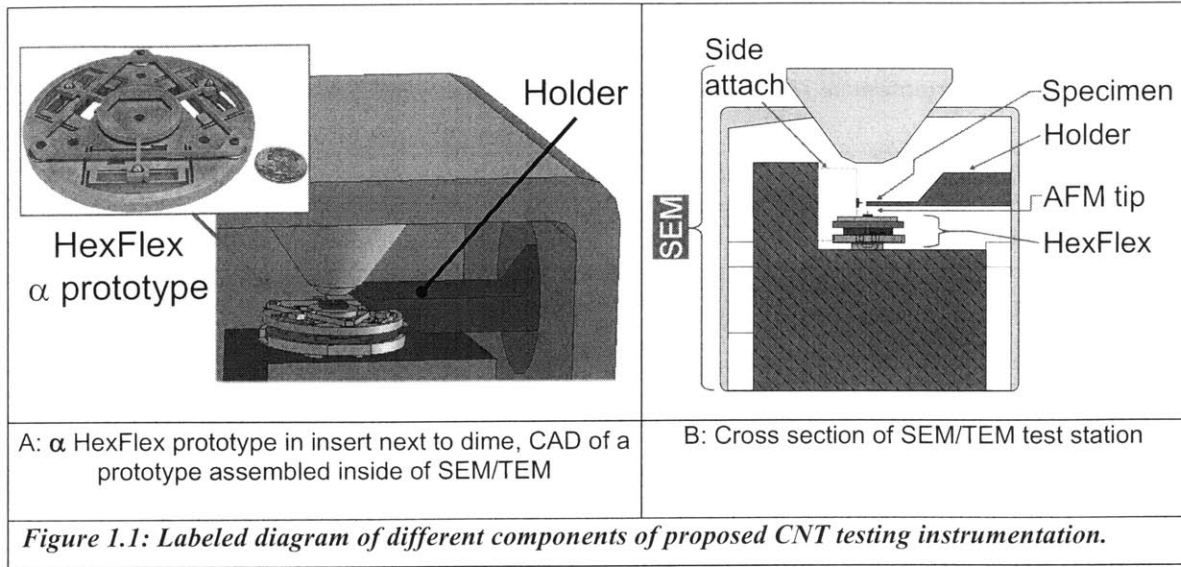
### 1.1 Purpose of this research

The purpose of this research is to learn how to design a multi-axis nanopositioner that has the necessary degrees of freedom and sensitivity to conduct multi-mode mechanical testing of Carbon nanotubes (CNTs). These capabilities are necessary to obtain knowledge about their multi-axis load-displacement characteristics. These characteristics are required for successful integration of CNTs into useful nanomechanical compliant mechanisms (CMs) where the CNT is used as the deforming element. The reasons for pursuing a completely new instrumentation system are the following:

1. Existing CNT testing instruments focus on single mode testing (e.g. tensile, compressive, torsional, and bending). The mechanical properties of CNTs are not yet understood well enough to assume that superposition of single mode behavior can accurately predict multi-mode behavior required in CNT-based CMs, e.g. bending plus tension.

2. The operation of the majority of the CNT testing instruments is time consuming and difficult, because they rely on the use of atomic force microscope (AFM) probe tips to position and mount individual CNTs for each experiment.
3. Many instruments require major modifications to the scanning electron microscope (SEM) in which the experiment is conducted, e.g. the removal of original positioning stage during setup. These modifications would be impractical for a SEM that is shared among different research efforts.

This research looks at developing a new CNT instrument that can achieve multi-mode mechanical testing within a single experimental setup, while requiring minimal modifications to the SEM. The approach is to use as many of the original SEM components, such as the positioning stage and sample mounts, as part of the new instrument. Also, this work aims to minimize the number of additional custom components in the instrument, such as the multi-axis nanopositioner and the micro CNT test sample. A preview of the proposed instrumentation system is shown in Figure 1.1. The system is described later in the section in more detail.



This research effort is focused on creating the system's nanopositioner. At the heart of this research is a multi-scale design problem that requires proper cross-scaling between the macro-scale (the nanopositioner) to the nano-scale (the CNT). The design problem translates into the following functional requirements for the nanopositioner that are listed in Table 1.1.

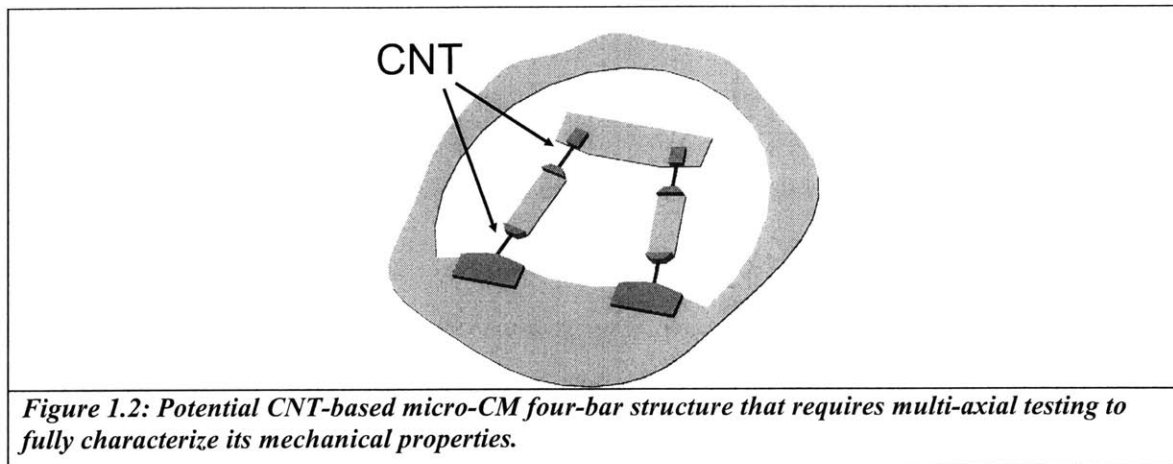
**Table 1.1: Performance-related functional requirements for high resolution nanopositioner that will provide the necessary multi-mode testing data required for integrating CNTs into nanomechanical devices.**

<b>Functional Requirement</b>	<b>Specification</b>	<b>Achieved</b>
Multi-axis motion	6 axis	4 axis
Device Volume	73 mm diameter 20 mm tall	73 mm diameter 20 mm tall
Resolution ( $\Delta_x, \Delta_y, \Delta_z$ ) ( $\theta_x, \theta_y, \theta_z$ )	1 nm 1 $\mu$ rad	1-10 nm 0.5 $\mu$ rad
Range ( $\Delta_x, \Delta_y, \Delta_z$ ) ( $\theta_x, \theta_y, \theta_z$ )	1 $\mu$ m 150 $\mu$ rad	0.5 – 4.5 $\mu$ m 120 $\mu$ rad
Repeatability	1 nm	1- 10 nm
Natural Frequency	> 1 kHz	> 1 kHz

In general, the CNTs have nano-scale characteristic dimensions that require the instrument measuring them to scale its sensitivity down accordingly; thus, the nanopositioner must have nanometer resolution and repeatability. Furthermore, CNTs can have up to millimeter length dimensions that require a comparable large range of motion from the instrument. Further reasons behind the quantitative values for the functional requirements are explained in greater detail in Chapter 2.

Current technology in nanopositioners cannot match all the functional requirements this research seeks to fulfill. Primarily, the 6-axis requirement and the device envelope requirement are the main shortcomings of current nanopositioners. This shortcoming is a result of their conventional approach of stacking different axial components together to achieve motion in the desired number of axes. As a result, this research looks to use a special 6-axis CM developed by Anderson and Culpepper at MIT, the HexFlex, for building the 6-axis nanopositioner [1].

The results from this research contribute to the potential production of CNT-based building-blocks for nanomechanical devices. For instance, CNTs may be used as compliant machine elements, e.g. flexure hinges. These elements may then be used to create micro-compliant mechanisms (micro-CMs) as shown in Figure 1.2.



These elements deform and therefore undergo multi-axis loading. Knowledge of their multi-axis load-displacement characteristics is needed for engineering, design, and testing work. As result to a lack of this knowledge, the realization of CNT-based nano-scale compliant mechanisms faces a fundamental barrier in terms of measuring CNT deformation characteristics for micro-CMs. The research addresses this barrier by:

- Quantifying the CNT instrument requirements, specifically the nanopositioner
- Generating and selecting design concepts for CNT instrument, and in turn, the nanopositioner
- Synthesizing and fabricating the nanopositioner for the CNT instrument
- Validating the nanopositioner design process and performance models to satisfy testing requirements
- Suggesting improvements for the nanopositioner and future work.

## 1.2 Background

### 1.2.1 Carbon Nanotubes

CNTs have desirable mechanical properties for acting as the deformable element in CMs due to their unique atomic geometry. CNTs are single molecules of cylindrical graphene sheets that have nano-scale diameters and micro-to-meso-scale lengths [2]. Figure 1.3 shows a diagram and transmission electron microscope (TEM) image of a single-walled carbon nanotube (SWCNT).

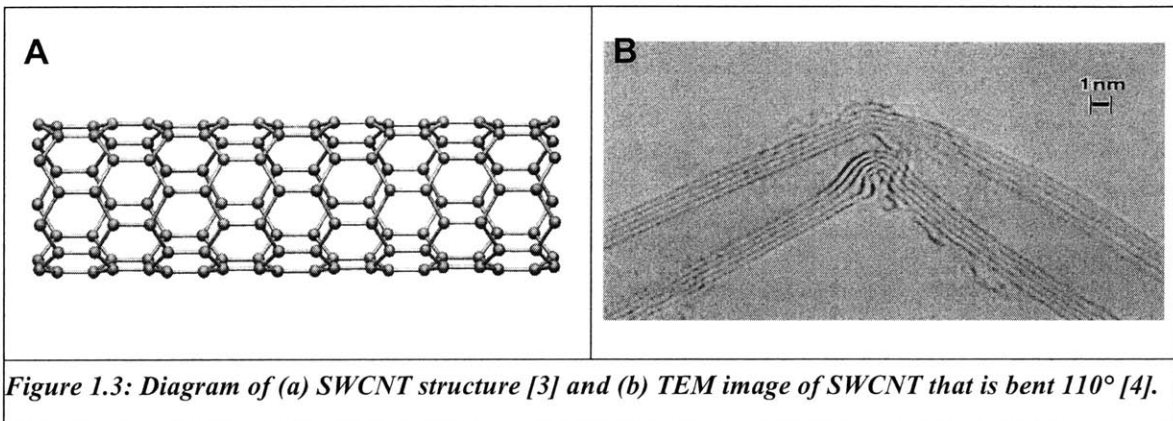


*Figure 1.3: Diagram of (a) SWCNT structure [3] and (b) TEM image of SWCNT that is bent 110° [4].*

The covalent  $sp^2$  bonds between the carbon atoms in the CNT lattice are responsible for their exceptional strength as well as their high Young's modulus. The modulus is typically measured at approximately 1 TPa [5-7]. CNTs can endure reversible bending angles of 110 degrees [8-10]. They may also exhibit tensile strain up to 16% [11]. Figure 2(b) shows a TEM image of a multi-walled carbon nanotube (MWCNT) experiencing a large bending angle. They have been described to be a hundred times stronger than steel and as stiff as diamond [12]. Their stiffness, strain, and strength are desirable mechanical properties for mechanisms that require bending to produce motion.

### 1.2.2 Compliant Mechanisms

CMs are similar to conventional rigid link mechanisms in that they both transfer motion, force, or energy. However, CMs derive their motion characteristics from the elastic deformation of



some or all of the mechanism's components. This difference gives CMs the advantages of (1) reducing friction-hysteresis position inaccuracies, (2) minimizing joint wear and its effect on device lifetime, and (3) eliminating joint clearances that affect accuracy [13]. CMs can be made monolithically, thereby reducing fabrication-related costs. The preceding benefits make CMs a good choice for high-precision, high reliability, and low cost applications wherein assembly is either difficult or expensive. Micromechanical devices are good examples where assembly is difficult and expensive, because they require microfabrication processes that are complex and delicate. In turn, CMs are popular designs for these small-scale mechanical devices. Examples of micro-CMs are shown in Figure 1.4 to illustrate micromechanical devices that use CMs rather than rigid-link mechanisms at that scale to direct motion. The reasoning for using CMs on the micro-scale can also be transferred to the nano-scale for nanomechanical systems.

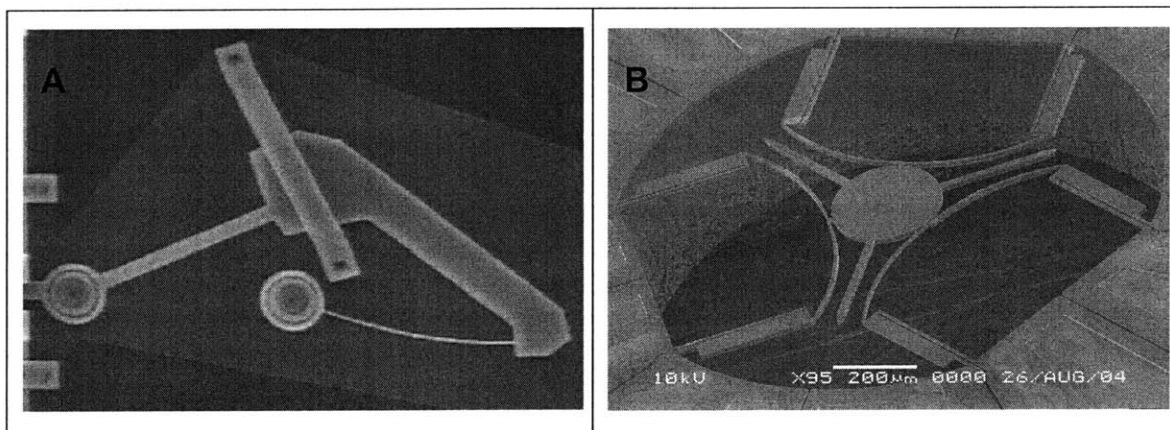


*Figure 1.4: Examples of micromechanical devices that take advantage of CMs to achieve their motion: (A) Bi-stable micro-CM [14] and (B) Micro-HexFlex.*

CMs also have disadvantages compared to conventional rigid link mechanisms. The design of compliant mechanisms requires simultaneous solution of kinematic and elasto-mechanic behaviors [14]. Therefore, a complete understanding of the deformation and stiffness characteristics of CNTs is required to enable CNT-based CMs. In addition, the range of motion

in CMs is generally limited to a few percent of their overall size. CNTs are desirable as nano-scale compliant elements, because they can endure large reversible deformations that would increase the CM's range from a few percent of device size to perhaps tens of percent of device size. It is critical to possess instrumentation that can characterize this load-displacement behavior. Without this capability, engineering design of nano-scale CMs will not be possible.

### **1.2.3 CNT Instrumentation**

There are a range of CNT instruments that are designed to quantitatively measure the mechanical, electrical, and chemical properties of CNTs. However, for the purpose of this research, current CNT instruments cannot:

1. Conduct the multiple modes of mechanical testing that are necessary to characterize the CNTs well enough to implement them in micro/nano-scale CMs, e.g. tension plus bending.
2. Be installed into conventional SEMs without requiring major modifications, primarily, the removal of the original translation stage. This prevents the implementation of the instrument when a SEM cannot be dedicated exclusively to the CNT instrumentation.
3. Conduct experiments reliably and efficiently, because the instruments rely on the unpredictable integrity of Van der Waal forces to interface the CNT to the instrument. The integrity of Van der Waal forces depends on several parameters that are difficult to precisely control.

Although the CNT properties and the methods to measure them vary among different CNT instruments, they all deal with the challenge of interfacing with CNTs' micro/nano-scale dimensions. Developing CNT instruments is especially challenging, because it involves scaling

down the geometry to the nano-scale, but at the same time, having to deal with a change in the physics. At the nano-scale, the electrostatic and surface forces are on the same order as elastostatic forces, while gravitational forces are negligible [15]. This section will also examine how other CNT instruments approach this multi-scale problem and addresses their weaknesses and limitations.

Operating CNT instruments to measure mechanical properties is time consuming and difficult, because they depend heavily on AFM probe tips to manipulate individual CNTs. Furthermore, this limits the instruments to conduct a single mode of mechanical testing, most commonly tensile and compressive testing. The integrity of an AFM probe tip's connection to a CNT is dependent on Van der Waal forces that are a function of the contact surface, the surfaces' material properties, and the angle of approach between the surfaces [16, 17]. Therefore, multi-mode mechanical testing has been limited by how well the AFM probe tip interfaces with the CNT. This research aims to find a solution to this limitation in order to test with simultaneous bending and tensile loading, because it simulates common stresses and strains induced in CMs.

Four different instruments that are commonly used to measure mechanical CNT properties are listed with their respective creators in Table 1.2. They reiterate the reliance on AFM probe tips, but also shed light on positive attributes they possess.

*Table 1.2: List of four successful CNT instruments that have characterized mechanical CNT properties. All four used an AFM probe as an end effector to manipulate individual CNTs to setup the experiment, while Yu and Dong also used the AFM to conduct the experiments.*

Yu et al.	<p><b>Description:</b> Double Cantilever instrument that conducted tensile testing to obtain stress-strain plots of CNTs.</p> <p><b>Advantage:</b> The use of two independently controlled AFM probe tips allowed multi-axis manipulation.</p> <p><b>Disadvantage:</b> AFM for setup and experimentation made this instrument very time consuming to operate. Reliance on Van der Waal forces limited the reliability of the boundary condition of the CNT.</p>
Dong et al.	<p><b>Description:</b> Three cantilever plus substrate instrument that accomplished both compressive bending and tensile testing of MWCNTs.</p> <p><b>Advantage:</b> Conducted two modes of mechanical testing. The use of independently controlled AFM probe tips allowed multi-axis manipulation. Use of substrate and additional AFM probe tips helped decrease setup effort.</p> <p><b>Disadvantage:</b> Still limited to just 2 AFM probe tips interfacing with CNT to conduct testing. Reliance on Van der Waal forces limited reliability of the boundary condition of the CNT.</p>
Williams et al.	<p><b>Description:</b> MEMS instrument that used comb drives in series with micro-flexures to conduct uni-axial testing on CNTs.</p> <p><b>Advantage:</b> Use of MEMS comb drives induced controllable and reliable deformation of a CNT. The use of springs with specific stiffness on the order of the CNT allowed high resolution measurements.</p> <p><b>Disadvantage:</b> The instrument is specific to tensile and compressive testing modes only. Also limited by Van der Waal forces that kept the CNT mounted to the MEMS device. Use of AFM probe tips to mount the CNT is time consuming and difficult.</p>
Papadakis et al.	<p><b>Description:</b> Micro-scale instrument where CNT is integrated into the instrument during the microfabrication process.</p> <p><b>Advantage:</b> Use of microfabrication to customize the interface between the CNT and the instrument allowed better mounting of CNT that was specific to the testing mode. Testing setup easily duplicated using batch processing.</p> <p><b>Disadvantage:</b> Still requires the use of AFM to initially position the CNT into position for subsequent microfabrication processes and for applying torsional testing loads. Limited to a single mode of testing.</p>

A common CNT instrument design induces mechanical deformation of the CNT by physically interfacing the CNT with micro-scale structures. Atomic force microscope (AFM) probe tips are desirable structures for this, because they have tips with nanometer-level radius of curvature attached to millimeter sized cantilever arms. In addition, their variety of geometries is standardized and readily available. The deformation of the CNT is normally analyzed by images taken from an electron microscopy.

For example, Yu et al. measured the Young's modulus of CNTs and mapped out their stress-strain curves using two AFM probes to deform single CNTs inside an SEM [11, 17]. He observed the deformation of both the AFM cantilevers and the CNT from the SEM images. Similarly, Dong et al. conducted compressive buckling tests using a combination of precision stages to independently manipulate three AFM cantilever probes. He also observed the effect of the CNT from the probe forces inside an SEM [18, 19]. This instrument was also able to conduct testing of MWCNT bearing motion. Dong's method is shown in Figure 1.5.

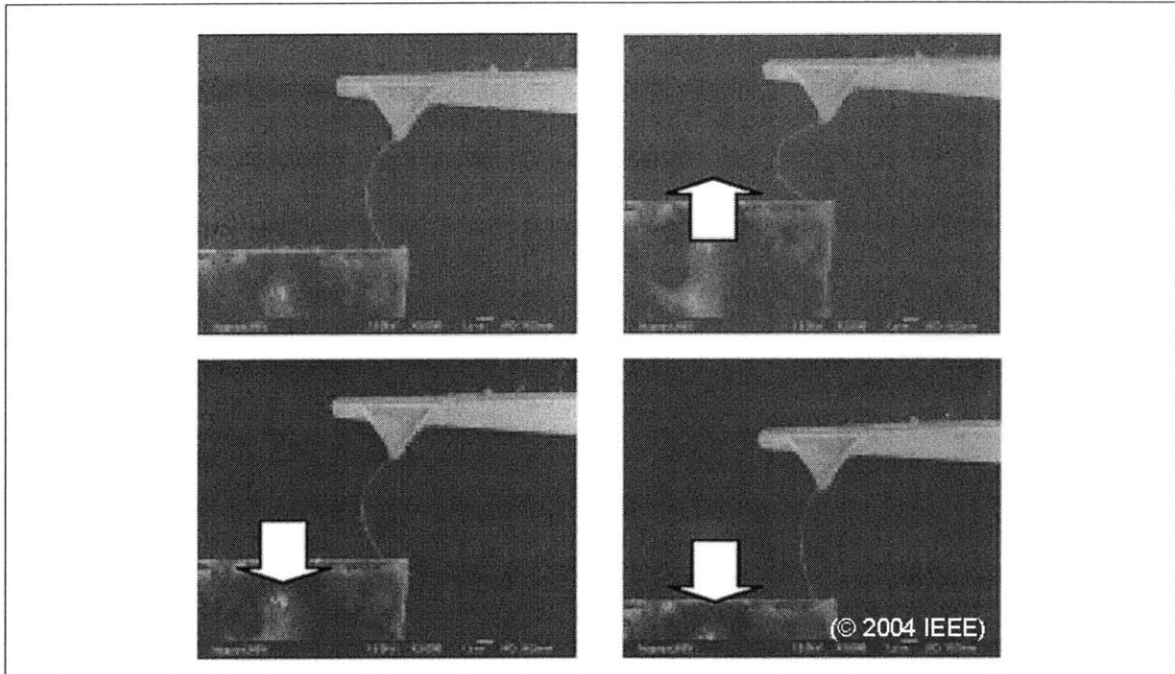


*Figure 1.5: CNT testing methods/equipment demonstrated by Dong et al. that used multiple AFM probe tips to measure mechanical CNT properties [19].*

Both methods had the disadvantage of using AFM probes for setting up the experiment as well as conducting the experiment. This made their testing process inefficient, as manipulating single CNTs is a difficult and time consuming task. More critically, the testing relied on the unpredictable integrity of the bond between the AFM probe and the CNT. On the other hand, both methods showed that independently controlled probes could potentially allow multi-axis loading on the CNT.

Both Williams et al. and Hartman et al. conducted similar experiments wherein single CNTs were connected to a MEMS flexure device to deform the CNT inside an SEM [20, 21]. By designing the flexures (springs that gauged the reaction force from the CNT) with stiffnesses on the same order as the CNT stiffness, they were able to optimize the accuracy of the data. Similarly, Papadakis et al. integrated CNTs into a torsional micro-structure by positioning the CNTs using an AFM probe and then conducting subsequent microfabrication processes [22].

The subsequent microfabrication allowed Papadakis to customize the interface between the CNT and the instrument. Although, this experimental setup had the potential to be batch processed for high volume experimentation, the individual CNT manipulation for setup bottlenecked the testing method. William's method is shown in Figure 1.6.

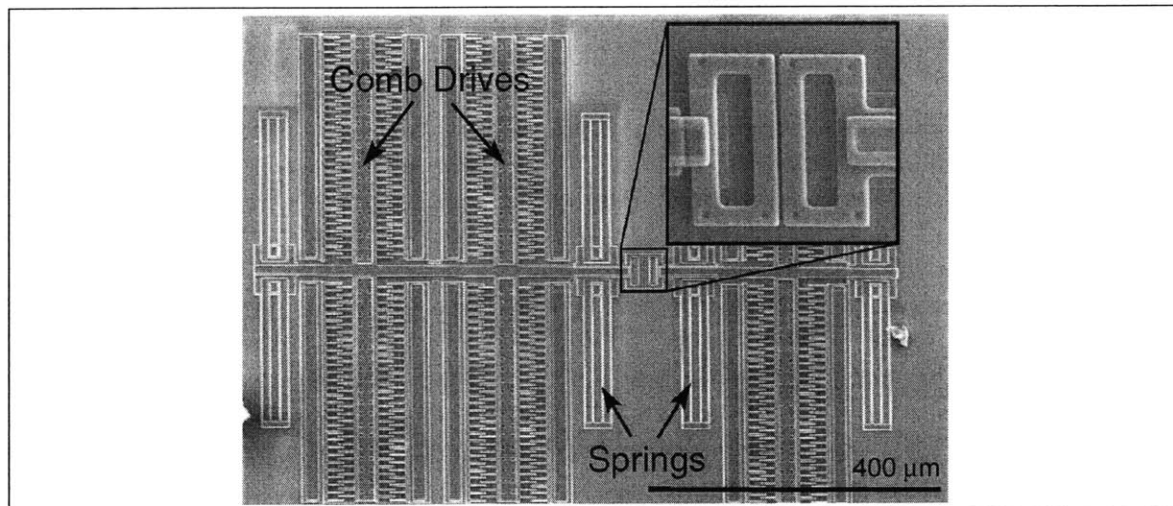


*Figure 1.6: MEMS CNT testing instrument developed by Williams et al. that used compliant flexures as gauge springs to measure CNT deformation [23].*

In general, the methods mentioned above required time consuming manipulation of single CNTs with an AFM to precisely position and secure them to other system components. In addition, they were not capable of the multi-axis testing necessary to characterize CNT-based CMs.

In addition to devices dedicated only for CNT testing, commercially available nanopositioners were also explored as possible devices that could produce the motion necessary to deform CNTs for testing. Currently, state-of-the-art nanopositioners have sub-nanometer resolution when operated in a closed-loop system. Also, they are capable of 6-axis motion. However, none of the commercial nanopositioners can satisfy the size envelope we seek. This is because commercial nanopositioners rely on stacking single-axis components in order to achieve multi-

axis motion. As a result, the height of the device becomes the limiting dimension when attempting to install the device into the SEM without removing the original SEM stage. For example, Physik Instrumente's smallest multi-axis nanopositioner, the Nanocube™, is capable of 3-axis motion, but is still over twice the allowable height for our needs. Figure 1.7 is a picture of the Nanocube from Physik Instrumente [24].

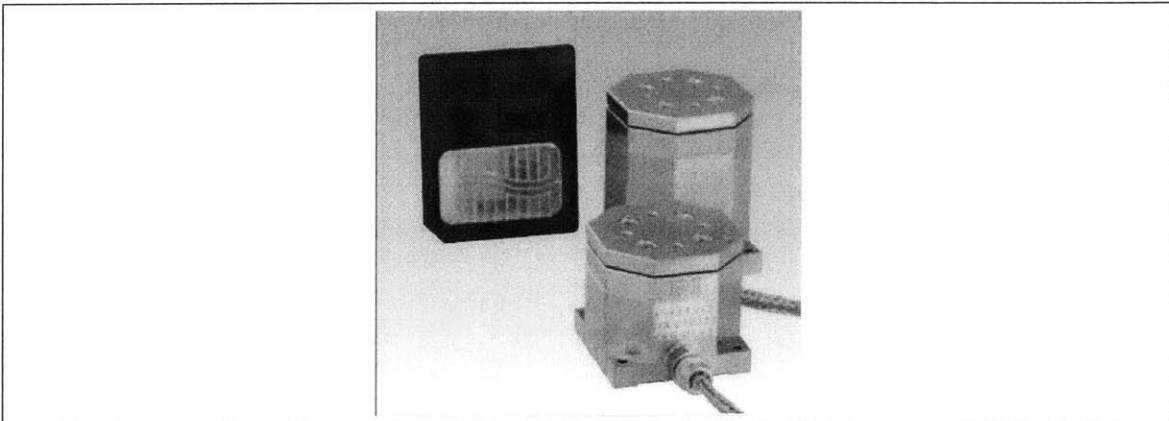


*Figure 1.7: Physik Instrumente's smallest nanopositioner that has sub-nanometer resolution and three-axis motion. The nanopositioner's height is about 50 mm tall (Courtesy of PI (Physik Instrumente), [www.pi.ws](http://www.pi.ws)).*

The assessment of CNT instruments and nanomanipulators has shown the advantages and disadvantages of the methods used to measure CNT properties. They are summarized in Table 1.3.



*Table 1.3: Summary of the advantageous and disadvantageous methods after assessing CNT instruments and nanomanipulators for the purpose of this research.*

<b>Advantageous Methods</b>	<b>Disadvantageous Methods</b>
Independently controlled probes that are capable of inducing multiple mechanical loading modes on CNTs.	Reliance on inconsistent Van der Waal forces to mount the CNTs to the instrumentation for conducting mechanical tests.
Custom fabricated microstructures that allow the designer to optimize the interface between the CNT and the instrument.	Use of AFM probe tips to manipulate individual CNTs one at a time.
Custom fabricated microstructures that allow the designer to optimize flexure gauges to match the stiffness of the CNT in order to increase the sensitivity of the instrument.	Removal of the SEM translation stage in order to install CNT instrument.
Microfabricated CNT instruments are easily mass produced using batch fabrication.	Microfabricated CNT instruments are difficult to modify and adjust once fabricated.

### 1.3 Hypothesis

As a result of the shortcomings of current CNT instruments and nanomanipulators described in the previous section, the research proposes a new instrumentation system as a solution. The new CNT instrumentation consists of the following components described below and already shown in Figure 1.1.

1. SEM for observing induced mechanical deformations of the test sample and for conducting image analysis.
2. Large range, limited resolution stage that could provide large motions for deforming the CNT test samples. This is the translation stage factory-built into the SEM.
3. Nanopositioning stage capable of providing the fine motion in 6-axes of motion required for this research's CNT testing.

4. Customized CNT test samples which interface the CNT with a microstructure that serves as a flexure gauge for measuring induced deformations of the CNT. These test samples are batch fabricated with the CNT grown into the microstructure.
5. AFM tip or end effector capable of interfacing and applying multi-axial loads to the CNT test sample.

The primary hypothesis of this research is that the HexFlex mechanism, a planar six-axis compliant mechanism, can be used as the nanopositioning component in the instruments. In other words, it is capable of simultaneously inducing multi-axis deformations to CNTs with a resolution that is meaningful to the measurement of their properties.

The HexFlex mechanism was chosen as the core component for the nanopositioner, because it provided precise 6-axis motion necessary for the CNT testing. The HexFlex's compact geometry was compatible with ordinary SEM setups, and its design was easily modified. Despite the benefits the HexFlex provided, its adaptation to become a nanopositioner that fulfilled the functional requirements was challenging in that:

1. This required a new conceptual design of the HexFlex and supporting actuation/sensing systems to meet the level of sub-nanometer requirements we are seeking
2. The nanopositioner was envelope-limited to standard SEM sample dimensions, in order for the nanopositioner to be successfully mounted upon the SEM translation stage
3. The actuators needed to be compatible with the magnetic fields and high-vacuum pressure within the SEM environment
4. The dynamic behavior of the instrument needed to reject disturbance forces so that vibrations less than the nanometer resolution are present for the device under test.

The research maps out the necessary constraints and functional requirements for a 6-axis nanopositioner suitable for integration into a larger system as a CNT instrument. The reasons for

these constraints and functional requirements are directly related to the geometry and scale of the CNT. The reasons are discussed in greater detail in Chapter 2. The metrics used to verify the positioner's success are related to how well critical design components fulfill the constraints and functional requirements.

As a first generation prototype, a bench-level 4-axis nanopositioner was tested with respect to the metrics. The 4-axis nanopositioner serves as a feasibility test for the 6-axis nanopositioner design. After the bench-level device is calibrated and tested, it will then be integrated with other components inside the SEM chamber. Figure 1.8 shows an assembled drawing in isometric view and Figure 1.9 shows an exploded view of the 4-axis nanopositioner.

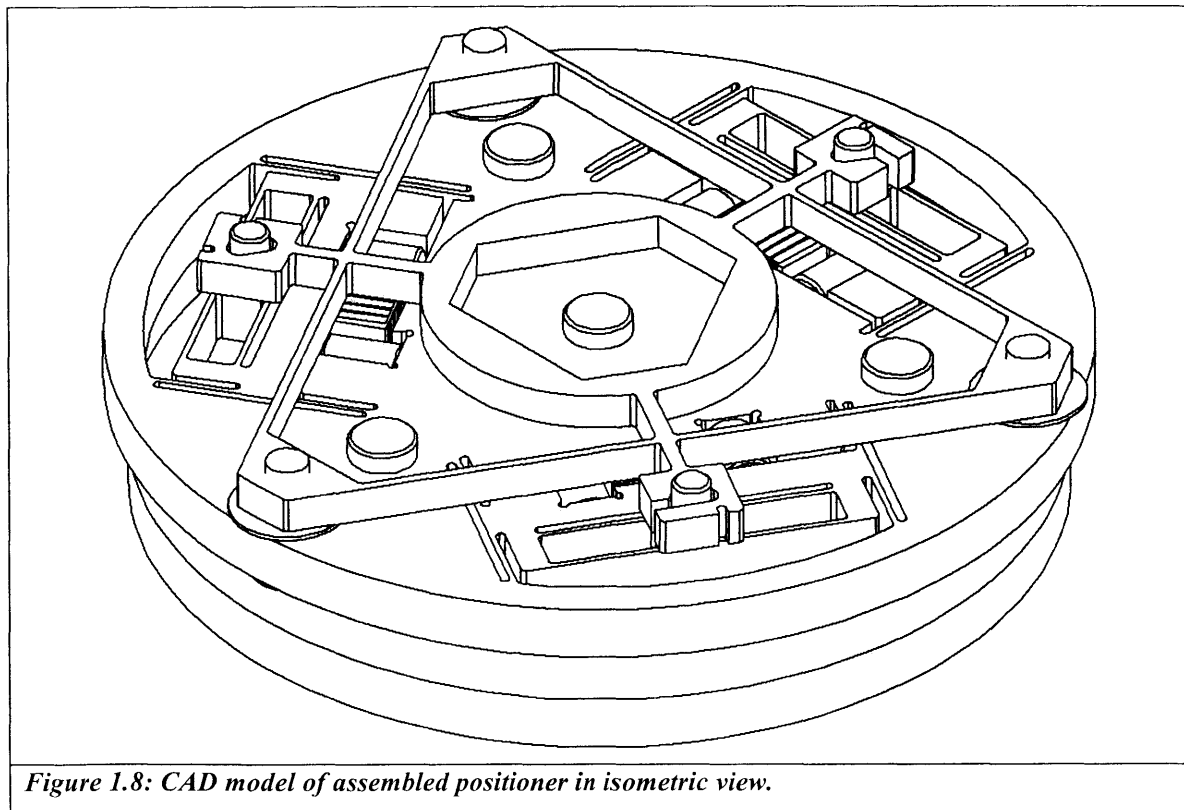


*Figure 1.8: CAD model of assembled positioner in isometric view.*

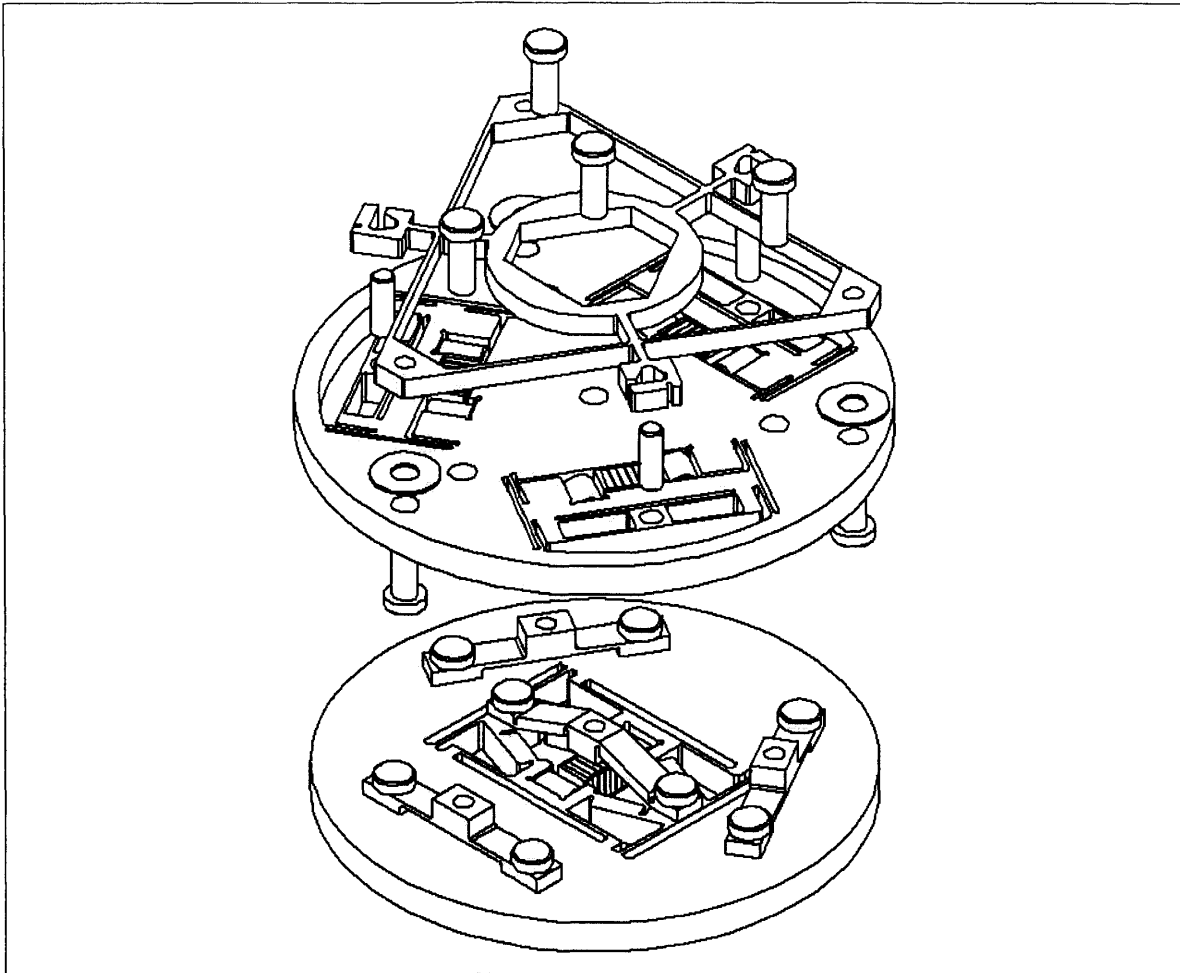


*Figure 1.9: CAD model of positioner in exploded view.*

## **1.4 Contributions**

The knowledge generated in this research includes:

1. An engineering design process for creating low cost, six-axis testing instruments for CNTs
2. A design tool that may be used to simulate and optimize the design of future instruments for custom applications.
3. Experimental validation of an instrument capable of multi-axis testing of CNTs via deformation.

Furthermore, the work accomplished in this research will contribute to the larger effort of developing the full CNT testing instrumentation. Consequently, the knowledge gained from this research must be passed on to subsequent researchers to allow successful integration and operation of the positioner within the overall system.



# CHAPTER 2

## 2 Design Requirements for 6-Axis SEM-Compatible Positioner

This chapter describes the decisions that were made during the design process. The process included determining functional requirements and constraints, creating concepts, and modeling the concepts to reach the final design. The goal of the chapter is to highlight the logic behind the critical design decisions that were made.

### 2.1 Design Constraints

Design constraints are requirements that must be met in order to achieve the design goals. For the nanopositioner design, the main constraints were related to its successful installation and operation within the SEM chamber environment. The SEM is the component in the full CNT

instrument that allows the user to observe and control the instrument. It also provides the means to measure the induced CNT deformation. The constraints and their reasoning are summarized in Table 2.1.

**Table 2.1: Table of major design constraints for precision positioner.**

<b>Constraints</b>	<b>Reason</b>
Mount inside SEM like ordinary sample 20 mm device height 72 mm diameter base	Minimize alterations or adjustments to default SEM components in order to allow easy installment/uninstallment of positioner. This is critical for SEMs that are shared and cannot be solely dedicated to being a CNT instrument.
High vacuum compatible $10^{-4}$ Torr	Minimize the introduction of contaminants into the SEM chamber from outgassed lubricants and adhesives.
Does not interfere with the magnetic field	Minimize disturbances to the e-beam focusing, which is controlled by a magnetic lens, and to the collection of rebounding electrons.
Uniform conductivity across imaged surface	Minimize charge build-up on device from e-beam imaging that leads to image degradation due to parasitic electric fields and interference with the emission of secondary electrons.

For this research, the most critical design constraint was that the multi-axis nanopositioner had to mount inside the SEM like an ordinary test sample. This attribute distinguishes the CNT instrument in this research from other instruments, because it eliminates the need to dedicate a SEM exclusively to CNT testing. The device volume constraint allows the nanopositioner to be quickly and easily installed while minimizing extra adjustments to the original SEM components. The benefits from this were:

- Minimal disturbance to the SEM functionality, which has been pre-calibrated to original SEM settings



- Adaptability of nanopositioner to a wider variety of SEMs than competing internal SEM instruments
- Flexibility for the user to use the SEM for other research purposes besides operating the nanopositioner (user needs to only take out nanopositioner and mount in another device, which would be similar to changing samples).

The other three design constraints (high vacuum compatibility, zero magnetic field interference, and uniform conductivity) are important to the quality of the SEM imaging. If any of three constraints are not met, the results from conducting image analysis to determine CNT mechanical property data will be compromised. In other words, the sub-nanometer image resolution necessary to measure any deformation of the CNT would be sacrificed; therefore, increasing the uncertainty of the data as a function of the severity of the image degradation.

## **2.2 Functional Requirements**

Functional requirements are associated with a performance metric and an acceptable tolerance window. For the nanopositioner design, the functional requirements were linked to how well it would accomplish different modes of mechanical CNT testing. This was directly related to the geometry and scale of the CNT and translated into the specifications on range, resolution, accuracy, repeatability, etc. A summary of the functional requirements, their specifications, and their reasoning is given in Table 2.2.

*Table 2.2: Nanopositioner design functional requirements listed with their specifications and the reasoning for them.*

<b>Functional Requirement</b>	<b>Specification</b>	<b>Reason</b>
Kinematic Requirement	6-axis	Allows instant center at any point in the device workspace for proper interfacing with the test sample and for multi-axis testing.
Resolution ( $\Delta_x, \Delta_y, \Delta_z$ ) ( $\theta_x, \theta_y, \theta_z$ )	1-10 nm 1-10 $\mu$ rad	Finest incremental motion is $1/10$ characteristic length of the CNT, which is the CNT diameter. This allows the CNT to be deformed and characterized with meaningful precision. The rotational resolution corresponds to the minimum angular deflection of the CNT to displace the end 1 nm.
Repeatability	1-10 nm	Must be repeatable on the same order of the resolution in order to make use of the nanometer resolution.
Range ( $\Delta_x, \Delta_y, \Delta_z$ ) ( $\theta_x, \theta_y, \theta_z$ )	1-2 $\mu$ m 1-10 mrad	Must overlap with the course stage resolution to provide fine and course resolution throughout the device workspace. Total range matches total range of CNT test sample.
Accuracy	10-50 nm	Matches the characteristic CNT dimension in order for the positioner to be maneuvered into contact with the CNT in the test sample.
Stability/Dynamics	> 1kHz	Reject vibrational noise from environment (< 100 Hz), because at 1 kHz, the vibrational noise causes sub-angstrom vibration to the positioner, which is negligible. Resonance is 10 times higher than nominal quasi-static operating frequency, so operating vibrations are also rejected.
Force Application	1 nN – 10 uN	Must be able to apply enough force to conduct different testing modes (tensile force $\sim 1 \mu$ N and bending force $\sim 10$ nN) [25].
Fabrication	< \$2000	Production costs must be less than commercially available multi-axis nanopositioners.

From a high level standpoint, the required order of operation for the nanopositioner was the following:

1. The nanopositioner must interface with the test sample at the right position and in the right orientation
2. The nanopositioner must induce a controlled amount of CNT deformation over a range of motion of interest
3. The nanopositioner must conduct the previous two operations in multiple axial directions.

The kinematic requirement of 6-axis motion is necessary for the nanopositioner to interface with the test sample correctly given the presence of initial placement errors. Meeting the resolution requirement enables the CNT to be deformed at a precision smaller than its characteristic length in order to yield data sensitive to the CNT's properties. In this case, the characteristic length was the CNT diameter. The repeatability requirement is equally as important as the resolution, because its satisfaction enables the nanopositioner to achieve its nano-resolution consistently. Fulfilling the range requirement allows the nanopositioner to perform its high resolution testing over the full range of motion capable by the CNT test sample. The force imparted onto the test sample from the nanopositioner needs to be large enough to achieve the desired deformation; otherwise, the full range of the nanopositioner will not be utilized. Satisfying the accuracy requirement allows the user to navigate the nanopositioner to a desired location. This will be critical when trying to interface the CNT test sample at a desired point.

In order to accomplish the functional requirements reliably, the positioner needs to reject dynamic disturbances present in the environment. The noise was typically vibrational noise that occurred in a frequency domain below 100 Hz. Thus, the resonant frequency of the nanopositioner was set to be higher than the noise frequency by a safety of factor of 10 to ensure the dynamic disturbances would induce vibrations smaller than the motion resolution of the

positioner. Finally, practical considerations about the manufacturability of the nanopositioner were set to give the nanopositioner a competitive edge over existing nanopositioners.

### 2.3 Design Strategies

Primarily, the question of what type of motion mechanism and what type of actuation would best address the design goals were answered next. Possible motion mechanisms included rigid-link mechanisms, compliant mechanisms, force-field based manipulation, and relative sliding stages. Their attributes were compared relative to how well they satisfied the requirements. Table 2.3 is a Pugh chart that summarizes the comparison of possible motion mechanisms.

**Table 2.3: Pugh chart comparing potential motion mechanisms for the nanopositioner. A conventional rigid link mechanism was used as the baseline.**

<b>Motion Mechanism Pugh Chart</b>				
	<b>Rigid Link Mechanism</b>	<b>Compliant Mechanism</b>	<b>Force-field Based</b>	<b>Relative Sliding Stages</b>
<b>Constraints</b>				
Height/Footprint	0	+	+	-
UHV	0	+	0	0
Magnetic interference	0	0	-	0
Electr. conductive	0	0	-	0
<b>Functional Requirements</b>				
Kinematic	0	0	-	0
Range	0	-	-	+
Resolution	0	0	0	0
Repeatability	0	+	-	0
1kHz resonance	0	-	+	0
Manufacturability	0	+	0	0
<b>Total</b>	<b>0</b>	<b>3</b>	<b>-2</b>	<b>0</b>

Similarly, potential actuators were compared after the motion mechanism was determined. Table 2.4 is a Pugh chart that compares motors, magnetic actuators, stacked piezo-electric actuators, and piezo-electric worm actuators.

*Table 2.4: Pugh chart that compares different potential actuators to be used in compliant mechanism based system.*

<b>Actuator Pugh Chart</b>				
	<b>Motor</b>	<b>Non-contact Magnetic Field</b>	<b>Stacked Piezo- electric</b>	<b>Piezo-electric Worm</b>
<b>Constraints</b>				
Height/Footprint	0	-	+	+
UHV	0	0	+	+
No magnetic field	0	0	0	0
No charge build up	0	-	+	+
<b>Functional Requirements</b>				
Kinematic	0	+	-	-
Range	0	0	-	+
Resolution	0	0	+	0
Repeatability	0	0	+	+
High resonance	0	-	+	+
Manufacturability	0	0	+	+
Output Force	0	0	+	-
<b>Total</b>	<b>0</b>	<b>-2</b>	<b>6</b>	<b>5</b>

### **2.3.1 Motion Mechanism Design Strategy**

After evaluating the different motion mechanisms, compliant mechanism (CM) was chosen to be the best strategy to deal with the all the constraints and functional requirements. By comparison to the other strategies, CMs satisfy the constraints most easily due to their monolithic and frictionless nature described in Chapter 1. For instance, their layered monolithic construction addresses the height and footprint constraint if designed correctly. Secondly, their lack of sliding joints avoids the use of lubricants that could outgas under ultra high vacuum. Thirdly, their monolithic construction avoids charge build up by using any conducting material, such as aluminum. The force-field based mechanism, which includes magnetic flux actuators and electrically charged substrates, would likely disrupt the SEM functionality, thus not fulfill all the constraints. Likewise, relative sliding stages would mostly likely not fulfill the size constraints,

especially when dealing with multi-axis motion that requires stacking single axis stages on top of each other.

By comparison, CMs met the repeatability and manufacturability requirements better than the alternatives. The high repeatability in CMs stems from its near frictionless motion, which is contrary to both the rigid link mechanism and in the sliding stages. Their good manufacturability derives from their monolithic construction, which results in a lower part count and less assembly costs. These advantages outweigh its main disadvantage of limited range. Thus, CM was chosen over the other strategies as the motion mechanism when considering the overall design goal.

### **2.3.2 Actuator Selection**

After the compliant mechanism strategy was chosen, the appropriate actuators were then selected to compliment a CM-based system and achieve the constraints and functional requirements. Already, some of the design aspects of the CM had been pre-determined by the constraints and functional requirements. For example, the 1 kHz resonant frequency and device envelope requirements were used to determine the overall stiffness of the device and help select the actuator type. In this case, it was also assumed that the positioner was made of metal in order to meet the constraints.

After comparing the different actuator types, stacked piezo-electric actuators were chosen to actuate the compliant mechanism based nanopositioner. In terms of constraints, the two piezo actuator types better satisfied the space constraint and the magnetic interference constraint than the other two actuation types. Motors and magnetic field actuators were, by nature, magnetically driven, which required them to be properly shielded from the SEM's e-beam in order to preserve

the SEM's imaging quality. Due to the SEM's high sensitivity to any foreign magnetic field, determining whether a foreign magnetic field is negligible to the SEM performance cost time and additional experimentation. From this stand point alone, the piezo actuators would provide cost benefits over the other two types of actuators. In terms of limited space, especially when dealing with multiple actuators, the stacked piezo-electric actuators were the most compact. They were single piece actuators that required no additional components to transfer their motion to a physical interface. Also, their installation required no additional lubricants or adhesives that could potentially outgas.

When comparing the different actuator types by how well they could satisfy the functional requirements, the two piezo-electric type actuators were closely matched. Both types of piezo-electric actuators provided excellent resolution due to their piezo-electric nature that derived its strain from the material's electromechanical property. At the same time, achieving 6-axis motion within a compact system provided a challenge for both types of piezo-electric actuators, primarily because they could only actuate in a single direction on a physical interface. This was contrary to the non-contact magnetic field actuator that could actuate in multiple directions on a single actuation node. However, the constraints dictated that the actuator be either of the two types of piezo-electric actuators. While the piezo-electric worm/motor actuator offered more than 100 times the range of the stacked piezo-electric actuator at comparable resolution, the stacked piezo-electric offered a much higher force output and stiffness. Despite the difference in range, both types of actuators could easily fulfill the range requirement of 1  $\mu\text{m}$ , but only the stacked piezo-electric actuator could generate enough force and have enough stiffness to actuate the compliant mechanisms for a 1 kHz resonance system. Thus, the stacked piezo-electric

actuator was chosen as the actuator. More specifically, the P-885.11 from Physik Instrumente (PI) was chosen. Its specifications are listed in Table 2.5.

*Table 2.5: Key technical data for chosen stacked piezo-electric actuator from Physik Instrumente.*

<b>Technical Attributes</b>	<b>P-885.11</b>
Dimensions [mm]	5 x 5 x 9
Nominal Displacement @ 100	7
Blocking Force @ 120 V [N]	900
Stiffness [N/ $\mu$ m]	115
Resonant Frequency [kHz]	135

Additional benefits provided by stacked piezo-electric actuators were their single part construction and low thermal expansion of 3 ppm/K, about 8 times less than aluminum [24]. Their single part construction made them very easy to install and minimized the part count of the overall device that required several actuators. Their low thermal expansion minimized the actuation inaccuracies that were due to thermal fluctuation in the system.

On the other hand, piezo-electric actuators exhibited hysteresis and creep that were products of ferroelectric polarization effects intrinsic to the piezo-electric material. The hysteresis was a function of applied voltage that could reach up to 15% of the actuated displacement at nominal voltages. The creep is a logarithmically decreasing function with respect to time, but can account up to 5% of the total displacement in the first minute. Although adjusting the actuation voltage could compensate for the hysteresis and creep using calibrated values in an open-loop



system, the optimal solution was to control the actuators in a closed-loop system where hysteresis and creep could be eliminated.

## **2.4 Design Conception and Selection**

After the compliant mechanism strategy and stacked piezo-electric actuators were selected, subsequent designs were created and developed to fit the constraints and functional requirements. The overall design of the nanopositioner consisted of three main parts:

1. The compliant mechanism for achieving 6-axis motion
2. The compliant transmission mechanisms for de-amplifying and directing motion
3. The interfaces between different components to ensure proper constraints.

### **2.4.1 Six-Axis Compliant Mechanism Design**

Six-axis compliant mechanism (CM) design is a relatively new technology compared to its rigid link counterpart. For this research, the nanopositioner design borrows the HexFlex technology [1] introduced by Anderson and Culpepper, because it offers a planar design to achieve 6-axis motion unlike traditional CM designs. Traditionally, CM designs have consisted of planar structures that guide input forces and displacements within the same plane as the structure. Common CM building blocks include leaf springs, localized flexural pivots, and four-bar mechanisms. These basic CM building blocks are combined to create more complex devices, which normally leads to a large device envelope in the case of multi-axis motion that include out-of-plane motion.

Although the HexFlex offered the 6-axis motion required for the nanopositioner, its adaptation to piezo-electric actuation required the eventual decoupling of its in-plane and out-of-plane motion. The HexFlex device was originally developed to use magnetic field actuators, which allowed the actuator to produce 2-axis motion on a single actuation tab. In addition, the magnetic field actuators allowed the actuation tabs on the HexFlex to move unconstrained in the radial direction, because the actuators did not require a physical interface with the HexFlex. Figure 2.1 illustrates the actuation forces from the original magnetic field actuators on the actuation tab.

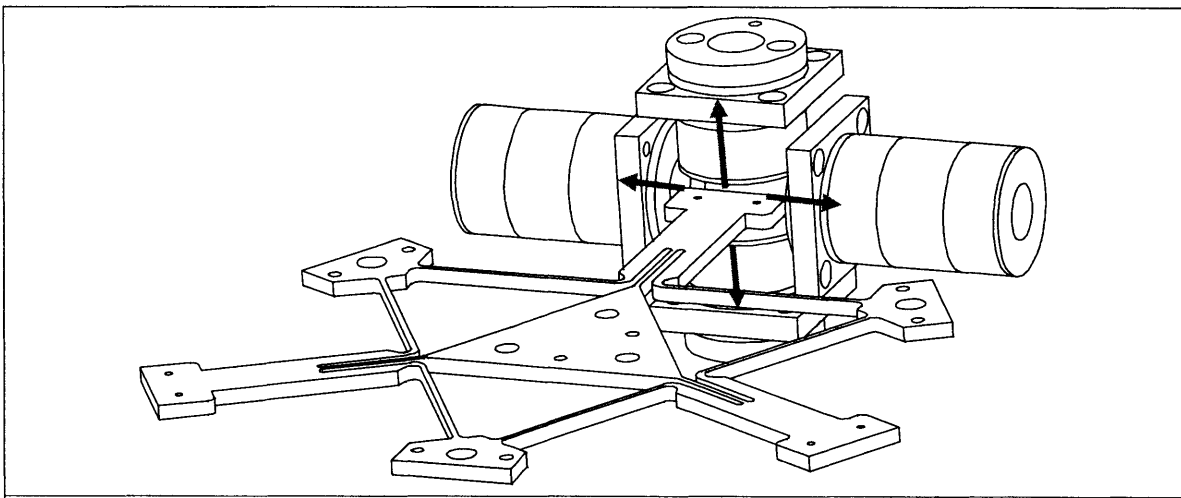
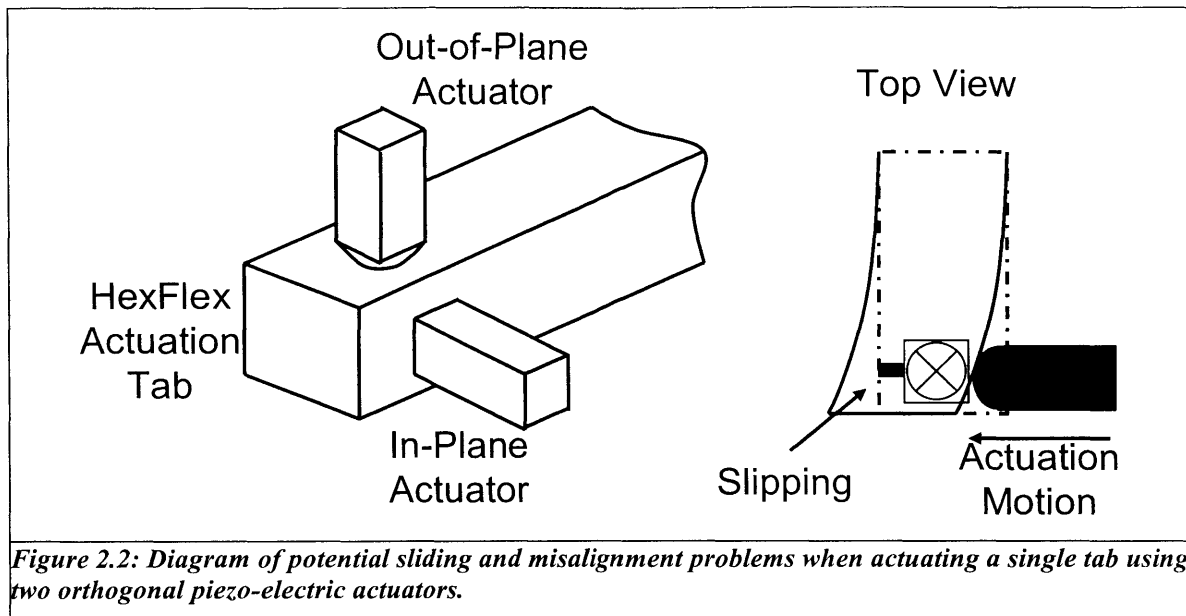


**Figure 2.1: Diagram of simultaneous actuation forces in the tangential direction and in the out-of-plane direction at a single actuation tab on the HexFlex.**

The main obstacle with actuating the HexFlex with piezo-electric actuators was that two orthogonally positioned actuators needed to share the same actuation tab. This effectively coupled the two actuation motions, creating parasitic motion and over-constraints of the HexFlex. More specifically, pushing on the tab in the tangential direction affected how the out-of-plane actuator interacted with the same tab. Figure 2.2 is a diagram of potential sliding and misalignment problems when actuating a single tab using two orthogonal actuators.

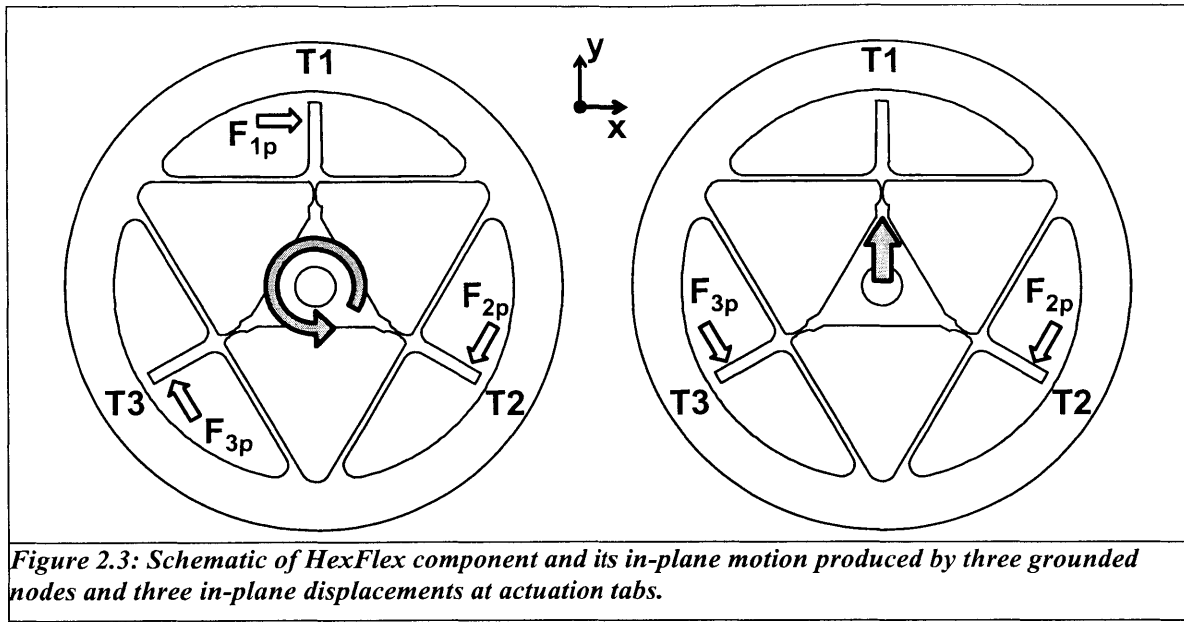


This set the stage for the first design challenge, which was to allow orthogonal actuation at a single tab without affecting the actuation performance in either direction.

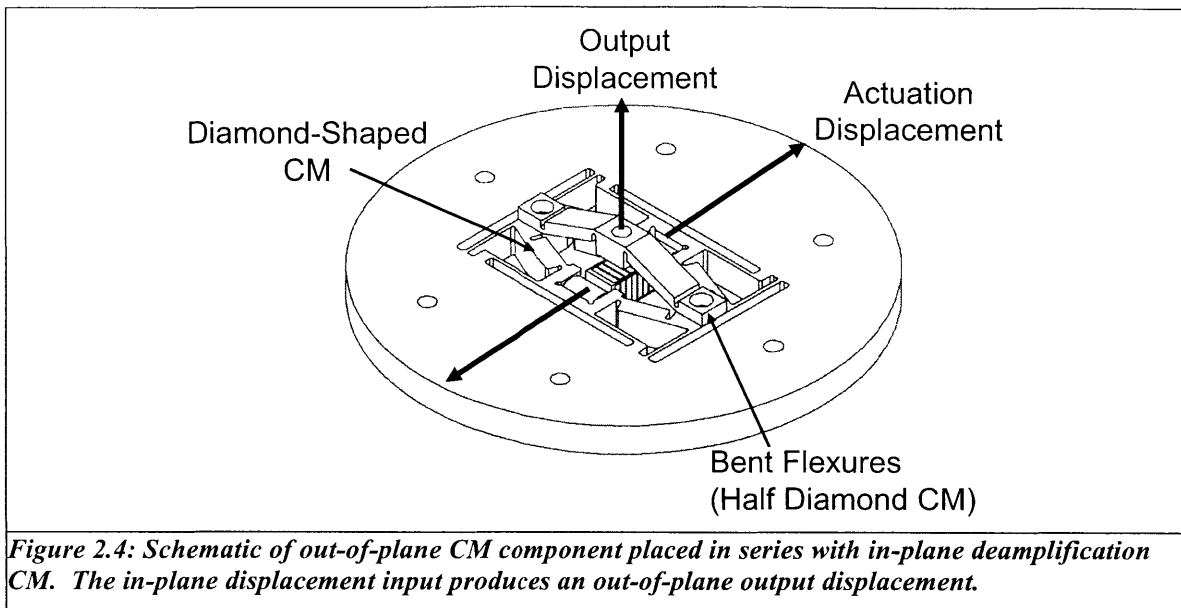
Several designs were considered to actuate the HexFlex piezo-electrically. The first approach was to decouple the actuation tab by separating it into two interfacing points, one for each actuator. This meant enlarging the tab on the HexFlex and using flexures to allow one actuator to keep in rigid contact with the tab while the other actuator displaced the same tab at another interfacing point. This design was rejected because the parasitic errors associated with this design were on the order of the desired output motion. The required degrees of freedom (DOFs) for each actuator flexure sub-system required features that were smaller than what available fabrication methods could offer, which led to large parasitic errors. The second approach was to couple the actuators so that they operated in series similar to stacked stages, except using flexures. Although this would achieve the independent motion at each actuation tab, the corresponding flexure system would violate the 2 cm height constraint for the device. Also, this approach would require additional flexures to allow the actuation tab to move freely in the radial

direction. The final design approach was to uncouple the in-plane and the out-of-plane motion. To do this, the in-plane motion components were stacked on top of the out-of-plane motion components, which varied the height at three independent points underneath the in-plane motion module, like a tripod. This approach reduced parasitic errors present in the coupled and decoupled designs. In addition, this design offered a compact device envelope that fit within the space constraint. Moreover, by separating the components, the development of the respective components could be done independently in parallel to save time and manufacturing during iterative design stages.

The final design utilized the HexFlex for in-plane motion ( $\delta_x, \delta_y, \theta_z$ ), and was stacked on top of three out-of-plane compliant transmission mechanisms that provided out-of-plane motion ( $\delta_z, \theta_x, \theta_y$ ). The HexFlex was grounded at three nodes and actuated at three other nodes (the actuation tabs). The three actuation tabs were actuated tangentially in the clockwise direction by three piezo-electric actuators. Figure 2.3 shows the HexFlex component interfaced with in-plane motion actuators.



The out-of-plane motion module was attached at three points underneath the in-plane motion module. The motion was produced by bent flexures that are attached perpendicularly to diamond shaped compliant mechanisms. The two compliant mechanisms worked in series to transmit the in-plane motion from the actuator into out-of-plane motion. Figure 2.4 illustrates how the compliant mechanisms in this module produce out-of-plane motion.

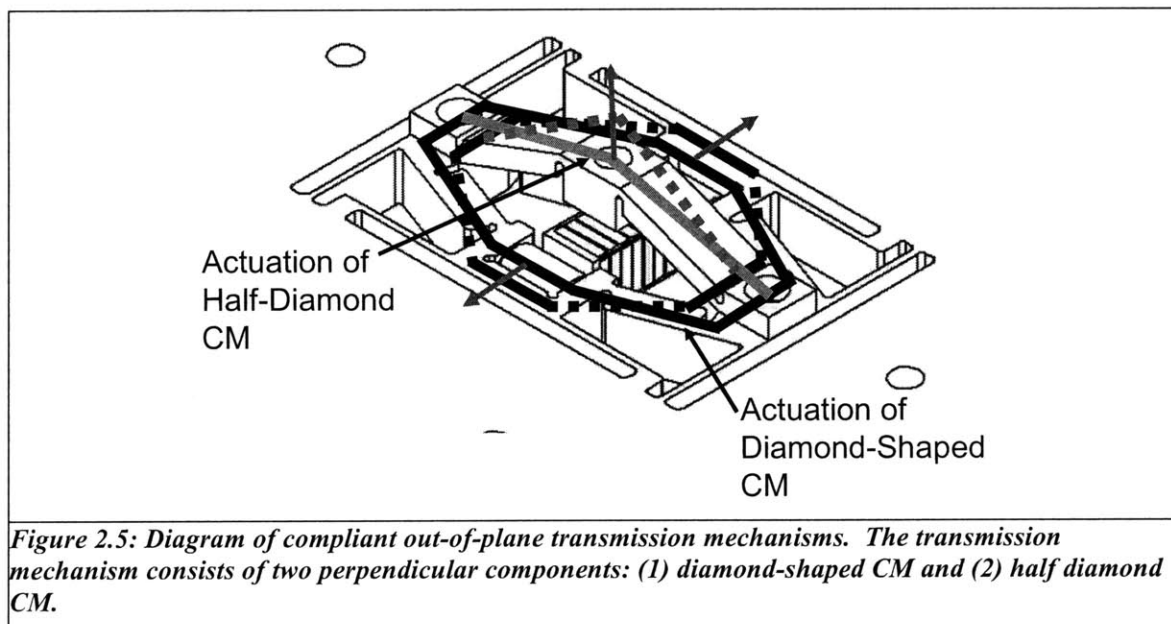


#### 2.4.2 Compliant Transmission Mechanism Design

To achieve the one nanometer resolution, the displacement from the stacked piezo-electric actuators needed to be de-amplified. Although the theoretical resolution of the actuators was sub-nanometer over its range of several microns, the practical limiting factor was the resolution of the electronic controller. In this case, the voltage controller created fluctuation on the order of 10 nm. To compensate for this fluctuation, the total actuator motion was mechanically de-amplified by compliant mechanisms. The tradeoff improved resolution at the expense of range of motion, both by the same factor. This tradeoff was settled by adjusting the de-amplification factor, also known as the transmission ratio, so that the actuator's range would be de-amplified to meet the one micron range requirement. The in-plane and out-of-plane actuators had a range of motion of 7  $\mu\text{m}$ ; therefore, their transmission ratio set to  $1/7$  to achieve 1  $\mu\text{m}$  range of motion.

The HexFlex itself was a compliant transmission mechanism. By tuning the HexFlex geometry, the transmission ratio was adjusted to the  $1/7$  value. For the out-of-plane motion, the compliant

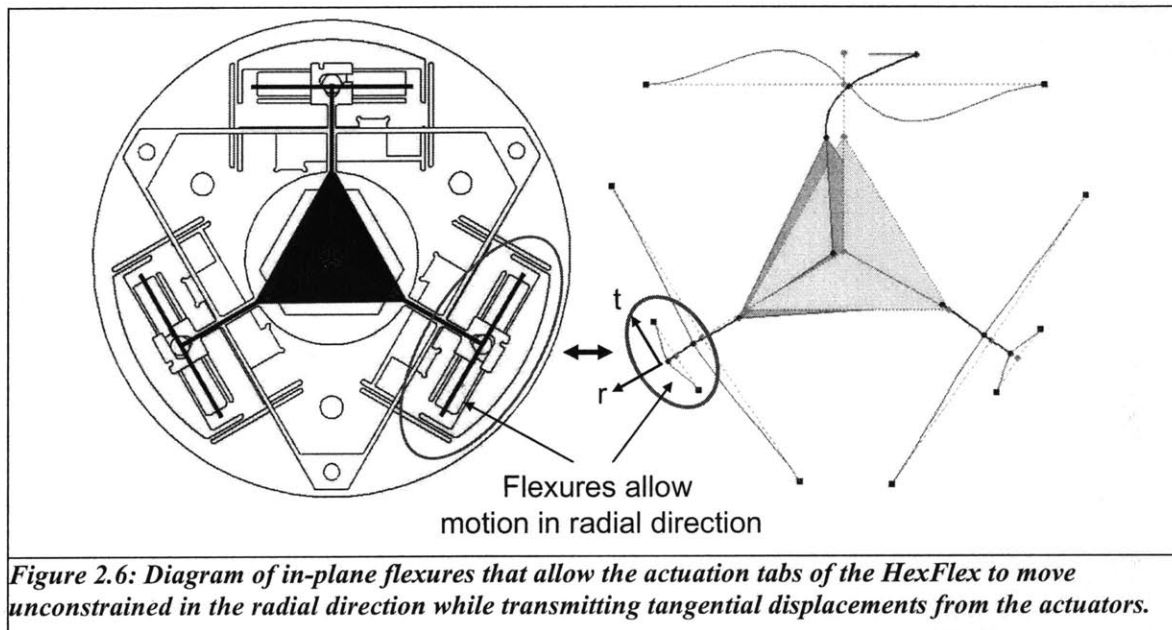
transmission mechanism involved two components. The first component was the diamond-shaped mechanism that interfaced with the actuator. As the actuator displaced opposite corners of the diamond geometry, the other two corners contracted. This contraction then squeezed the second component, which was a flexure that bent out-of-plane. By contracting the two ends of this bent flexure, the flexure height increased out-of-plane. Figure 2.5 is a diagram that illustrates how the in-plane actuator displacement was transmitted into an out-of-plane motion. The de-amplification factor is determined by the geometry of both the diamond mechanism and the bent flexure.



### 2.4.3 Actuation Tab Constraint Design

As mentioned before, constraining the actuation tab to allow the HexFlex to function properly was a large design challenge, especially because piezo-electric actuators required physical contact interfaces. More specifically, the in-plane motion of the HexFlex required the actuation tabs to be unconstrained in the radial direction. To achieve this, the in-plane component design

had a set of leaf flexures, shown in Figure 2.6, that operated in series in between the actuator flexures and the HexFlex. The leaf flexures were at least five times less stiff in the radial direction than in the tangential (actuation) direction. Figure 2.6 illustrates the leaf flexures placement within the in-plane components and how it allows stiff tangential actuation while allowing radial motion.



#### 2.4.4 Component Interface Design

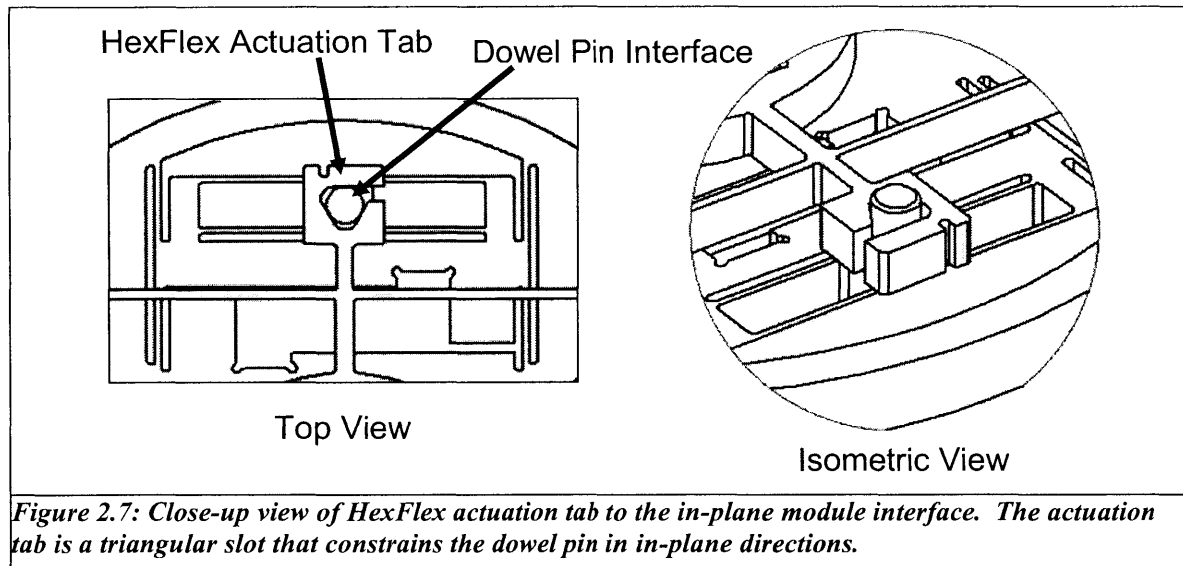
The last design task was designing the interfaces between different components, primarily between moving components. It was important to avoid any stick-slip behavior in order to achieve one nanometer precision. In most cases, this involved creating a rigid interface between two components by bolting them together and filling up the bolt clearance with epoxy. The advantage of using the bolt and epoxy combination was that the components could be correctly positioned with respect to each other by the bolts prior to permanently bonding them together with epoxy. The epoxy was a high vacuum compatible, electrically conductive epoxy that was



suitable for the SEM. Examples of these interfaces would be the grounded nodes for the HexFlex and the interface between bent out-of-plane flexures and the in-plane module. However, not all the interfaces could use this method, such as the interface between the HexFlex and the in-plane module and the interface between the actuators and the device.

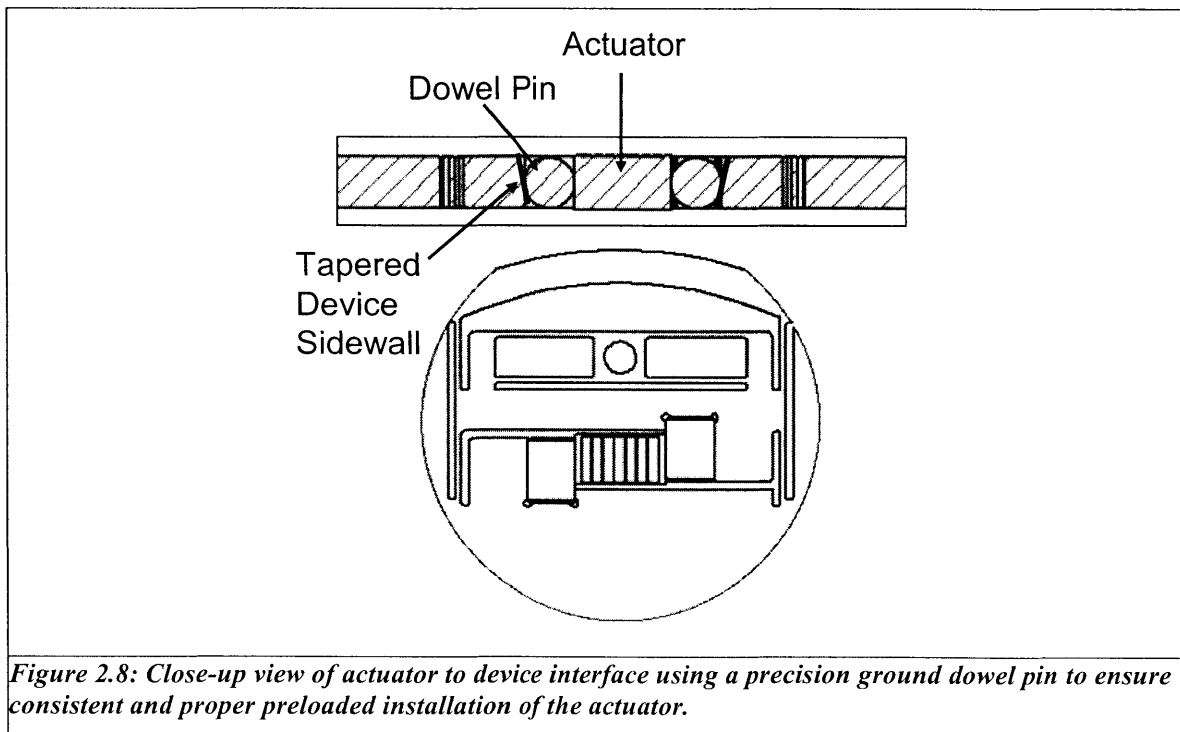
The interface between the actuation tab of the HexFlex and the in-plane module used a compliant triangular slot in the tab to fit around a dowel pin that extended from the in-plane module.

Figure 2.7 is a close-up top view of the interface and its corresponding isometric view.



By using a dowel pin and a triangular slot, the actuation tab was constrained in all the in-plane directions without constraints in the out-of-plane direction. This allowed the HexFlex to be installed correctly into the in-plane module by sliding the triangular slots around the dowel pins while bolting in the grounded nodes. Once the HexFlex was grounded in place, its actuation tabs were bonded to the dowel pins.

The other critical interface was the physical contact between the stacked piezo-electric actuator and the device. These interfaces required a consistent preloaded contact between the actuator and device. Also, the interface had to transmit loading forces to the actuator uniformly across the actuator's contact surface. This meant that tapered and rough surfaces would cause damaging shear loads on the actuator and potentially introduce slipping at the interface. To compensate for these problems, dowel pins were rigidly installed between the device and the actuator interface to produce a consistent line contact interface. The line contact across the actuator interface was consistently straight within a given assembly tolerance, because the dowel pins were installed with its major axis perpendicular to possible tapering in the device. This was true even with surface defects on the contact surface. Figure 2.8 is a close-up view of the dowel pin installed at the interface between the device and the actuator.



## 2.5 Summary of Design

A summary of the main design topics that were discussed in this chapter are listed in below:

- The constraints and functional requirements necessary for the nanopositioner to conduct mechanical CNT tests were determined for the nanopositioner.
- Compliant mechanism was the motion mechanism chosen for the nanopositioner.
- Stacked piezo-electric actuators were chosen to actuate the nanopositioner.
- The in-plane and out-of-plane motion were decoupled in order to avoid parasitic errors using piezo-electric actuators.
- The HexFlex mechanism was chosen for the in-plane motion. Properly constraining the HexFlex required additional flexures for radial DOF at actuation tabs.
- A diamond-shape compliant transmission mechanism in series with out-of-plane flexure was designed for transmitting in-plane actuation motion to out-of-plane motion.
- Dowel pins were chosen to interface the actuators with the device to avoid slipping against the actuator interface and imparting sheer forces onto the actuator.
- Dowel pins were chosen to interface the HexFlex with the device to avoid overconstraining the mechanism.



# CHAPTER 3

## 3 Modeling, Simulation, and Optimization of Selected Concepts

The intent of this chapter is to illustrate the considerations that evolved the concept into a finalized design. After selecting the concept described in the previous chapter, the concept was broken down into modular pieces that could be modeled, simulated, and optimized individually. To first verify that the concept satisfied the functional requirements an error budget was calculated for the overall system. Then the compliant transmission mechanisms were designed to meet performance requirements. Next, the stiffness analysis was conducted for the device, which included modeling the contact stiffness for the actuators. Finally, a dynamic model was made to optimize the dynamic characteristics of the device.

The general approach for evolving the concept into the final design took the following steps:

1. Determine the underlying physics governing the device component

2. Determine first order model of device component
3. Determine general design architecture of the device component
4. Verify design performance using Finite Element Analysis (FEA).

### **3.1 Constructing an Error Budget for Concept Verification**

An error budget is a tool that can assist in characterizing a design and direct its evolution into a final design to satisfy the functional requirements [26]. Constructing an error budget consists of modeling the interaction between the components in the system and accounting for possible sources of errors, such as deflection errors and assembly errors. Normally, an error loop that connects the two performance critical components, such as the positioner and the target sample, is used to gauge the change in performance as errors are introduced. The results from the simulation reveal which type of error is most sensitive to the device. Also, insight can be gained about the design's strengths and weaknesses, leading to design improvements.

At this stage in the design effort, the most suitable concept was chosen based on the requirements described in the previous chapter. The basic components of the concept were modeled using a series of coordinate systems (CSs) that represented their location with respect to each other. The CSs were related to each other by homogeneous transformation matrices that contained each component's rotation and translational properties. The components included in the system were the electron-beam lens, the built-in cantilevered platform and translational stage, the sample carriage, the two layers of the nanopositioner, the end-effector, and the cantilevered sample platform, and sample. The corresponding CSs were placed at the center of stiffness of each of the components, which embedded information about how the components interfaced each other in addition to their location. The error loop started from the nanopositioner's end-

effector and traced through the different CSs to the target sample. A diagram of where the CSs were located with respect to the system components is shown in Figure 3.1.

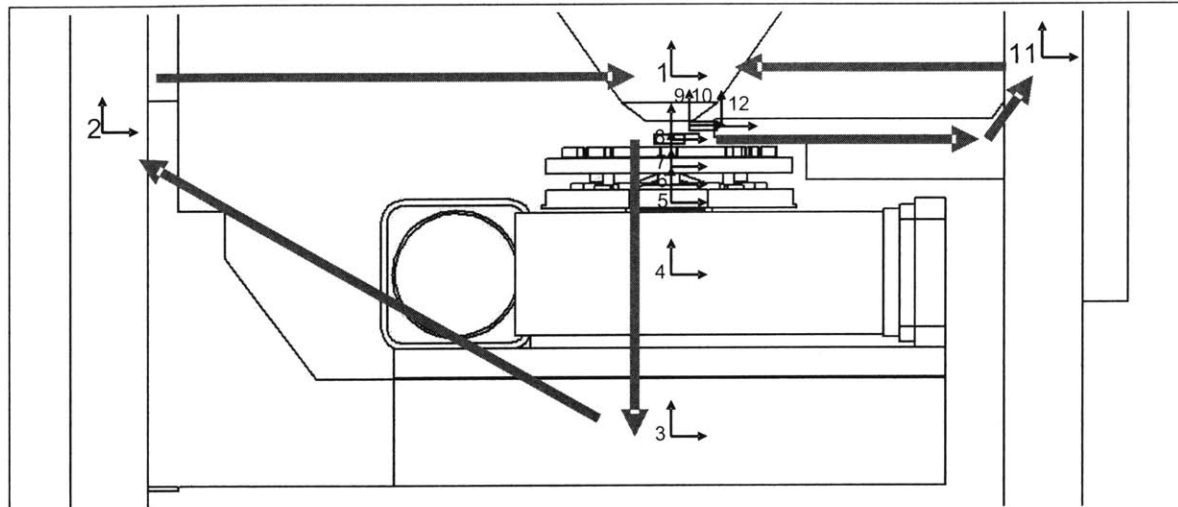


**Figure 3.1:** 2-D Diagram of the different coordinate systems (CSs) used to represent the different critical components of the system for the error budget. The first half of the error loop starts from the nanopositioner’s end-effector (CS9) and traces through the different CSs to the e-beam lens (CS1). The second half of the error loop starts from target sample (CS10) and traces back to the e-beam lens (CS1).

There were three main types of errors that were introduced to the system: (1) thermal errors, (2) fabrication errors, and (3) assembly errors. The thermal errors were modeled as random temperatures that followed a skewed distribution, because temperature rises as the device is operated. The other two errors followed a normal distribution given a mean value,  $\mu$ , and a standard deviation,  $\sigma$ , as inputs. The normal distribution represented the plus-minus nature of the fabrication and assembly tolerance. Also, any systematic errors that did not get averaged out by the assembly process would be calibrated out during performance testing. The errors were randomly generated and selected for different components for each simulation trial. The following table, Table 3.1, summarizes the values used to generate the errors as well as the physical significance of the errors.

*Table 3.1: Summary of the different input errors and their parameters to calculate the error budget.*

Type of Error	Error Parameters	Physical Reasoning
Thermal	$\mu = 22 \text{ C}$ $3\sigma = +0.5 \text{ C}$ Thermal Expansion Constant, $\alpha$ $Al = 23.6 \text{ }\mu\text{m/m-C}$ $Stnls \text{ Stl} = 17.3 \text{ }\mu\text{m/m-C}$	All the components, except the actuators, were made of either aluminum or stainless steel. The thermal fluctuation parameters were taken from measured room conditions and assumed to take place in the SEM chamber as a worst case scenario.
Fabrication	$\mu = 0$ $3\sigma = 0.003''$	Fabrication errors were associated with machining tolerances and stock material manufacturing tolerances that could affect the overall system geometry as tolerances built up from stacking components together.
Assembly	$\mu = 0$ $3\sigma = 0.01''$  Carriage-to-Stage Positioner Base-to-Carriage End-effector-to-Positioner Sample-to-Sample Stage	Assembly errors are associated with errors that arose as individual components were interfaced and put together. These errors were most prominent in components that required repeated removal and installment as part of the testing procedure. Essentially, assembly errors were dependent on the quality of the coupling between components.

The results from the error budget showed that the system was most sensitive to assembly errors, which stemmed from clearance fits and sliding mounts. The assembly error envelope was twice as large as the fabrication error envelope and a few hundred times greater than the thermal error envelope. The overall results of 100 simulation trials that map out the errors are shown in Figure 3.2.



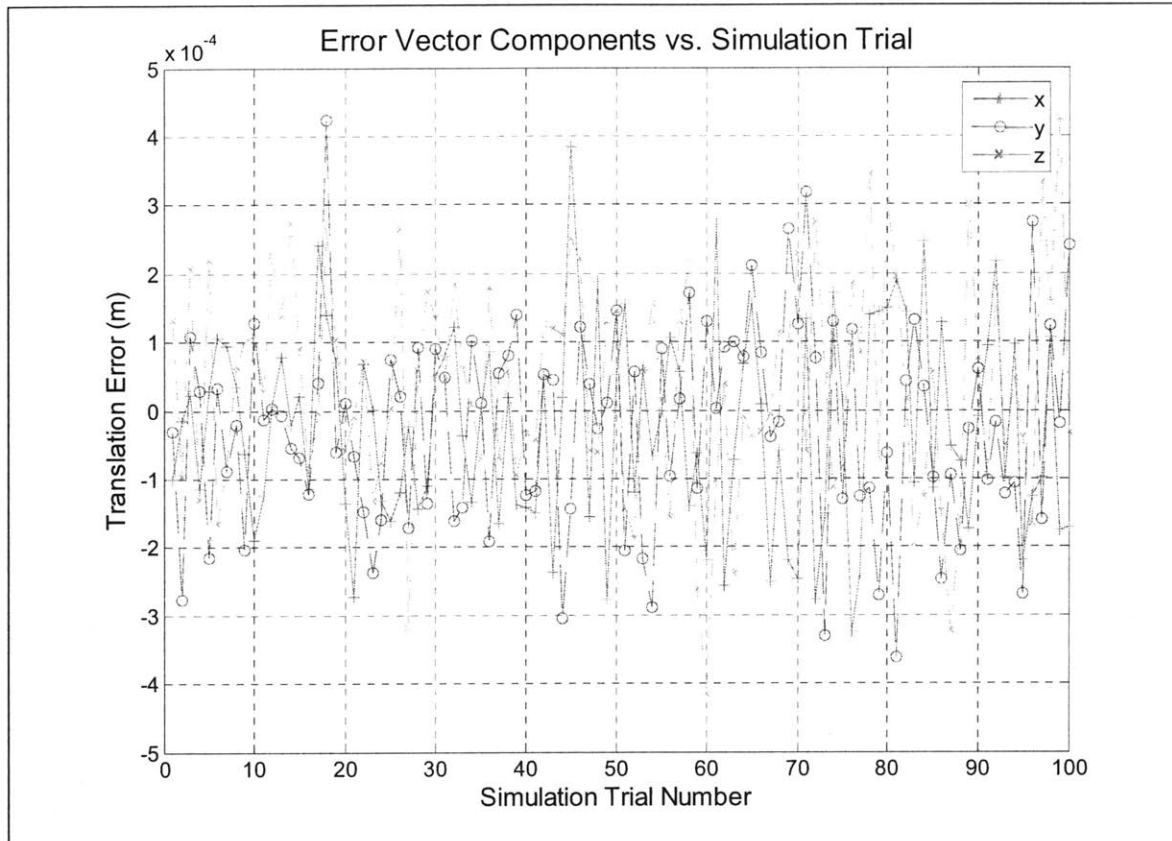


**Figure 3.2:** Plot of the error budget results for 100 simulation trials. The results plot the error vector components from end-effector to target sample.

The error envelope, evident in the figure, shows that the extent of the simulated errors could reach 400  $\mu\text{m}$ . These results highlighted a key advantage for keeping fabrication and assembly consistent with minimal parts and operations. More specifically, the results played an important role in deciding which fabrication technique would be used for building the device, which is discussed in Chapter 4. In addition to pointing out where the system was most sensitive, it also confirmed that the system design of stacking the fine resolution positioner on top of the course positioning stage was a solution to the large translational errors.

### 3.2 Compliant Transmission Mechanisms (Mechanical De-amplifiers)

First, the pseudo-rigid body model was used to predict the kinematics of the compliant elements.

Then, the modules were modeled in CoMeT, a CM synthesis/analysis software package, where

their mechanics and motion were simulated by applying forces and displacements on the model. Finally, the modules were modeled in SolidWorks and their behavior was simulated in COSMOSworks using FEA to verify previous results and ensure stresses were below yield stress. The optimization of the different modules was an iterative process that used results from kinematic, mechanical, and finite element models.

### 3.2.1 Out-of-Plane Compliant Transmission Mechanism

The out-of-plane mechanism was required to transmit the actuator's in-plane motion into out-of-plane motion capable of one nanometer resolution over a range of at least one micron. It was also responsible for generating 150  $\mu$ rad of rotation about the in-plane axes. Three independent actuators needed to be placed symmetric about the central axis. Each actuated a diamond-shaped de-amplifying flexure that in turn actuated an orthogonal half diamond-shaped flexure that stuck out-of-plane. The two CMs worked in series to produce out-of-plane motion.

#### 3.2.1.1 Diamond-Shaped De-amplifying Mechanism

The first step in optimizing the CMs was to approximate its kinematic motion with a diamond-shaped four-bar rigid-link mechanism. The equations obtained from this model provide a starting point for determining the dimensions by relating key dimensions to the transmission ratio. The key kinematic equations and their significance to the design are given in Equations 3.1 and 3.2

$$\frac{\delta_{input}}{2} = \ell(\cos \theta_2 - \cos \theta_1) = \frac{\delta_{output}}{2} \quad \text{Eq.3.1}$$

$$T = \frac{\delta_{input}}{\delta_{output}} = \frac{(\cos \theta_2 - \cos \theta_1)}{(\sin \theta_2 - \sin \theta_1)} \quad \text{Eq.3.2}$$

Where the parameters are:

- $\delta_{input}$  = Input Displacement
- $\delta_{output}$  = Output Displacement
- $l$  = Edge Length
- $\theta_1$  = Initial Angle
- $\theta_2$  = Final Angle
- $T$  = Transmission Ratio

The equations were derived from assuming the diamond-shaped flexure was symmetrical about two orthogonal axes, which allowed it to be broken up into quadrants. Equation 3.1 relates the two internal angles of one quadrant of the diamond-shaped flexure given the flexure length and the desired actuation displacement. Equation 3.2 relates the transmission ratio to the two internal angles of one quadrant of the diamond-shaped flexure. In both equations, the critical dimensions are related back to the internal quadrant angles. Figure 3.3 is a labeled diagram of the kinematic diamond-shaped mechanism model.

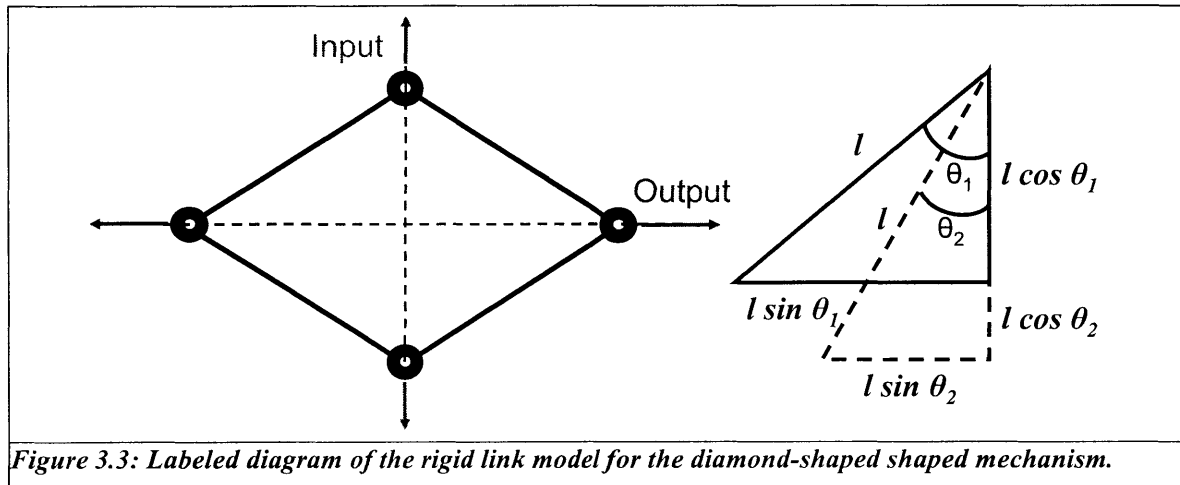


**Figure 3.3: Labeled diagram of the rigid link model for the diamond-shaped mechanism.**

Equations 3.1 and 3.2 were used to determine the preliminary dimensions for the diamond-shaped flexure using a spreadsheet. Knowing the input displacement to be the actuation range, a range of values for the flexure length,  $l$ , and initial internal quadrant angle,  $\theta_1$ , were used to calculate the final internal quadrant angle,  $\theta_2$ , and the transmission ratio. As  $\theta_1$  increased

linearly, the transmission ratio increased exponentially until reaching a singularity at  $\theta_1 = \frac{\pi}{2}$ .

The plot of the modeled relationship is shown in Figure 3.4 along side the FEA results for the diamond-shaped flexure of the same critical dimensions.

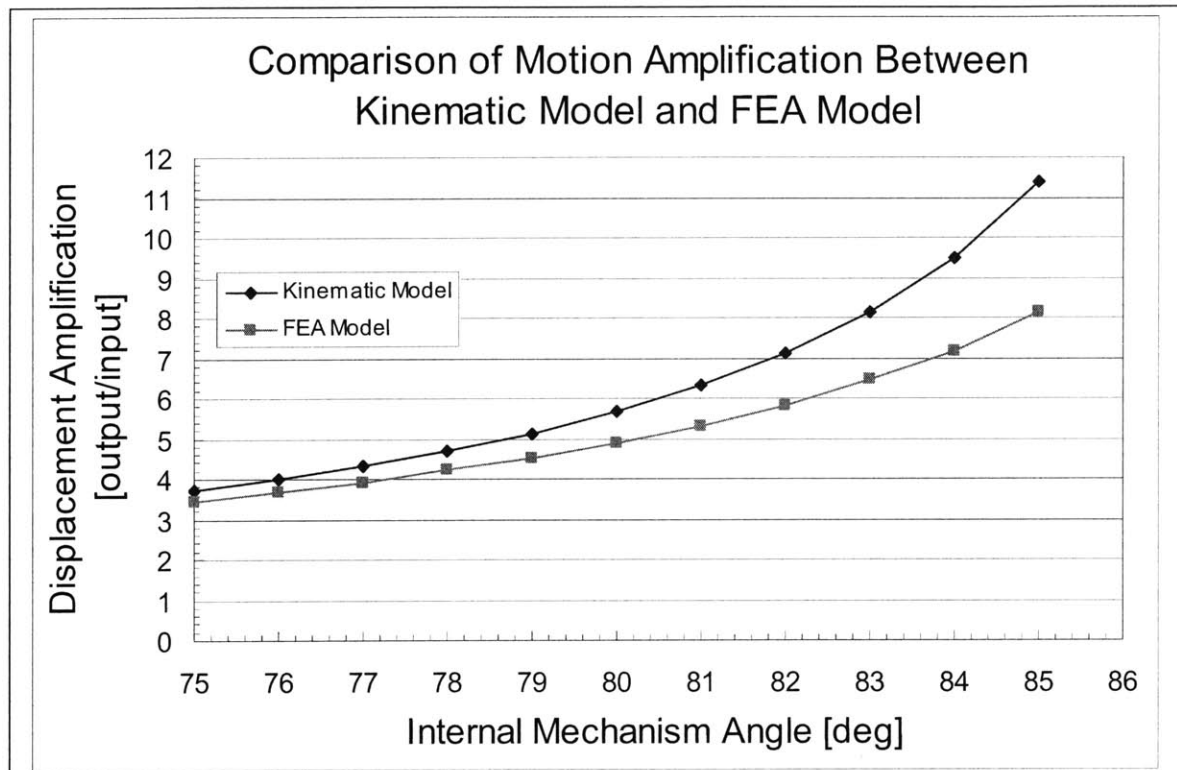


Figure 3.4: Plot of the transmission ratio as a function of the primary internal quadrant angle of the rigid link diamond-shaped mechanism and of the FEA model.

The agreement between the kinematic model plot and the FEA model showed that the kinematic model provided a good starting point. The kinematic model was expected to over estimate the degree of amplification compared to FEA, because it assumed perfectly rigid links with single point revolute joints. The FEA model accounted for the compliance in the link and also the mechanical bending at the flexure pivot. For the 4-axis prototype design, the diamond-shaped flexure was chosen to have a transmission ratio of  $1/7$  in order to satisfy the minimal range

requirement, which corresponded to a primary angle,  $\theta_1$ , of 83 degrees with a flexure length of 8 mm.

### 3.2.1.2 Bent Out-of-Plane Transmission Flexure

The bent out-of-plane transmission flexure was essentially a diamond-shaped transmission mechanism cut in half; therefore, the modeling approach followed the same steps as the diamond-shaped flexure. The only difference between this model and the diamond-shaped model was that the output motion was generated by only one vertex. As a result, the transmission ratio was half the transmission ratio of the diamond-shaped flexure. This is shown in Equations 3.3 and 3.4, which are similar to Equations 3.2 and 3.3, divided by a factor of two.

$$\delta_{input} = \ell(\cos \theta_2 - \cos \theta_1) = \frac{\delta_{output}}{2} \quad \text{Eq.3.3}$$

$$T = \frac{\delta_{input}}{\delta_{output}} = \frac{(\cos \theta_2 - \cos \theta_1)}{2(\sin \theta_2 - \sin \theta_1)} \quad \text{Eq.3.4}$$

Where the parameters are:

- $\delta_{input}$  = Input Displacement
- $\delta_{output}$  = Output Displacement
- $\ell$  = Edge Length
- $\theta_1$  = Initial Angle
- $\theta_2$  = Final Angle
- $T$  = Transmission Ratio

Like the diamond-shaped flexure, the initial dimensions were chosen by looking at the kinematic model and then optimized and verified using FEA.

### 3.2.2 In-Plane Compliant Transmission Mechanism

The in-plane compliant transmission mechanism needed to de-amplify in-plane actuator motion by a factor of 7 to meet the one nanometer resolution and 1  $\mu\text{m}$  range requirements. The chosen mechanism to accomplish this was the HexFlex. CoMeT was used to model and optimize the

HexFlex's dimensions. CoMeT was created for compliant mechanism design at MIT's Precision Compliant Systems Laboratory [27]. CoMeT allowed designers to simulate the CM's behavior due to input forces and displacements using beam bending mechanics to within 5% of FEA results [27]. For this research, the HexFlex was tuned to provide the right de-amplification by adjusting different dimensions and running CoMeT. After the dimensions were determined using CoMeT iteratively, the model was verified by FEA to make sure that yield stresses were not exceeded and that its resonant frequency was above the 1 kHz functional requirement.

### **3.3 System Stiffness Analysis and Modeling**

The stiffness analysis was an essential part of characterizing the overall system. Understanding the system's overall stiffness allows the designer to more closely predict the behavior of the system (i.e. range of motion), the system's modes of resonance, and natural frequency.

The stiffness in the out-of-plane direction was of greatest concern. This was because the majority of the system components were involved with the out-of-plane motion. This was apparent in having two mechanisms work in series for each out-of-plane actuator as compared to the in-plane actuators that shared the HexFlex. Also, the HexFlex behavior has been fully characterized by CoMeT and confirmed in previous research [1] as opposed to the out-of-plane mechanism design.

#### **3.3.1 Out-of-Plane Stiffness**

The approach to modeling the system's out-of-plane stiffness involved combining the out-of-plane stiffness of individual components either in series or in parallel. If the component's stiffness made the system stiffer, it would be combined in parallel. Conversely, if the component's stiffness made the system more compliant, then it would be added in series. In

addition to the component stiffness, the contact stiffnesses at the dowel-actuator interfaces were also taken into consideration for the model. The result was a network of springs, shown in Figure 3.5, that represented the overall out-of-plane system.

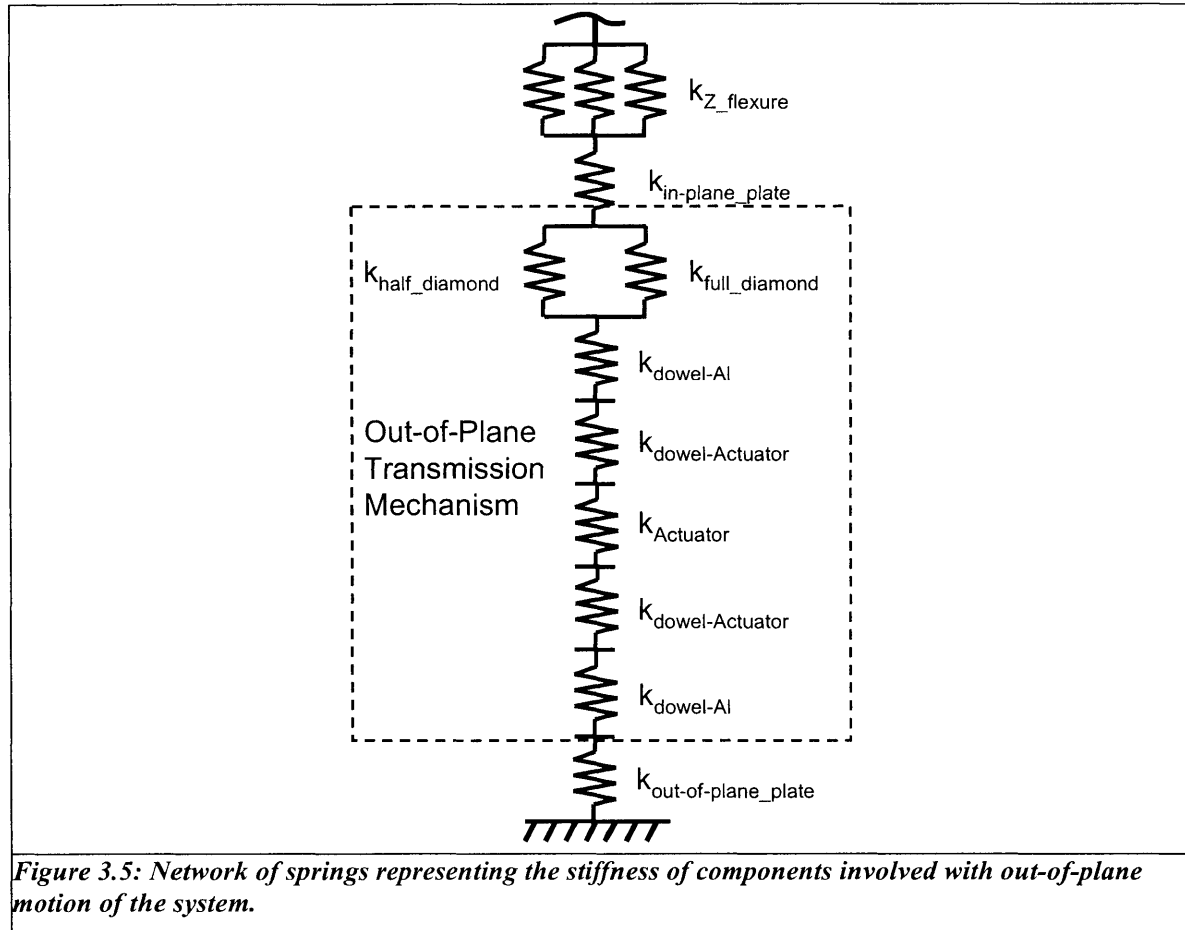


Figure 3.5: Network of springs representing the stiffness of components involved with out-of-plane motion of the system.

The corresponding equations describing the network of springs are given in Equation 3.5 to 3.8, where  $k$  and  $K$  are the stiffness variables.

$$K_{contacts} = \frac{1}{\frac{2}{k_{dowel-Al}} + \frac{2}{k_{dowel-Actuator}}} \quad \text{Eq.3.5}$$

$$K_{amplifier\_sys} = \frac{1}{\frac{1}{k_{half\_diamond} + k_{full\_diamond}} + \frac{1}{K_{contacts}}} \quad \text{Eq.3.6}$$

$$K_{Z\_system\_with\_act} = \frac{1}{\frac{1}{3k_{Z\_flexure}} + \frac{1}{k_{in-plane\_plate}} + \frac{1}{K_{amplifier\_sys}} + \frac{1}{k_{actuator}}} \quad \text{Eq.3.7}$$

$$\delta_{input} = \frac{\delta_{desired\_output}}{\left(1 - \frac{k_{Z\_system\_with\_act}}{k_{out\_of\_plane\_plate}}\right)} \quad \text{Eq.3.8}$$

From the model, equivalent stiffness values were computed to make sure that the actuator output range was enough to meet the desired functional requirements. By creating a ratio between the equivalent stiffness of the system with the actuator stiffness and the out-of-plane stiffness of the anchoring base plate, the system output displacement could be predicted by Equation 3.8. For this prototype, it was critical that the system output displacement meet the one micron out-of-plane range given the actuator input range.

### 3.3.1.1 Transmission Mechanism Stiffness

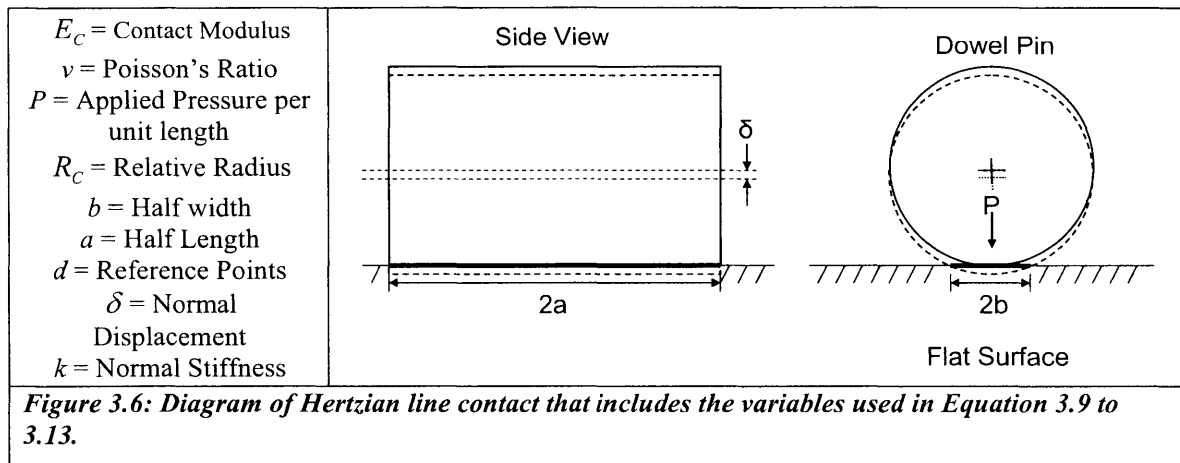
The out-of-plane stiffness for individual components was gathered from FEA simulation results. For components that transmitted their motion from the out-of-plane direction to the in-plane direction, their stiffnesses were computed by applying input forces to two vertices of the flexure and dividing the input force by the resulting displacement of the other vertices.

### 3.3.1.2 Contact Stiffness

The contact stiffness of greatest concern was at the interface between the actuator and the device. The contact stiffness needed to be considered because the system components were not infinitely stiff; thus deformations at the point of contact would occur. The resolution for the device was on the same order as the contact deformation. In the out-of-plane module, as well for the in-plane



module, the actuators were interfaced on both ends with stainless steel dowel pins that were 4.763 mm ( $3/16$  inch) in diameter and 6.35mm ( $1/4$  inch) long. For both modules, the dowel pins were in contact with aluminum. For simplicity, we assumed that the contact surfaces were smooth and produced a Hertzian elastic line contact. The line contacts caused the interfacing surfaces to elastically deform and produce rectangular contact geometry along the length of the dowel pin. The main equations, Equations 3.9 to 3.13, describing the contact stiffness are barrowed by Johnson [28]. The variables are described in Figure 3.6 that is a diagram of the Hertzian line contact.



Equation 3.9 calculates the contact modulus equation that accounts for material properties of two surfaces.

$$\frac{1}{E_c} = \frac{1 - \nu_1^2}{E_1} + \frac{1 - \nu_2^2}{E_2} \quad \text{Eq.3.9}$$

Equation 3.10 is the relative radius equation that accounts for the curvature of two surfaces.

$$\frac{1}{R_c} = \frac{1}{R_1} + \frac{1}{R_2} \quad \text{Eq.3.10}$$

Equation 3.11 calculates the half width of line contact made between the two surfaces.

$$b = \left( \frac{4PR_c}{\pi E_c} \right)^{\frac{1}{2}} \quad \text{Eq.3.11}$$

Equation 3.12 approximates the normal displacement due to applied pressure. This depends on the distance between the reference points and the contact, which must be given in a 2D representation.

$$\delta \cong \frac{P}{\pi E_c} \left\{ \ln \left( \frac{4d_1}{b} \right) + \ln \left( \frac{4d_2}{b} \right) - 1 \right\} \quad \text{Eq.3.12}$$

Finally, Equation 3.13 approximates the normal stiffness due to the applied pressure between the two surfaces. This function is also dependent on distance between the reference points and the contact.

$$k \cong \frac{\pi E_c 2a}{\ln \left( \frac{4d_1}{b} \right) + \ln \left( \frac{4d_2}{b} \right) - 2} \quad \text{Eq.3.13}$$

It was important to note that contact stiffness was a function of the applied load, which meant that the stiffness would change depending on the how far the actuator displaced the compliant mechanism. The further the displacement, the more load would be transferred to the contact. To compensate for this, the actuators were preloaded so that the change in load from actuation was small compared to the preload. This helped keep the load applied at the contact more consistent throughout the range of actuation, which in turn helped keep the contact stiffness more consistent. Also, the stiffness was noted to be proportional to the contact length, which

promoted the use of dowel pins that created a line contact across the entire actuator face and component thickness to maximize contact stiffness.

### 3.3.2 In-Plane Stiffness

The in-plane stiffness model was similar to the out-of-plane model except that there were fewer components to consider; however, there were more contact interfaces. The model consisted of the following stiffness values:

1. Actuator stiffness
2. Contact stiffness at the actuator interface
3. Contact stiffness between the dowel pin at the actuator and the device
4. Leaf spring mechanism stiffness
5. Contact stiffness between the HexFlex dowel pin and the device
6. Contact stiffness between the HexFlex dowel pin and the HexFlex
7. HexFlex stiffness

Figure 3.7 shows the corresponding spring network. Its equivalent stiffness equations for the in-plane system are given in Equations 3.14 to 3.17. Like the previous equations describing the out-of-plane stiffness, the variables  $k$  and  $K$  represent stiffness of components and equivalent stiffness of multiple components, respectively.

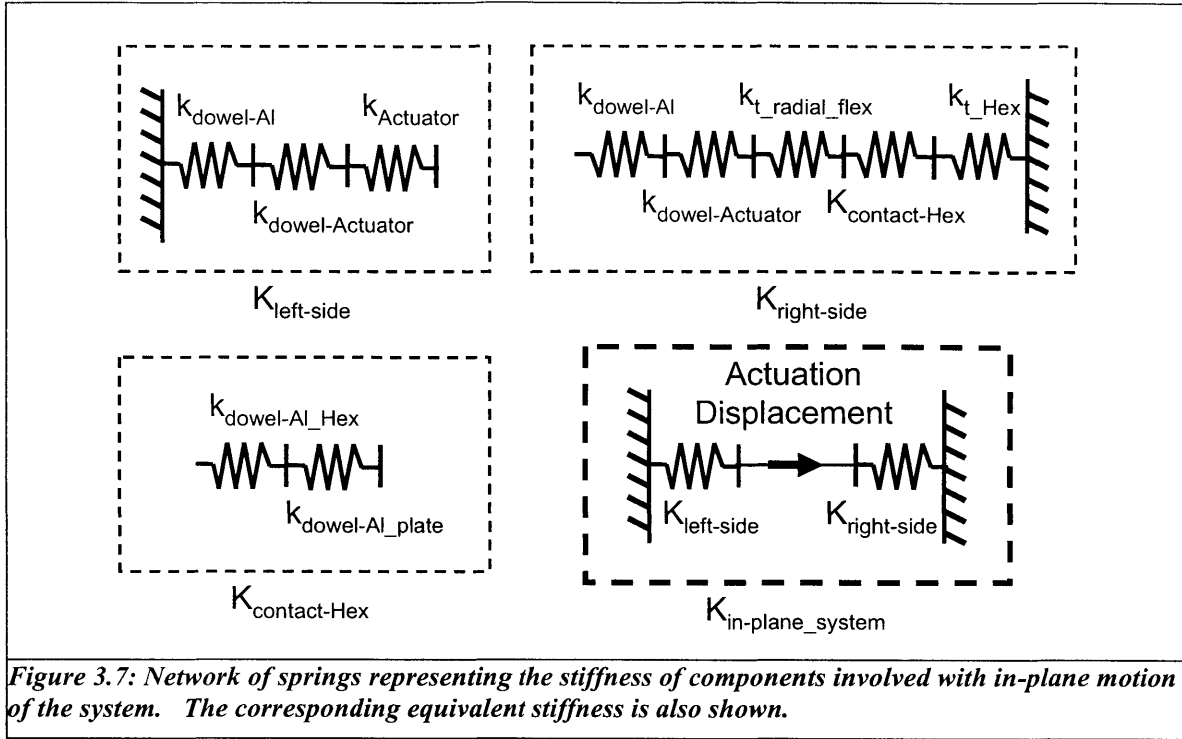


**Figure 3.7: Network of springs representing the stiffness of components involved with in-plane motion of the system. The corresponding equivalent stiffness is also shown.**

$$K_{left\_side} = \frac{1}{\frac{1}{k_{dowel\_Al}} + \frac{1}{k_{dowel\_Actuator}} + \frac{1}{k_{Actuator}}} \quad \text{Eq.3.14}$$

$$K_{contacts\_Hex} = \frac{1}{\frac{1}{k_{dowel\_Al\_Hex}} + \frac{1}{k_{dowel\_Al\_plate}}} \quad \text{Eq.3.15}$$

$$K_{right\_side} = \frac{1}{\frac{1}{k_{dowel\_Al}} + \frac{1}{k_{dowel\_Actuator}} + \frac{1}{k_{t\_radial\_flex}} + \frac{1}{K_{contacts\_Hex}} + \frac{1}{k_{t\_Hex}}} \quad \text{Eq.3.16}$$

$$\delta_{input} = \frac{\delta_{desired\_output}}{\left(1 - \frac{k_{right\_side}}{k_{left\_side}}\right)} \quad \text{Eq.3.17}$$

The compliant mechanism and the HexFlex stiffnesses were obtained through FEA and CoMeT, while the actuator stiffness was obtained from the manufacturer. Only the contact stiffnesses needed to be calculated for this model, because there were no transmission mechanisms in the in-

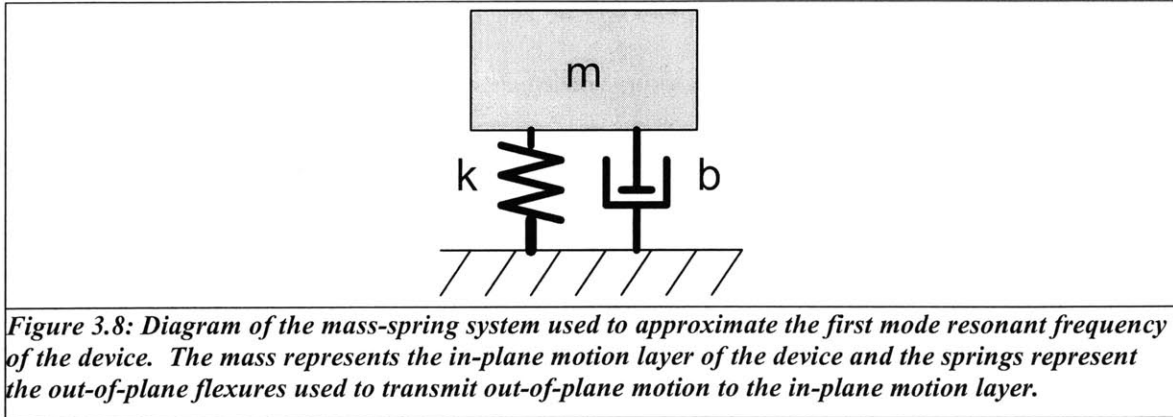
plane system. To solve for the necessary input displacement given a desired output displacement, the chain of springs were divided into two parts at the actuator, as shown in Figure 3.7. Similar to the out-of-plane point stiffness analysis, the ratio of the equivalent stiffnesses from both parts were used to compute the necessary input displacement using Equation 3.17.

After calculating the two types of contact stiffness, their values were used in the system stiffness model to calculate the necessary displacement from the actuators to ensure the range of motion satisfied the functional requirements.

### **3.4 Dynamic Modeling of the System**

The dynamic modeling was an important part of the design process, because it helped determine what operating bandwidth it could handle and what bandwidth of noise it could reject. As mentioned in the Chapter 2, the functional requirement of 1 kHz first mode resonance would be sufficient to reject most of the mechanical noise from the environment. The approach to model the dynamics of the system was to first approximate with a mass-spring-damper model and then verify the results with FEA. This was an efficient method to get an approximation of the resonant frequency of potential designs without relying heavily on time-consuming FEA.

The architecture of the design was essentially a mass-spring-damper system, where the top in-plane layer was the mass and the out-of-plane flexures were the springs that anchored the mass to the bottom out-of-plane layer. A diagram of the model is shown in Figure 3.8.



The architecture dictated the resonance to oscillate in the out-of-plane direction, because the mode was parallel to the system’s most compliant direction. Using the equivalent stiffness calculated in the previous section and the mass calculated by the CAD model, the resonant frequency was estimated by using Equation 3.19.

$$f = \frac{1}{2\pi} \sqrt{\frac{k}{m}} \tag{Eq.3.19}$$

In addition to finding the resonant frequency, the Bode plot was also constructed for the mass-spring-damper system to help see how the system would react to certain vibrational inputs. For example, the Bode plot, shown in Figure 3.9, showed that 20 nm oscillation noise from floor vibrations had negligible (7.61e-6 nm deflection) effects on the device, because the device’s resonant frequency was 10 times higher than the frequency of the noise. The Bode plot also reveals the first mode resonant frequency at the peak.

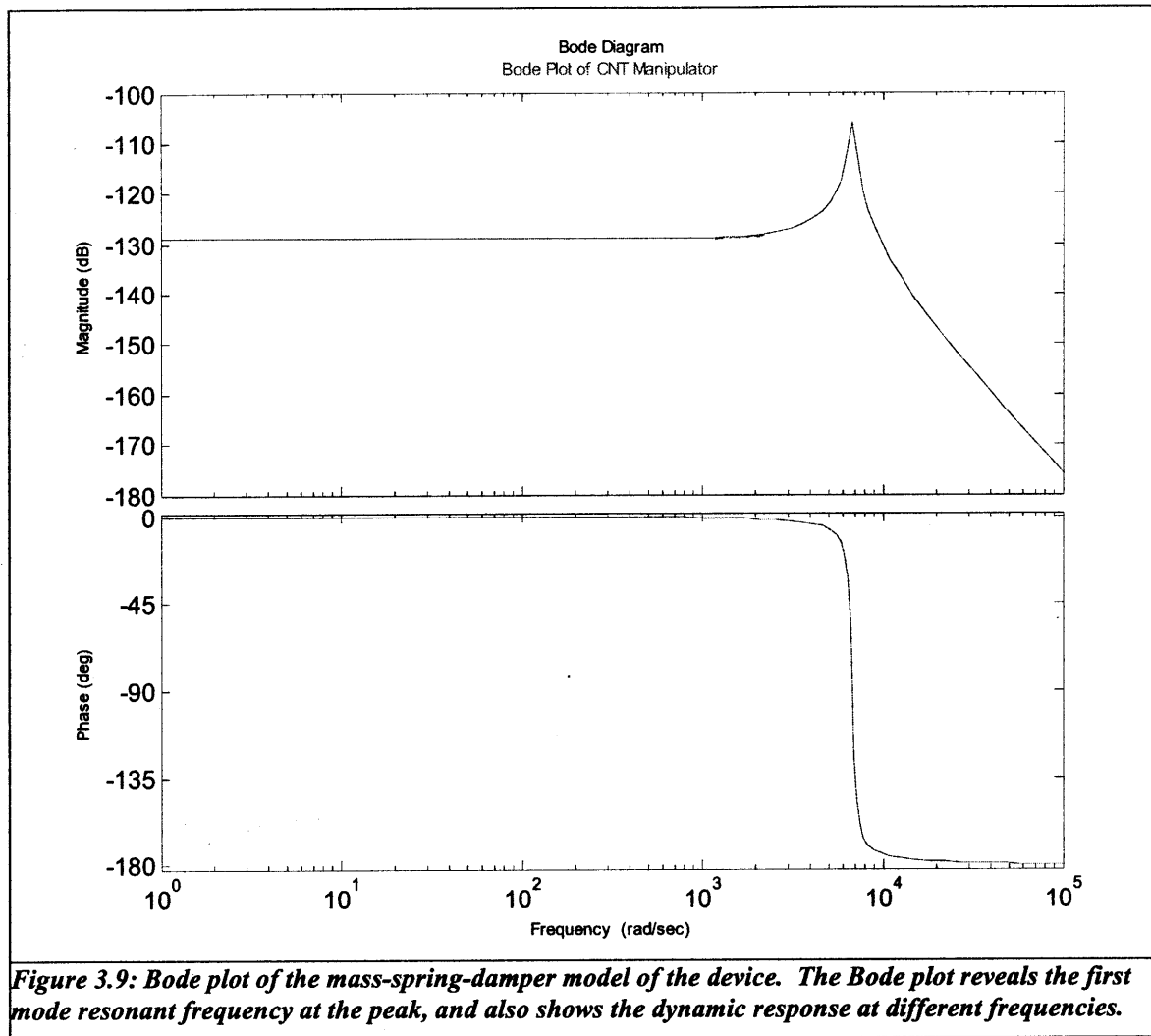


**Figure 3.9: Bode plot of the mass-spring-damper model of the device. The Bode plot reveals the first mode resonant frequency at the peak, and also shows the dynamic response at different frequencies.**

### 3.5 Summary of Design

The nanopositioner design was finalized after modeling its critical components and using the results from the models to iteratively evolve the design to meet the functional requirements. The key components were the compliant transmission mechanisms that transmitted the actuators' motion into 6-axis motion. After the transmission mechanisms were detailed, the rest of the device was designed around them. Creating a stiffness model allowed the de-amplification of the actuator range to be tuned appropriately to meet the functional requirements. This involved creating kinematic models of the compliant mechanisms and also calculating the contact

stiffnesses at different interfaces. Also, the dynamic model of the overall system could be constructed after knowing the general system architecture to make sure that the dynamic functional requirement was met.



# CHAPTER 4

## 4 Fabrication and Assembly of a Prototype

The intent of this chapter is to explore the reasoning behind choosing abrasive waterjet cutting as the primary fabrication method for the nanopositioner components. Also described are the keys steps of pre-waterjet preparation, post-waterjet machining, and device assembly. Finally, the chapter offers suggestions for subsequent manufacturing of the 6-axis nanopositioner product.

### 4.1 Fabrication Method Selection

Selecting the fabrication method for making the nanopositioner played a large role in the design process. In part, the design was developed knowing which manufacturing techniques were available and practical for this research; therefore, design decisions were made to take advantage of certain manufacturing processes. With respect to the nanopositioner, its architecture of multiple layers of planar components allowed it to be fabricated by a machine with only 2.5-axis motion. The half-axis corresponds to the out-of-plane axis that needed to only engage and disengage. Also, the nanopositioner had a space constraint that required that the minimum

feature size be on the order of 0.5 mm (0.02 inch). Finally, practical considerations were taken into account such as availability, average machining time, and costs. Table 4.1 is a Pugh chart that summarizes the different factors that were taken into consideration.

**Table 4.1: Pugh chart comparing the three most feasible fabrication methods for making the nanopositioner.**

<b>Fabrication Method Pugh Chart</b>			
	<b>Waterjet Cutting</b>	<b>Wire EDM</b>	<b>CNC Milling</b>
<b>Criterion</b>			
2.5 axis (Out-of-plane machining axis needs to only engage/disengage)	0	0	+
0.5 mm feature size	0	+	0
Precision	0	+	+
Cost	0	-	-
Availability	0	-	0
Prep Time	0	-	-2
Machining Time	0	-	-2
<b>Total</b>	<b>0</b>	<b>-2</b>	<b>-3</b>

Possible machining methods that were considered were CNC milling, wire EDM, and waterjet cutting. Looking at the Pugh chart, it showed that wire CNC milling was the least favorable fabrication method, due to substantially longer preparation and machining time associate with CNC milling as compared with wire EDM, especially for the nanopositioner device. This is indicated by the two -2 values in the preparation and machining time categories. Given this consideration and the considerations shown in the Pugh chart, the method of CNC milling was eliminated as a possible choice early in the design process.

Waterjet cutting and wire EDM remained as the most potential fabrication methods. On one hand, the wire EDM was an ideal method for precision planar construction, especially for flexure-based mechanisms because of the absence of cutting taper and minimal surface defects.

However, the cost, preparation, machining time, and availability ultimately became critical factors that eliminated it as an option. Wire EDM cost 10 times as much as waterjet cutting and took 10 times longer to prepare and machine. In addition, the parts needed to be sent out to be machined, leading to extra delivery time. Several design prototypes were needed as a part of this design process; thus, the needs of fast and cheap construction became critical. Waterjet cutting provided a fabrication method that met the criteria and fit within the research budget. The waterjet was readily accessible at a cost of \$200 per machining hour. On average, the main components of the nanopositioner took only 15 minutes to cut with the waterjet. In the end, as the Pugh chart prescribed, waterjet cutting proved to be more suitable for building the nanopositioner components.

## **4.2 Waterjet Cutting**

To prepare waterjet cutting is a relatively simple procedure that involved converting 3D CAD models into a planar cutting path for the waterjet. Achieving the feature sizes necessary for this particular design required extra manipulation of the cutting path. The smallest cut feature size on the design was 0.762 mm (0.03 inches), the diameter of the cutting beam from the waterjet nozzle. Normally, the standard waterjet software that creates the cut path does not compensate for cutting such a small dimension. The result was a cut that did not puncture through the material near the beginning of the cut. To remedy this problem, the width of the cut path was increased, while the beam off-set from the path was also increased. This allowed the software to retrace the cut path and ensure that the cut passed through the material along the entire path. Also, this method took advantage of the software's auto path generation function, which greatly sped up the procedure.

Another adjustment to the normal waterjet procedure was to reduce the cutting speed in order to reduce taper. Taper in a flexure-based mechanism can potentially reduce the life of a piezo-electric actuator by creating an interface that would be more prone to slipping depending on the actual contact geometry. Also, the taper could affect the flexure behavior because the cross-section of the beam would no longer be rectangular. The taper was a product of the “floppy” nature of waterjet cutting. As the jet of abrasive garnet and water penetrates the work piece, it dissipates energy, which in turn leads to deflection and lag. Figure 4.1 is a photograph of the waterjet cutting the in-plane motion component of the device.

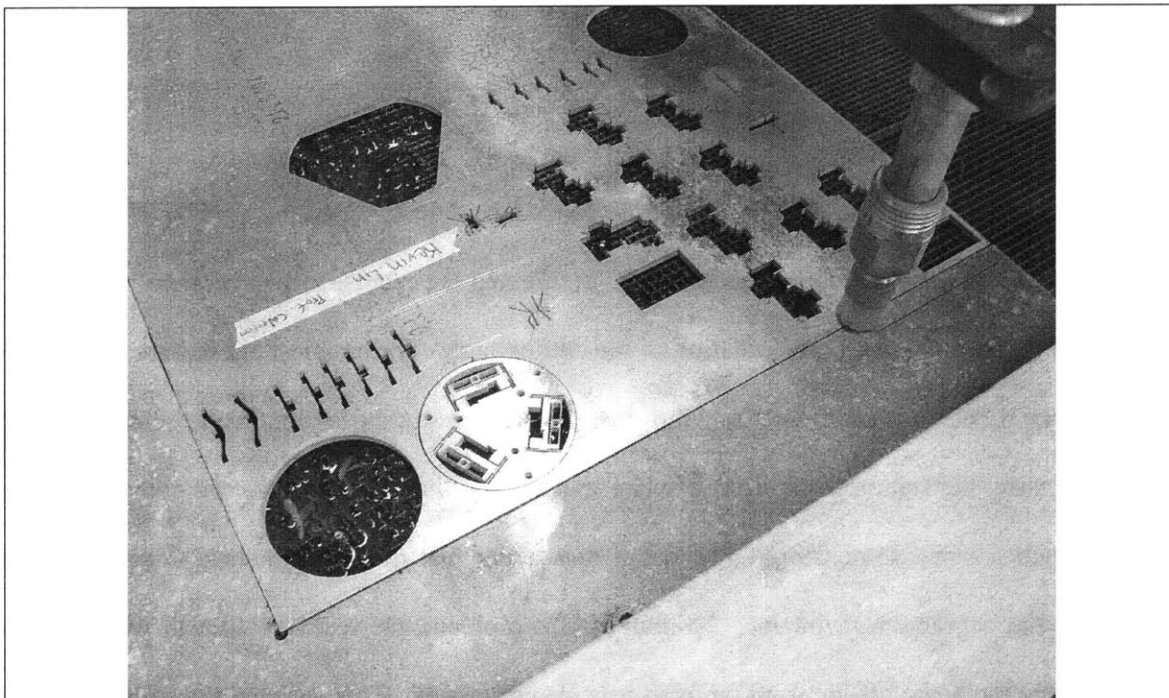


*Figure 4.1: Photograph of waterjet cutting of aluminum in-plane motion component for the nanopositioner. The smallest cut feature size is the same as the waterjet beam diameter.*

### **4.3 Assembly**

As shown in the error budget results, careful assembly of the different components was important to minimizing the initial accuracy errors for the nanopositioner. The general

assembling approach was to first make sure that component interfaces were deburred and cleaned before bonding it to other components. Secondly, the symmetry was preserved as best as possible by aligning identical components in exactly the same manner and tightening the components together gradually in sequence. Designing the different components to be perfectly constrained helped ensure that the assembly process did not deform any of the components prior to operation.

More specifically, the most critical tasks during the assembly process for the nanopositioner were preloading the actuators consistently and installing the HexFlex without over-constraints. The challenge with preloading the actuators was to obtain a good grip on the small component features to allow the actuators to slide into place, while avoiding plastic deformation of the compliant mechanism. This was a critical task, because the consistency of the preload, as mentioned in Chapter 3, would affect the consistency of the output motion due to change in contact stiffness. Also, there were four actuators that needed to be separately installed, so this became the main bottleneck of the assembly process. The solution for dealing with this issue was to design tapped threaded holes at the actuator-mechanism interfaces that allowed clamps to grip onto screws and controllably widen the slot for the actuator. The actuator slot in the mechanism could then be widened consistently to ensure proper preloading and installment of the actuators.

Installing the HexFlex required sliding the three actuation tabs along the dowel pins while bolting down the remaining three grounded nodes. The actuation interface design was described in detail in Chapter 2. The assembly challenge was to install the HexFlex without introducing stresses due to misalignments from mounting all tabs and nodes simultaneously. To remedy this

potential problem, the actuation interface on the HexFlex was designed to be a compliant perfectly constrained slot. Its compliant nature enabled the slot to be elastically widened during installation to avoid sliding resistance from the dowel pin. As a result, the HexFlex could be bolted down without adding extra stresses and then bonded to the dowel pin appropriately.

Practical assembly issues were taken into consideration during the design process, which helped deal with the challenges just mentioned and also reduced assembly time. In general, the design was modularized into sub-assemblies that could be assembled independently and then integrated into the device. The modularity provided the benefit associated with interchangeable parts. Different sub-assemblies could be redesigned or replaced without rebuilding the entire assembly.

# CHAPTER 5

## 5 Performance Characterization

This chapter provides a discussion of the experimental approach that was used to characterize the performance of the positioner. It describes the capacitance probe based metrology system that was built for experimentation and the testing procedure. The goal of the experiment was to determine how well the nanopositioner met the functional requirements. Also discussed are special issues concerning the limitations of the experimentation.

### 5.1 Review of Performance Metrics

A bench top experiment was conducted to provide a worst case scenario of environmental noise that would be encountered in an SEM. SEM chambers are supported by an air table. This isolates the positioner from vibrational noise that originates from the outside environment, especially ground vibration. Unlike optical benches, SEM chambers are kept at high vacuum, meaning few particles would interact with the device inside the chamber. Sources of noise from typical bench top environments, such as air flow and heat conduction and convection, either do

not exist or are negligible in an SEM chamber. Thus, noise factors from the bench top environment translate to the SEM chamber environment as an upper bound on what would actually be observed and experienced. Table 5.1 also explains the experimental approach to obtaining the metric values.

**Table 5.1: Review of performance metrics and their experimental bench top approach.**

Performance Metric	Experimental Procedure
Range	Map out the workspace envelope by cycling from 0% to 100% actuation in all 4-axis of motion.
Resolution	Apply smallest incremental voltage to get clear incremental movement along each axis.
Repeatability	Repeatedly apply and remove incremental voltage to determine how well the positioner returns to the same position along each axis.
Accuracy	Assuming a linear relationship between actuation voltage and output motion, actuate accordingly to predetermined positions in the workspace. Track how closely actual position matches the predicted position.
Dynamics	Ping the device by inducing a mechanical impulse and measure the subsequent vibrational behavior (analyze using FFT).

## 5.2 Metrology System Design

A metrology system was designed and built for measuring 6-axis motion for the nanopositioner. The metrology system consisted of 6 independent capacitance probes, the stage for positioning the capacitance probes, the target piece, the electronic drivers for operating the capacitance probes, and the data acquisition system for collecting data. Figure 5.1 is a photograph of the overall metrology system conducting experiments on the nanopositioner.



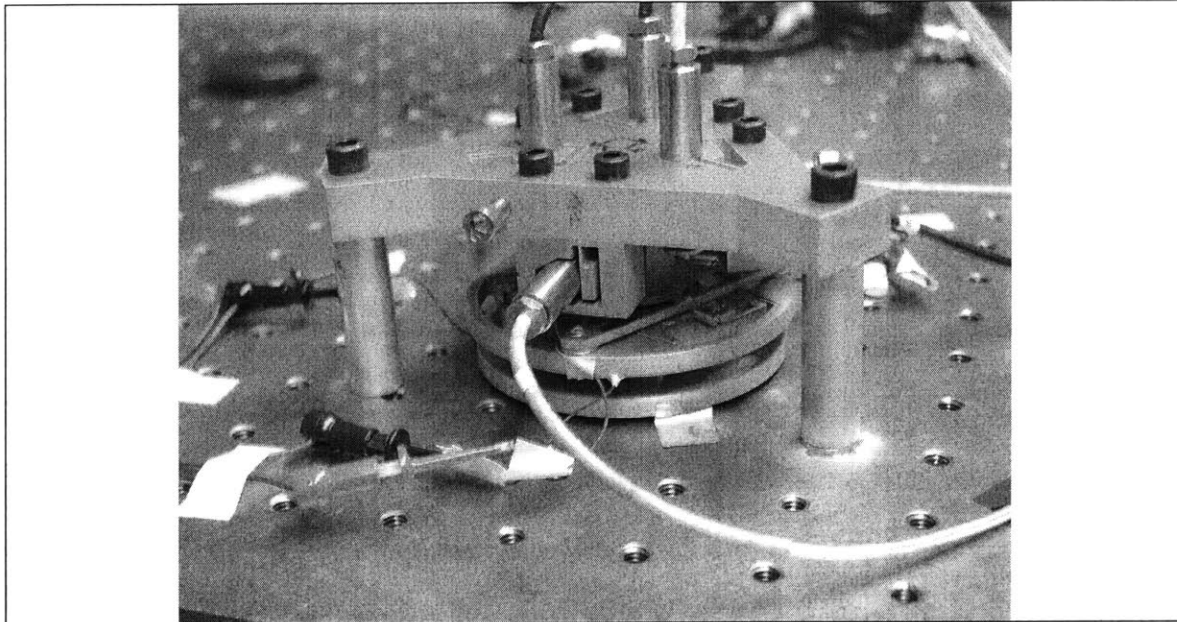


*Figure 5.1: Photograph of metrology system conducting experiments on the nanopositioner. The system includes the capacitance probes, the capacitance probe stages, the target piece, the capacitance probe driver, and the data acquisition system.*

Capacitance probes were chosen because they are compact, durable and offer a non-contact method of measuring displacement. In addition, capacitance probes require a simple and flexible setup where only a flat conductive target is needed to be placed perpendicular to its measuring axis. Their resolution depends on the noise from the data acquisition system. In this setup, the sensitivity was rated at 1 V per 100  $\mu\text{m}$  at the typical resolution setting and 1 V per 20  $\mu\text{m}$  at the high resolution setting. The flexibility and ease of use of capacitance probes outweighed the benefit of higher resolution (nanometer resolution) from laser interferometers that required a more complex setup, especially when measuring 6 axes simultaneously.

The capacitance probe stage was fabricated from aluminum using an abrasive waterjet. The stage works in conjunction with the target piece, which is essentially an equilateral triangular shell with chamfered corners. The drawings of both the test stage and test piece are shown in Figure 5.2.

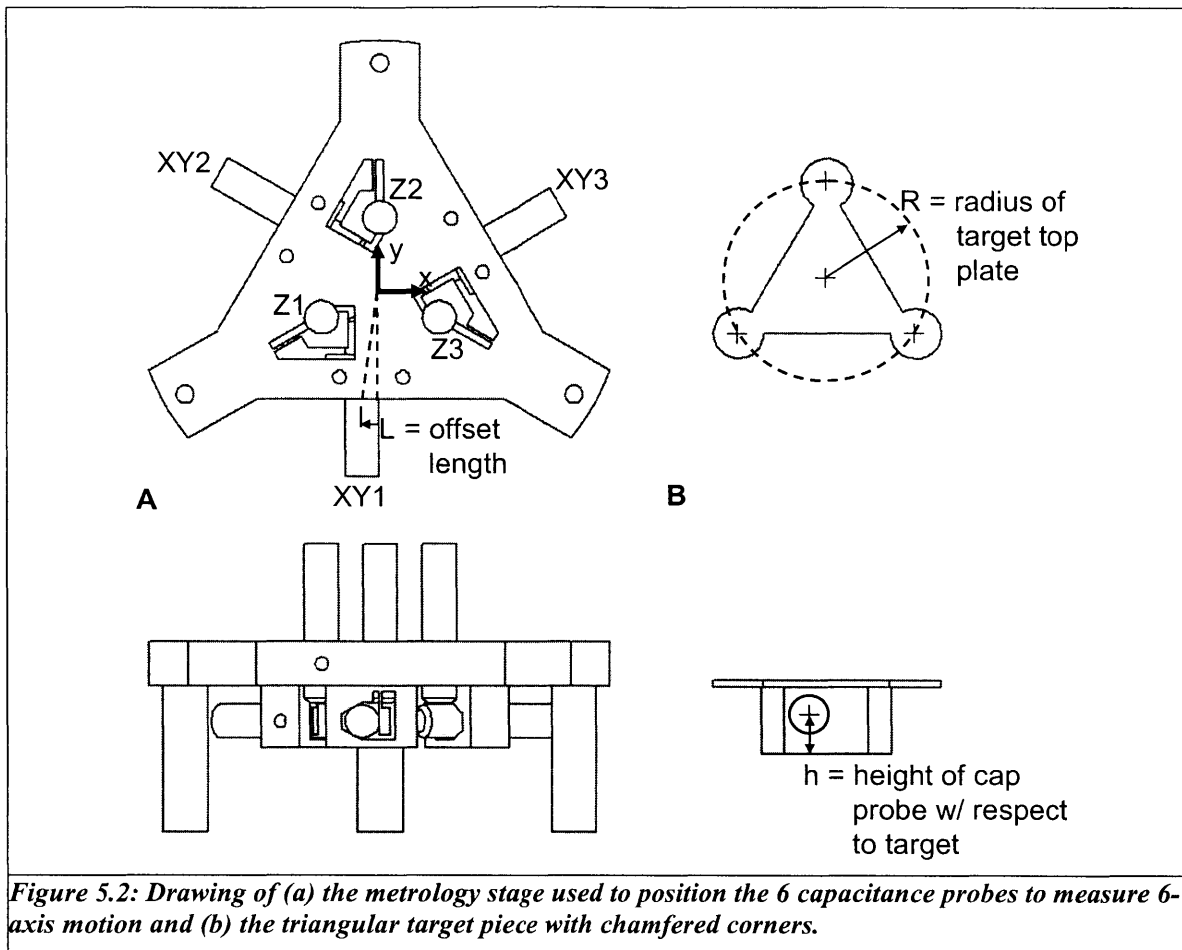


**Figure 5.2:** Drawing of (a) the metrology stage used to position the 6 capacitance probes to measure 6-axis motion and (b) the triangular target piece with chamfered corners.

Three capacitance probes were placed perpendicular to the top plane of the target at the three corners of triangular shaped target. These probes measured the three out-of-plane motions ( $\delta_z, \theta_x, \theta_y$ ). The other three probes were each placed in-plane, perpendicular to one side of the triangular target. The probes were offset from the midpoint of the triangular side in order to track  $\theta_z$  motion in addition to  $\delta_x$  and  $\delta_y$ .

The data collected from the capacitance probes were voltage readings that needed to be linearly converted to length measurements in microns. After they were converted to length measurements, they needed to be transformed from their independent coordinate systems to a global Cartesian coordinate system. To do this, the data was multiplied by a transformation

matrix that took into account how the motion in each axis contributed to the different capacitance probe measurements for the given system geometry. Figure 5.3 is a schematic that maps the placement of the capacitance probes with respect to the target piece.

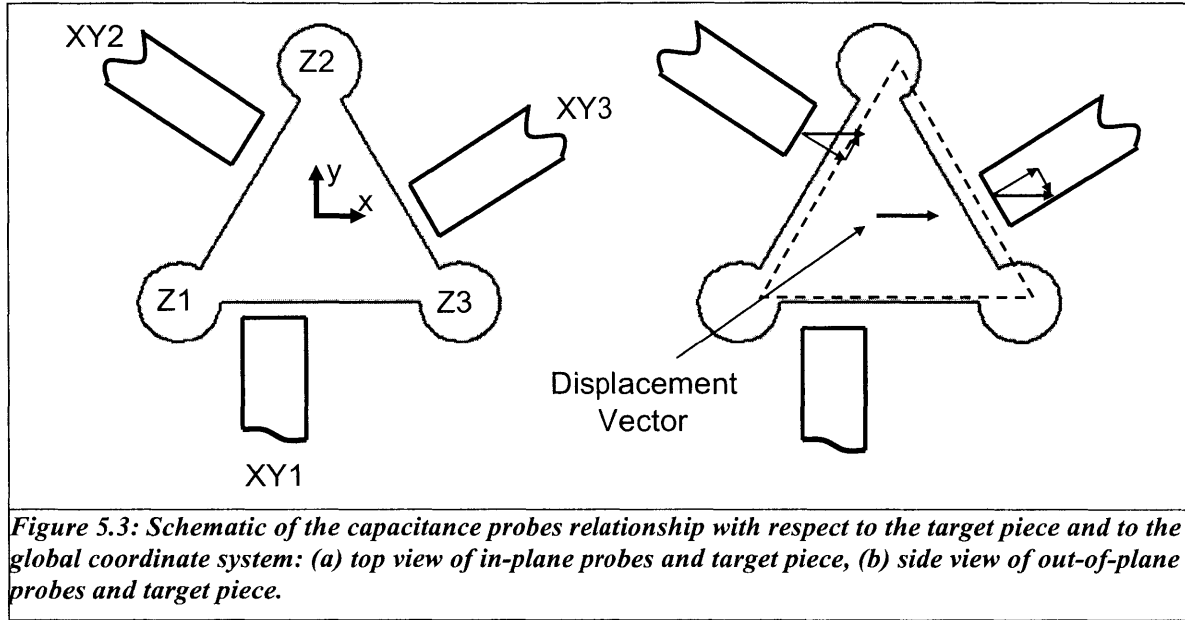


Figure 5.3: Schematic of the capacitance probes relationship with respect to the target piece and to the global coordinate system: (a) top view of in-plane probes and target piece, (b) side view of out-of-plane probes and target piece.

Equation 5.1 is the equation used to convert raw data into motion data with respect to the global Cartesian coordinate system.

$$\begin{bmatrix} xy1 \\ xy2 \\ xy3 \\ z1 \\ z2 \\ z3 \end{bmatrix} = \begin{bmatrix} 0 & -1 & 0 & h & 0 & L \\ -\cos\left(\frac{\pi}{6}\right) & \sin\left(\frac{\pi}{6}\right) & 0 & -h\sin\left(\frac{\pi}{6}\right) & -h\cos\left(\frac{\pi}{6}\right) & L \\ \cos\left(\frac{\pi}{6}\right) & \sin\left(\frac{\pi}{6}\right) & 0 & -h\sin\left(\frac{\pi}{6}\right) & h\cos\left(\frac{\pi}{6}\right) & L \\ 0 & 0 & 1 & -R\sin\left(\frac{\pi}{6}\right) & R\cos\left(\frac{\pi}{6}\right) & 0 \\ 0 & 0 & 1 & R & 0 & 0 \\ 0 & 0 & 1 & -R\sin\left(\frac{\pi}{6}\right) & -R\cos\left(\frac{\pi}{6}\right) & 0 \end{bmatrix} \begin{bmatrix} \delta_x \\ \delta_y \\ \delta_z \\ \theta_x \\ \theta_y \\ \theta_z \end{bmatrix} \quad \text{Eq.5.1}$$

### 5.3 Experimental Procedure

The general experimental procedure was summarized in Table 5.1 at the beginning of the chapter. All the metrics, with exception of the dynamic metric, involved actuating the actuators appropriately to achieve motion in each axis. The general method for collecting data was to actuate the device to a certain position where 1000 data points were collected and averaged. The decision to take 1000 data points was based on a desired tolerance of  $\pm 0.5 \text{ \AA}$  at 95% uncertainty using the Central Limit Theorem given in Equation 5.2. The variable  $S_x$  is the standard deviation of the sample data,  $n$  is the number of data points taken, and  $z$  is the erf function at 95% uncertainty.

$$tolerance = \pm z_{95\%/2} \frac{S_x}{\sqrt{n}} \quad \text{Eq.5.2}$$

The main assumptions were that the noise followed a Gaussian distribution and that enough samples were taken from the tested device at a particular moment in order to allow the standard deviation of the sample to represent the standard deviation of the population. The subsequent procedures followed the same procedure in order to map out the motion path.

Prior to the procedures described in Table 5.1, additional experiments needed to be conducted on the metrology system in order to characterize its performance. The system's electronic noise needed to be measured by measuring the analog-to-digital port signals without plugging the capacitance probe. In addition, the metrology's stability was characterized by measuring a static target over a 10 minute period inside a thermally insulated enclosure. The temperature was also monitored to gauge temperature changes and the corresponding thermal drift in the metrology system. Before measurements were taken, the metrology system and the static target were

allowed to stabilize and reach thermal equilibrium inside the enclosure. On average, it took about 15 minutes to thermally stabilize. After stabilization, the temperature stopped climbing and only fluctuated by 0.1 C. At this point, the 10 minute sample time was enough time to capture enough data where remaining thermal instabilities would only affect some of the data from that trial. The reasons for these prior experiments are given in more detail below.

## **5.4 Metrology Limitations and Issues**

Given the experimental conditions and instrumentation available to conduct the experiments, the accuracy of the results was limited to mechanical, environmental, and electrical noise.

### **5.4.1 Mechanical Limitations**

The mechanical noise included vibrational noise and misalignments between the metrology system and the target test piece. Most of the vibrational noise originated from the building's floor vibration which was about 20 nm in amplitude. To minimize the amount of noise that transferred to the experimental setup, the experiments were conducted on a self-leveling optical air table. Another source of mechanical vibrations came from the wire leads that connected the capacitance probes to the drivers and the actuator leads that supplied power to the actuators. These leads acted like hanging cantilevers that transferred vibrations to the device. For this reason, all the leads were separated to reduce the amount of hanging mass and secured to the table as rigidly possible without straining the connections.

In terms of the mechanical misalignment between the metrology system and target piece, the resulting systematic errors could be calibrated out or filtered out of the data. By mapping out the measured position of the device versus the desired position, systematic errors, such as misalignments, would appear as linear deviations from the desired position. Using this slope

from the deviating data to construct a calibration matrix, the input commands to the positioner were adjusted by multiplying it by the calibration matrix. In addition to misalignments, a rough surface finish may have also contributed to systematic errors. If the surface is rough, the capacitance probe will average the collected data. This average can shift along the same surface depending on how rough it is. If the data is repeatedly collected over the same surface, the errors due to roughness will be systematic and can be calibrated out like the misalignment.

#### **5.4.2 Environmental Limitations**

Environmental limitations mainly included air flow interacting with the device and temperature fluctuation. Air flow not only helped induce temperature changes in the device, but also added vibrations to the system. Sources of air flow included the air conditioning system in the room and people passing by the device. Thermal fluctuation of the system created thermal expansion problems that were compensated for in the design by a symmetric design, but thermal fluctuation was not uniform throughout the system. Heat concentrations could have developed from human interaction with the device or neighboring electronic hardware. To compensate for both air flow interference and thermal fluctuation, the experiments were conducted within a thermally insulated closed box. Figure 5.4 is a picture of the experimental setup underneath the thermally insulating box.

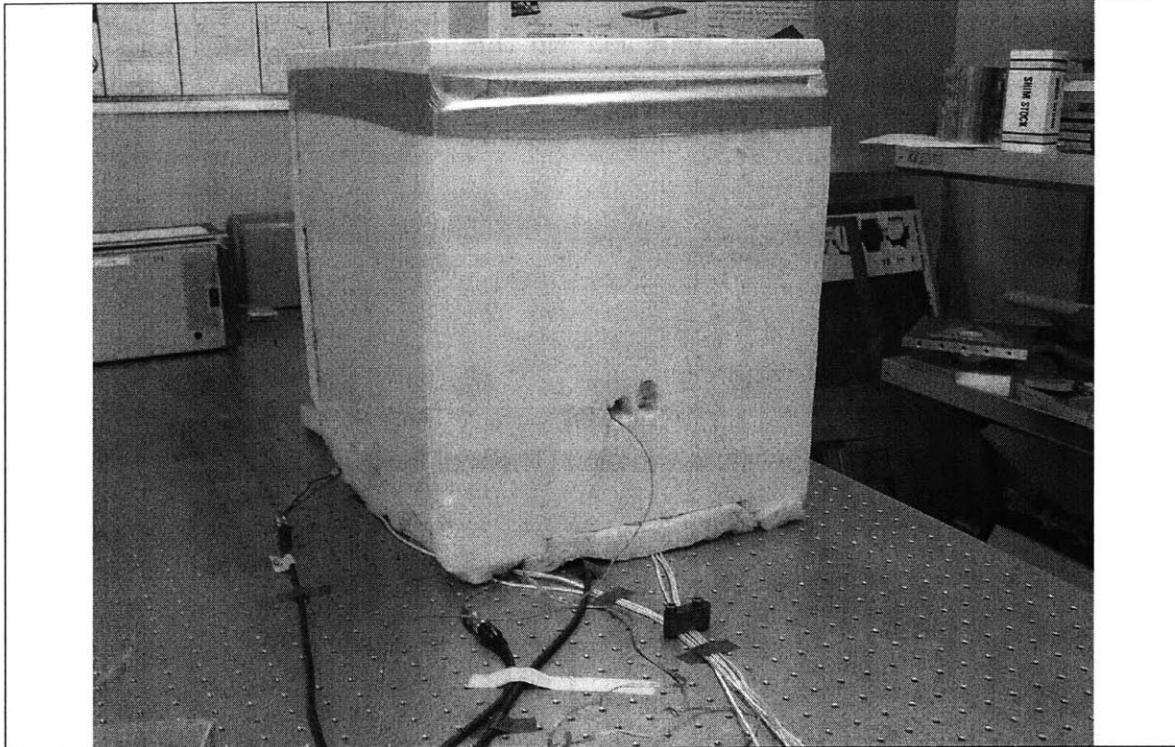
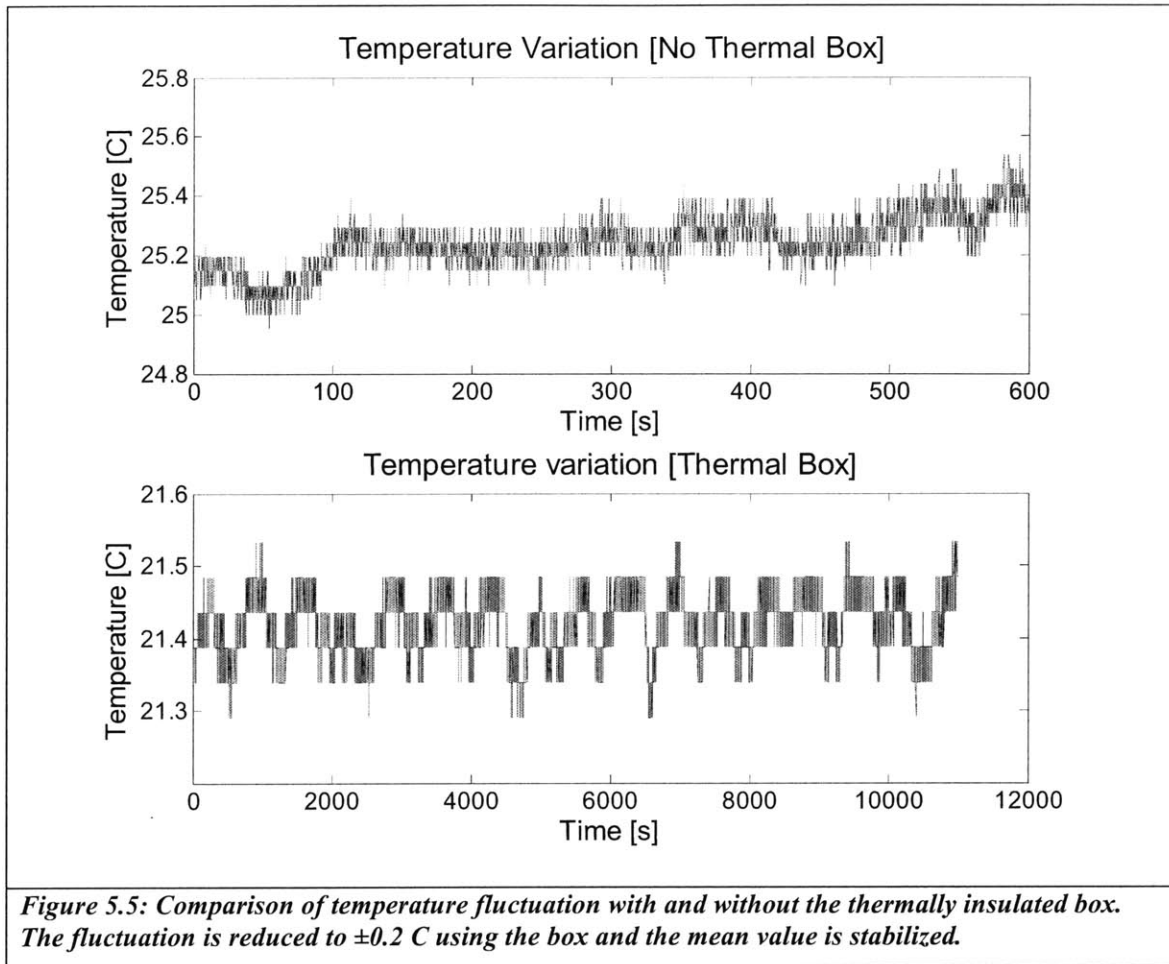


*Figure 5.4: Photograph of the thermally insulating box that covered the metrology system and the nanopositioner during experimentation.*

To characterize the effectiveness of the thermally insulated box, the temperature surrounding the positioner was monitored with and without the box. The resulting temperature data showed that the box reduced temperature fluctuations by half to about  $\pm 0.2$  C and the mean temperature was stabilized, as seen in Figure 5.5.



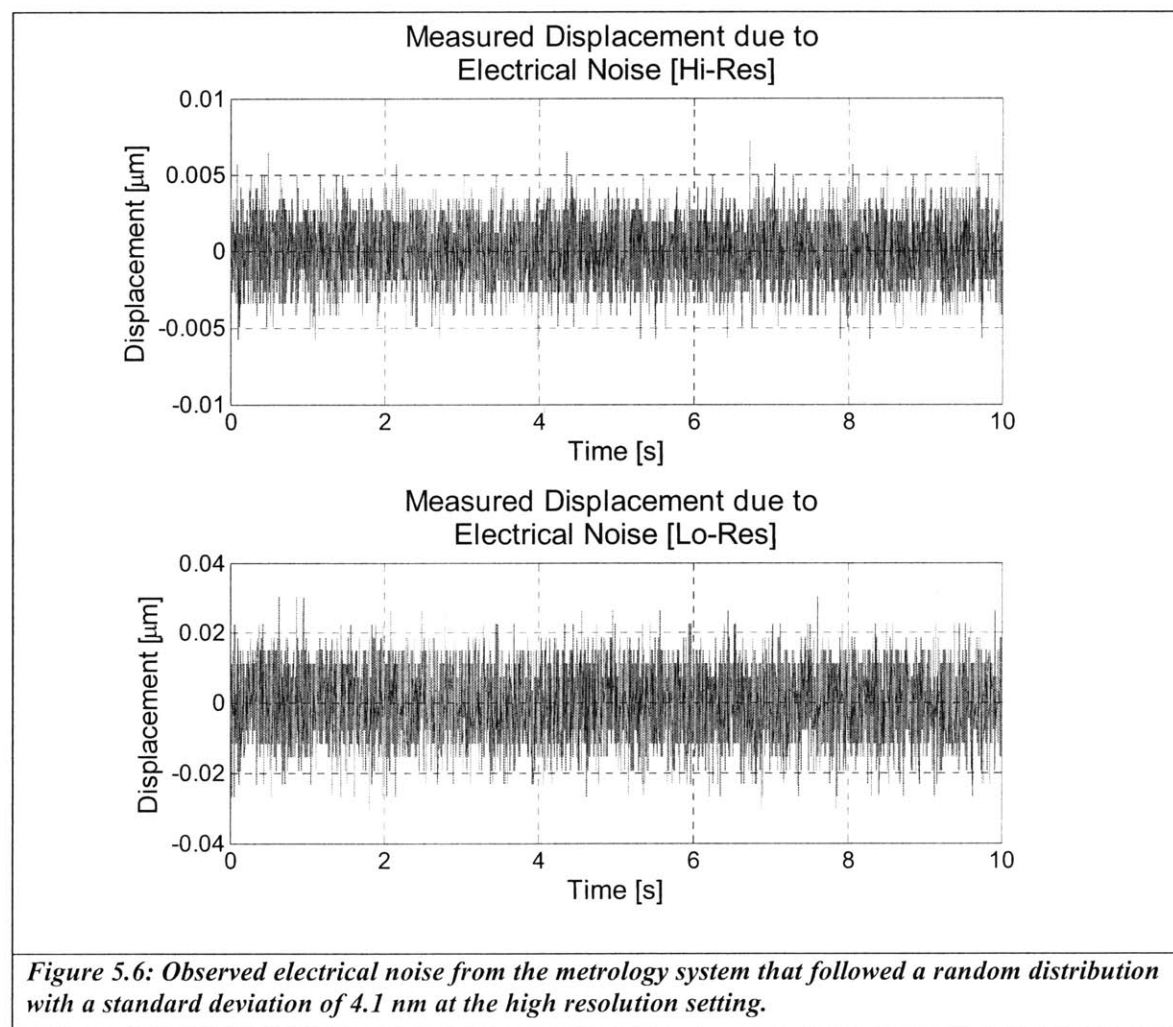
### 5.4.3 Electrical Limitations

The electrical limitations came from the electrical components that were used to drive the positioner and to measure its performance. Essentially, any electrical component in the metrology loop limited the accuracy of the open-loop control and data collection. The reason was because the actuation and sensing were based on producing and collecting sensitive voltage signals. The electrical components of the system were shielded from each other and from the environment to minimize electrical noise.

Theoretically, the 16-bit data acquisition system and the capacitance probe system, which had a sensitivity of one volt per 20  $\mu\text{m}$  (high resolution setting), yielded a 6 nm measurable resolution.



This did not take electrical noise into consideration, which superimposed another 4.2 nm of noise at the high-resolution setting and 21 nm of noise at the low-resolution setting. The magnitude of the noise was quantified from the data that was collected from recording the voltage fluctuation without attaching any capacitance probes. The measured data for both the high and low resolution settings are shown in Figure 5.6, and show that the noise follows a random distribution about a mean value.



The random noise distribution could be compensated for by averaging the data at different points to obtain a measurable resolution below the noise limitations, as mentioned previously in this chapter.

The output voltage used to drive the actuators also deviated from ideal behavior. The largest error was 0.043 V at zero volt input. This error decreased as the input voltage increased, as seen in the Figure 5.7, which compares the measured voltage with the desired input voltage.

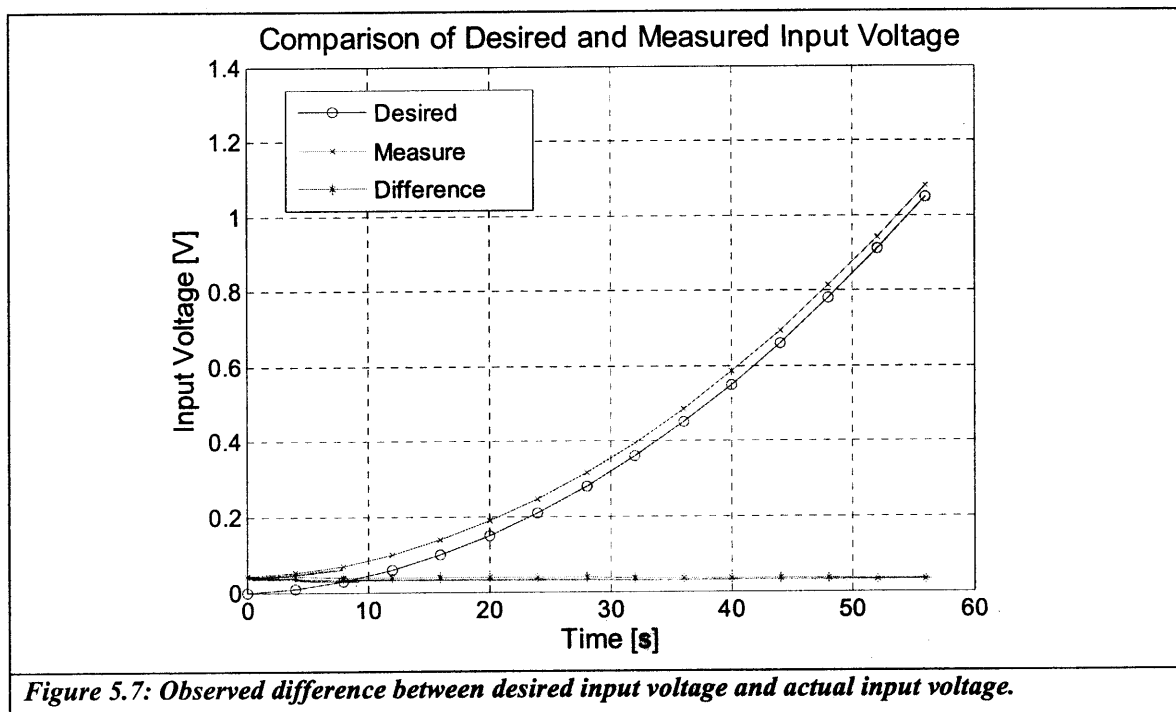


**Figure 5.7: Observed difference between desired input voltage and actual input voltage.**

The main reason for the error was the amplifier that multiplied the voltage from the computer I/O block by a gain of 10 in order to achieve the 0-100 V driving range for the actuators. As a result, errors were multiplied by the gain. In addition, the amplifier also added its own noise to the system. To minimize this error, actuating voltages were based about 50 V (50% saturation voltage), which avoided the lower and upper operating voltage limits.

# CHAPTER 6

## 6 Performance Characterization of Nanopositioner

This chapter describes the experimental results according to the metrics and procedures given in Chapter 5. In this chapter, the possible reasons for discrepancies between predicted performance and measured performance are discussed. The reasons are used to evolve the design for the next version of the nanopositioner.

### 6.1 Initial Results for Completely Assembled Nanopositioner

The initial measurements of the completely assembled 4-axis nanopositioner showed large parasitic errors that were larger than the desired range of motion for particular axes, primarily in the out-of-plane axis. The range for each axis and the associated parasitic errors are given in Table 6.1.

*Table 6.1: Range of motion and accompanied parasitic error motion (non-bold) associated with actuation in each of the four-axis. The parasitic errors are comparable, or larger than, the desired actuation range. The range of motion in the actuation axis is in bold.*

Actuation Axis (Predicted Range)	Range of motion X-axis [ $\mu\text{m}$ ]	Range of motion Y-axis [ $\mu\text{m}$ ]	Range of motion Z-axis [ $\mu\text{m}$ ]	Range of motion $\theta_z$ -axis [ $\mu\text{rad}$ ]
X-axis (4.5 $\mu\text{m}$ )	<b>2.0</b>	2.0	0.2	60
Y-axis (3.9 $\mu\text{m}$ )	1.7	<b>3.0</b>	0.06	13
Z-axis (1.5 $\mu\text{m}$ )	1.4	1.0	<b>0.5</b>	4
$\theta_z$ -axis (150 $\mu\text{rad}$ )	0.5	1.5	0.02	<b>100</b>

The range was the one performance metric that was not limited by the resolution of the metrology system due to its range of at least 1  $\mu\text{m}$ , which was more than 10 times the measuring noise in system. The hypothesis for the source of error was that the three supporting flexures were applying unequal stiffnesses to the system. As a result, the out-of-plane and in-plane modules were separated and tested independently to isolate the performance data from possible assembly errors between modules. The metrics for testing remained the same, because the modules were designed to be decoupled, with the exception that the out-of-plane range did not take the flexure supports into consideration. The independent results would remain relevant for the purpose of building the 6-axis version of this prototype, because the 6-axis version would be a combination of the different components. For the testing, first the out-of-plane module was tested, followed by the in-plane module.

## 6.2 Out-of-Plane Module Results

The out-of-plane module included the diamond-shaped CM attached perpendicularly in series to the half-diamond CM. The two mechanisms transmitted the in-plane actuator input displacement into the out-of-plane direction. When disassembled from the in-plane module, the motion of the mechanisms was not impeded by the stiffness of the three flexure supports that help attach the

two modules together. As a result, the desired range of motion of the unassembled out-of-plane module was 1.5  $\mu\text{m}$  instead of 1.0  $\mu\text{m}$ , according to the design model. The resolution was also affected by the change in stiffness of the system, thus it also scaled by 1.5 times. On the other hand, the repeatability and accuracy metrics remained the same, because they were based on relative motion and on the observed displacement to voltage relationship, respectively. The measured performance resulting from the procedures explained in Table 5.1 are shown in Table 6.2.

*Table 6.2: Summary of the measured performance of the independent out-of-plane module that was separated from the in-plane module. The desired metric values are adjusted for the range and resolution due to the absence of flexure supports*

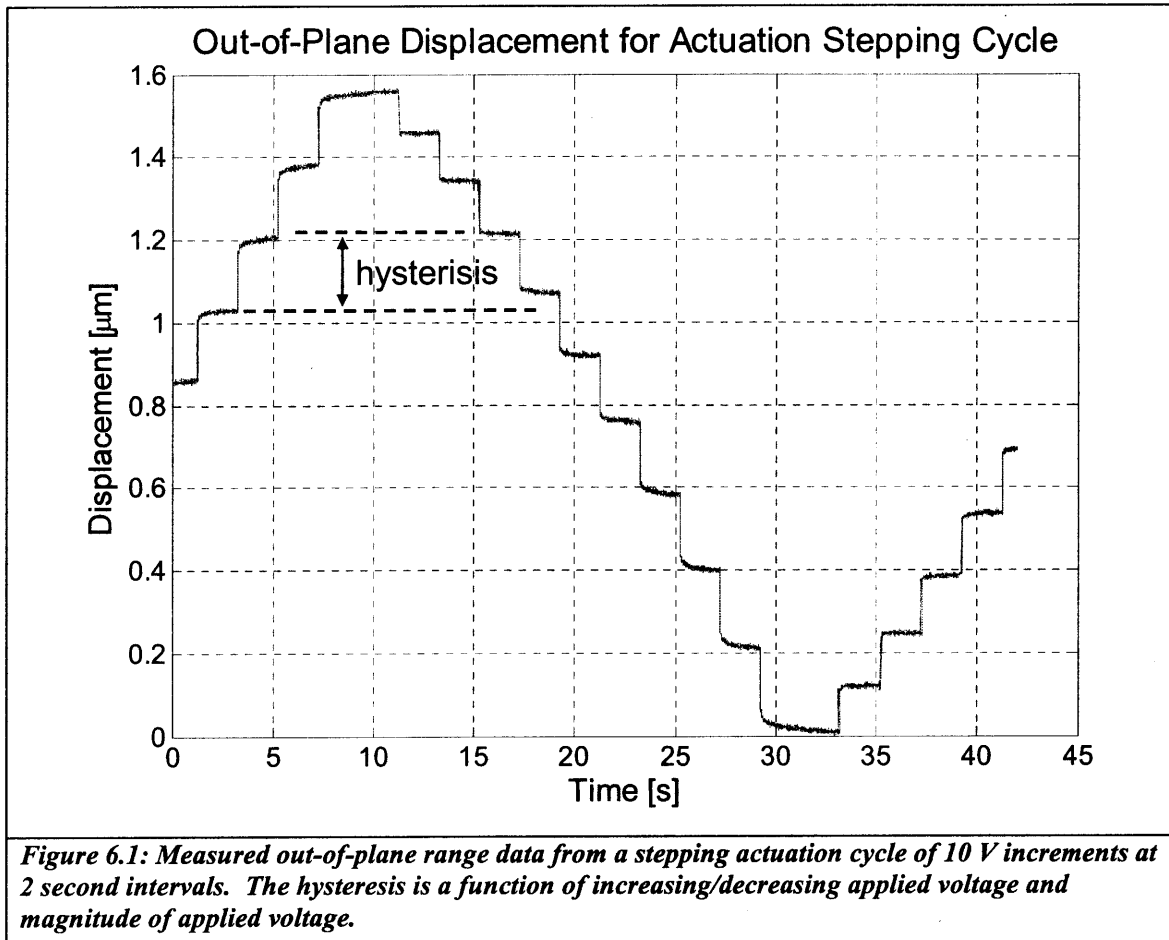
Metric	Desired	Actual
Range	1.50 $\mu\text{m}$	1.55 $\mu\text{m}$
Resolution	1.5 nm	2 nm
Repeatability	1 nm	1.2 nm
Accuracy	10 nm	233 nm

Overall, the measured performance of the out-of-plane module matched within 20% the desired specifications, except for the accuracy. The 20% error is acceptable, because the error translates into only fractions of a nanometer. In contrast, the accuracy was approximately 23 times the desired specification. Much of this value is attributed to the hysteresis intrinsic to piezo-electric actuators.

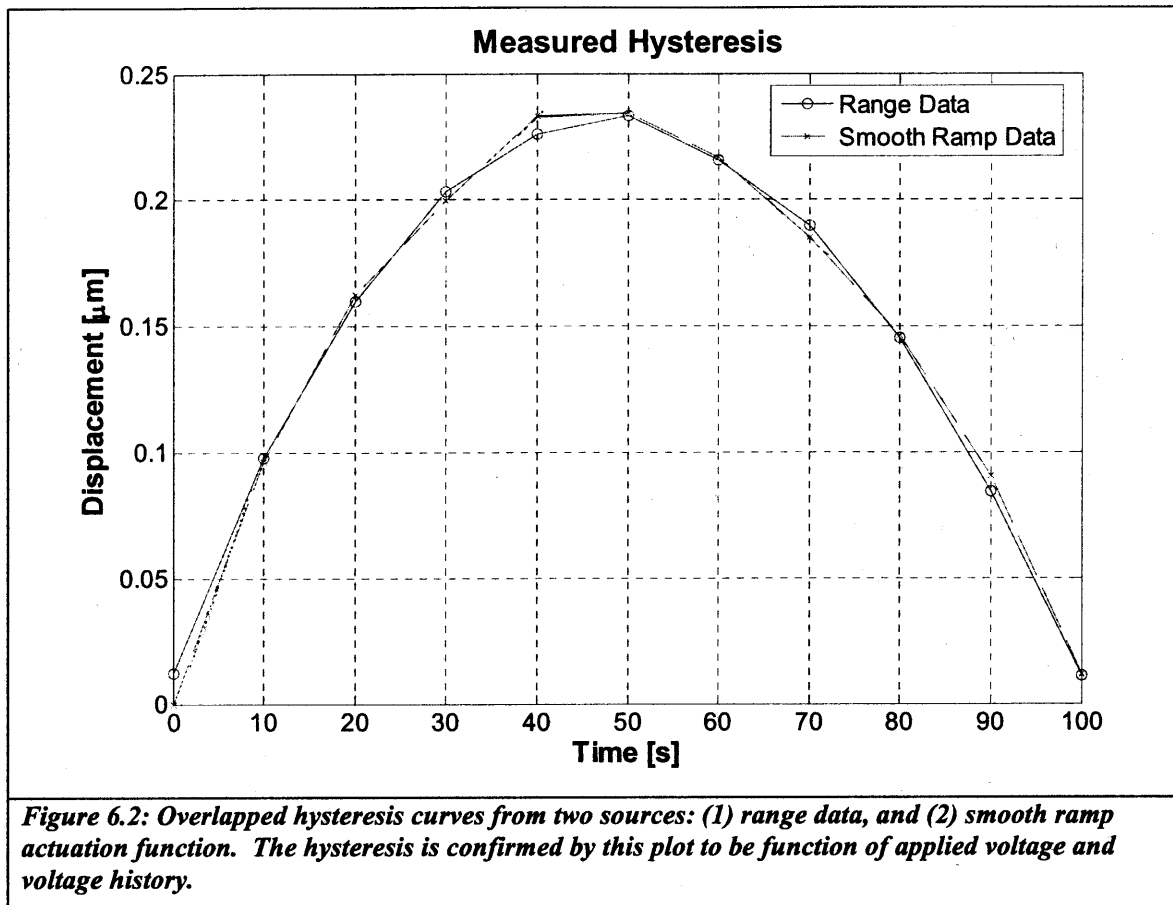
### 6.2.2 Hysteresis

The hysteresis caused the actuator to reach a different position at the same actuation voltage depending if the controlling voltage was increasing or decreasing. In addition, the hysteresis was

also a function of the magnitude of the applied voltage. The hysteresis was apparent in the range data, seen in Figure 6.1 as the difference in displacement between same applied voltages.



The maximum hysteresis was measured to be 233 nm at 50% applied voltage with full voltage actuation, and was present in all the data taken. To characterize the hysteresis, the hysteresis observed in the range data was compared with the hysteresis due to a smooth ramping actuation function. The two hystereses were compared with respect to applied voltage and are seen in Figure 6.2 to closely match within nanometers. Both the repeatability data and the range data showed a closely matched hysteresis behavior.



The hysteresis degrades the accuracy of the mechanism according to the curves shown in Figure 6.2. A possible open-loop control solution is to always apply the saturation voltage and then decrease down to the desired voltage. This method ensures that the output displacement is always on the upper bound of the hysteresis curve. However, this method is not suitable for a positioner that is used for deforming test CNT specimens, because the actuators are always engaged and will overshoot the desired position using this method. The desired position must be reached from any point in the workspace through the shortest direct path. As result, the only alternative solution to the hysteresis is implementing a closed loop control system that will adjust to the inaccuracies by using feedback from a system of sensors.

### 6.3 In-Plane Module Results

Unlike the out-of-plane module that exhibited motion in a single axis, the in-plane module was capable of 3-axis motion; therefore, the metrology stage and target piece described in Chapter 5 were used. All 6 capacitance probes were used to obtain motion data from the module, which was converted into a global coordinate system using the transformation matrix given in Equation 5.1. The performance results are listed in Table 6.3.

**Table 6.3: Experimental data obtained from the in-plane module using 6 capacitance probes.**

Metric	X-axis		Y-axis		$\theta_z$ - axis	
	Desired/ Predicted	Measured	Desired/ Predicted	Measured	Desired/ Predicted	Measured
Range	4.5 $\mu$ m	4 $\mu$ m	4 $\mu$ m	2.9 $\mu$ m	150 $\mu$ rad	120 $\mu$ rad
Resolution	1 nm	10 nm	1 nm	10 nm	1 $\mu$ rad	0.1 $\mu$ rad
Repeatability	1 nm	13 nm	1 nm	10 nm	1 $\mu$ rad	0.5 $\mu$ rad
Accuracy	10 nm	208 nm	10 nm	153 nm	10 $\mu$ rad	9 $\mu$ rad

#### 6.3.2 Range

The range of this in-plane data is similar to the range of the in-plane data collected from the assembled positioner; however, the parasitic errors are on average 10 times smaller than the previous parasitic errors. To further investigate this difference, the parasitic data was plotted with respect to the desired output to map out the trend. This was part of the calibration step that compensated for any systematic errors, such as misalignments in the metrology system or in the modules. Figure 6.3 to Figure 6.5 are plots of the range of motion in the x, y, and  $\theta_z$  directions and the parasitic errors associated with each.



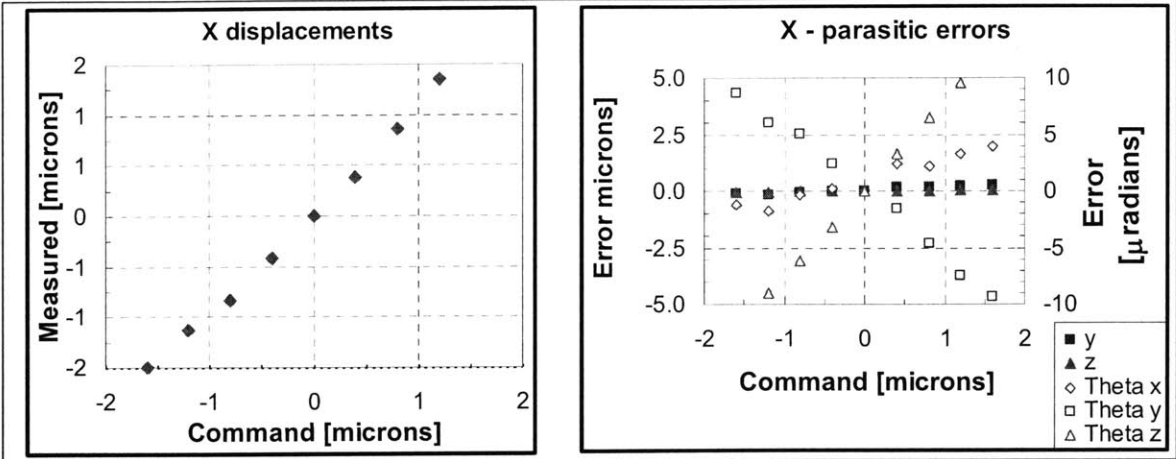


Figure 6.3: Displacement motion in X-axis and associated parasitic errors.

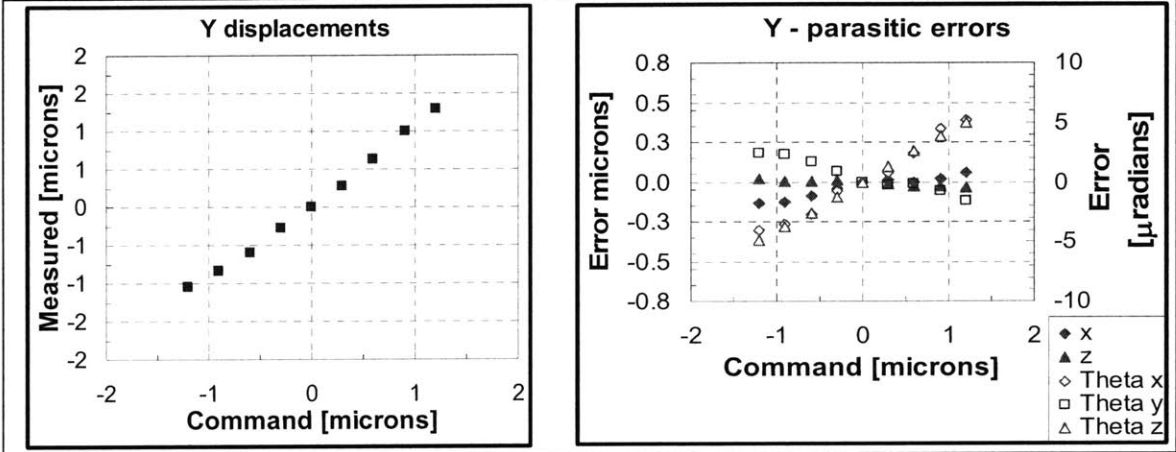


Figure 6.4: Displacement motion in Y-axis and associated parasitic errors.

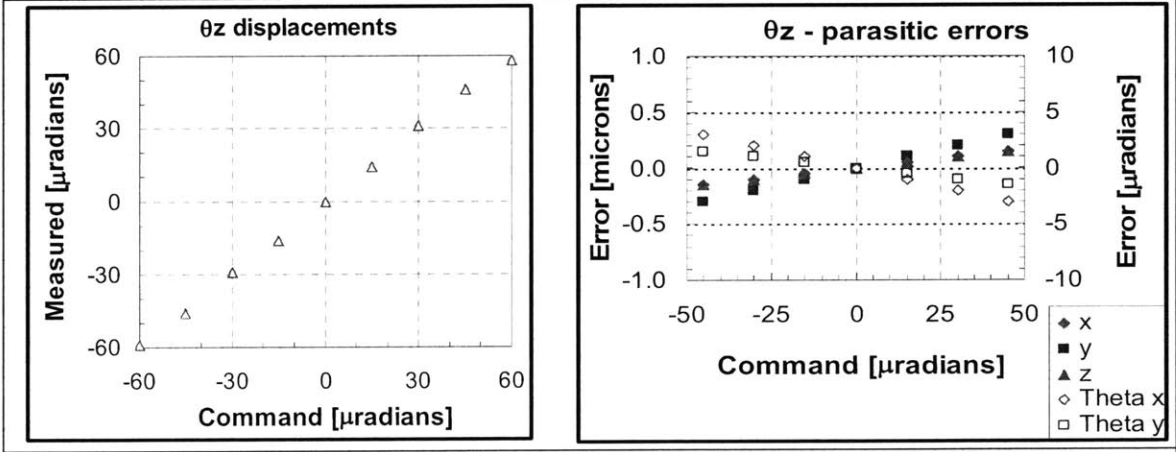


Figure 6.5: Displacement motion in  $\theta_z$ -axis and associated parasitic errors.

The parasitic errors in almost all the axes of motion show a linear trend, although some are more linear than others. The linear trend is an indication that the parasitic errors are systematic in nature for this system of small displacements where the small angle approximation applies. As a result, their effects can be compensated for by calibrating the system input to take into account the slope of their trend.

The range of motion in the x and y-axis were both less than the predicted range of motion, yet still satisfied the required 1  $\mu\text{m}$  requirement. The rotational range was also 20% less than the desired target. Although the root cause has not fully been verified via experimentation, the most probable cause consists of a combination of the following:

1. The contact forces between different moving components were not perfectly perpendicular leading to forces that acted on the epoxy adhesive that surrounded the contact surfaces. The adhesive is less stiff than the components and the contact stiffness, which resulted in loss of transmitted displacement from the actuator to the component. For example, the taper due to the waterjet cutting, illustrated in Figure 2.8, partially transmits the in-plane force from the actuator in the out-of-plane direction. This out-of-plane force is then transmitted to the adhesive that surrounds the line contact around the dowel pin.
2. Modeling inaccuracies due to constraints approximations. An example of a constraint approximation was the modeling of the actuation tab with radially compliant beams only at tabs that were not being actuated, as illustrated in Figure 2.6. This was done to avoid

more complex models that included more compliant beam elements that would promote greater inaccuracies.

3. Modeling inaccuracies due to linear approximation used in both CoMeT and ComosWorks. These inaccuracies would account for up to 5% of the observed error.

### **6.3.3 Resolution and Repeatability**

The resolution and repeatability for the two translational axes exceeded the one nanometer requirement, while the rotational resolution satisfied the functional requirement. The source of the problem was primarily traced back to the surface finish of the target piece. The target piece was constructed using waterjet cutting; however, the surface finish from waterjet cutting is course, up to a few 100  $\mu\text{m}$  in variation, due to the use of abrasive garnet that is mixed in turbulent jet stream. The course surface finish required subsequent polishing of the target surfaces by hand, yet the polishing was kept to a minimum to avoid degrading the flatness of the surface. The resulting surface finish is shown in Figure 6.6.

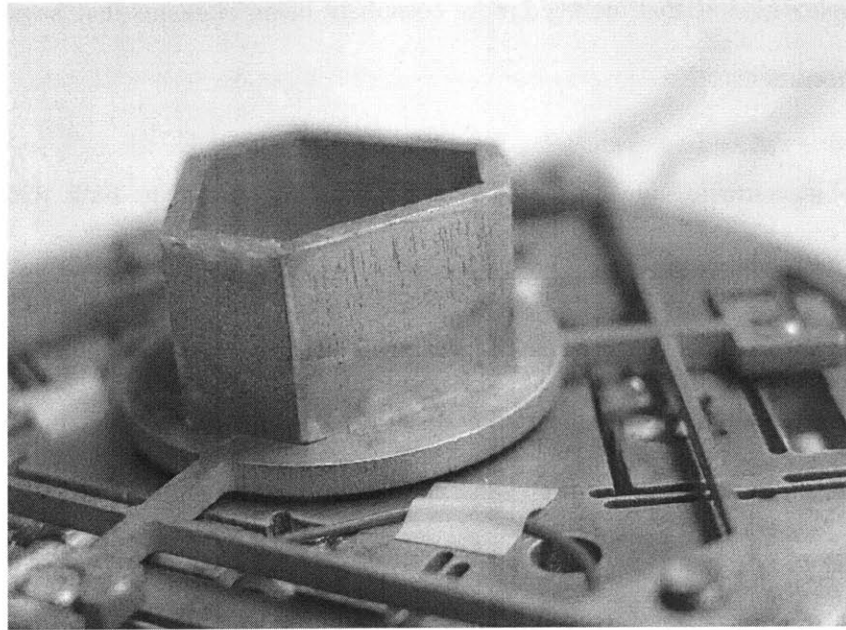


*Figure 6.6: Close-up picture of surface finish of target piece after waterjet cutting and hand polishing.*

The original assumption was that the surface defects would average out evenly across the capacitance probe's sensing area; therefore, as long as the surface was flat, the defects would not degrade the measurement. Although the polishing produced a reflective surface, the deeper surface defects from the waterjet still remained. These defects were responsible for introducing measurement errors on the order of nanometers. These errors were on the same order of the resolution and repeatability, which translated into large errors when converting the raw data from the metrology coordinate system to the global coordinate system. The effect is most noticeable when the target piece moves laterally (perpendicularly) with respect to the axis of the capacitance probes, because the probe measures changing surface features. Figure 6.7 shows the raw data that was gathered from two of the in-plane capacitance probes (Cap Probe #2 and #3) in response to an increasing staircase function to determine the resolution.

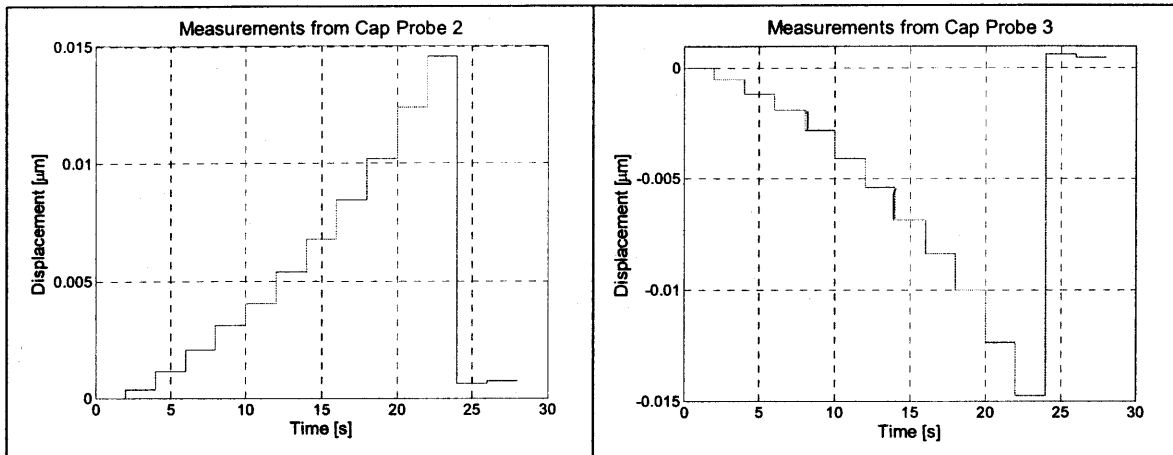


**Figure 6.7: Raw capacitance probe data from two in-plane probes that show the response to an increasing staircase input function.**

The resolution appeared to be sub-nanometer; however, when converting the data into the global coordinate system, inaccuracies from the other four probes degraded the converted resolution. Figure 6.8 is a plot of the resulting resolution in the x-direction, which is irregular compared to the staircase responses from Figure 6.7.

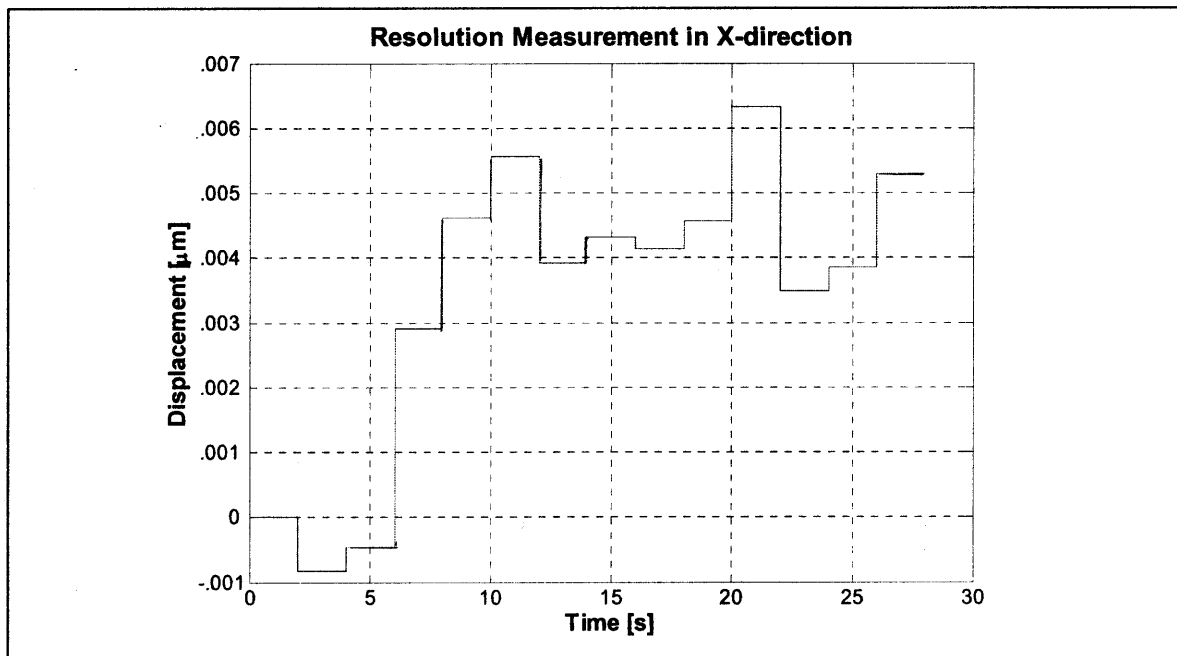


**Figure 6.8: Resulting x-direction response after transforming the capacitance probe data into the global coordinate system.**

In this example, the third in-plane capacitance probe (Cap Probe #1) took measurements as the target piece moved laterally with respect to its axis, contrary to the relative motion of the target piece to Cap Probe #2 and #3, which had a large component along the primary axes. Other contributing factors included the nanometer scale inaccuracies due to the limited sensitivity of the metrology system and due to the electrical noise.

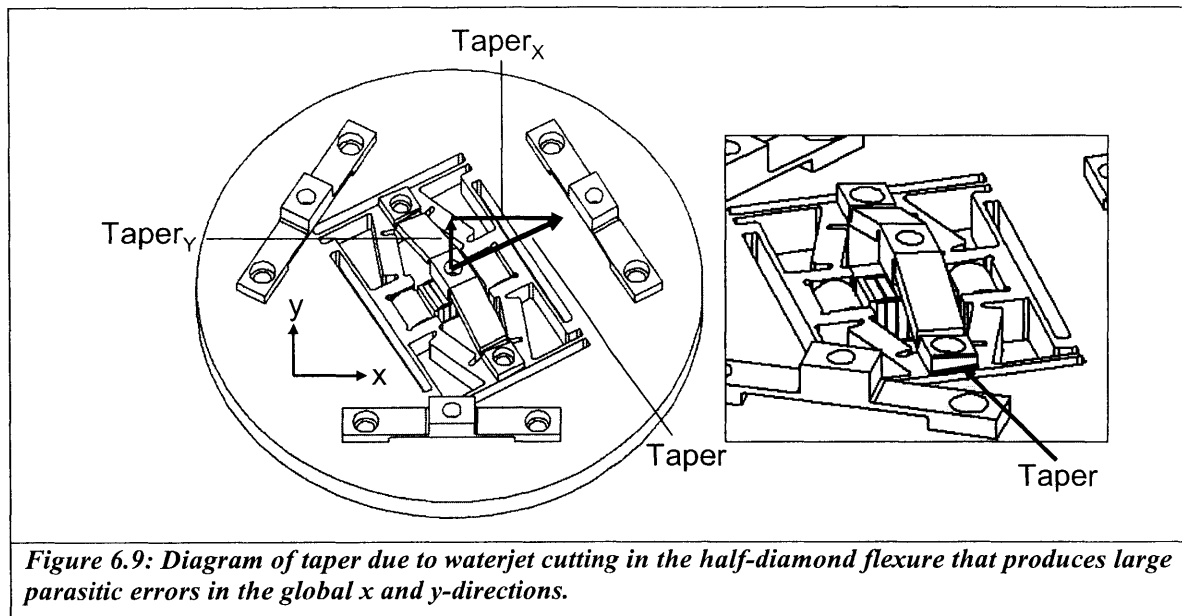
#### **6.3.4 Accuracy**

The measured accuracy of the in-plane performance was many times the desired accuracy. The main reason for this consistent inaccuracy was due to the hysteresis from the piezo-electric actuators. The relationship between the hysteresis and the accuracy is similar to the hysteresis observed in the out-of-plane performance, and is explained in detail in section 6.2.2 of the chapter.

### **6.4 Assembled Nanopositioner Results**

#### **6.4.1 Performance Results**

The nanopositioner's decoupled design between the in-plane and out-of-plane modules allowed the results from the individual testing to predict the overall performance of the completely assembled device; however, the initial results showed that the out-of-plane performance differed substantially from the predicted metrics, as shown in Table 6.1. The out-of-plane behavior was characterized by large parasitic errors that resulted in its reduced range of motion. The parasitic errors were caused by the taper in the out-of-plane half diamond flexure. This taper caused the actuation direction to tilt, which caused the symmetrically positioned flexure supports to apply asymmetric reaction forces to the actuation direction. The result was displacement in the direction of the taper, as shown in Figure 6.9.

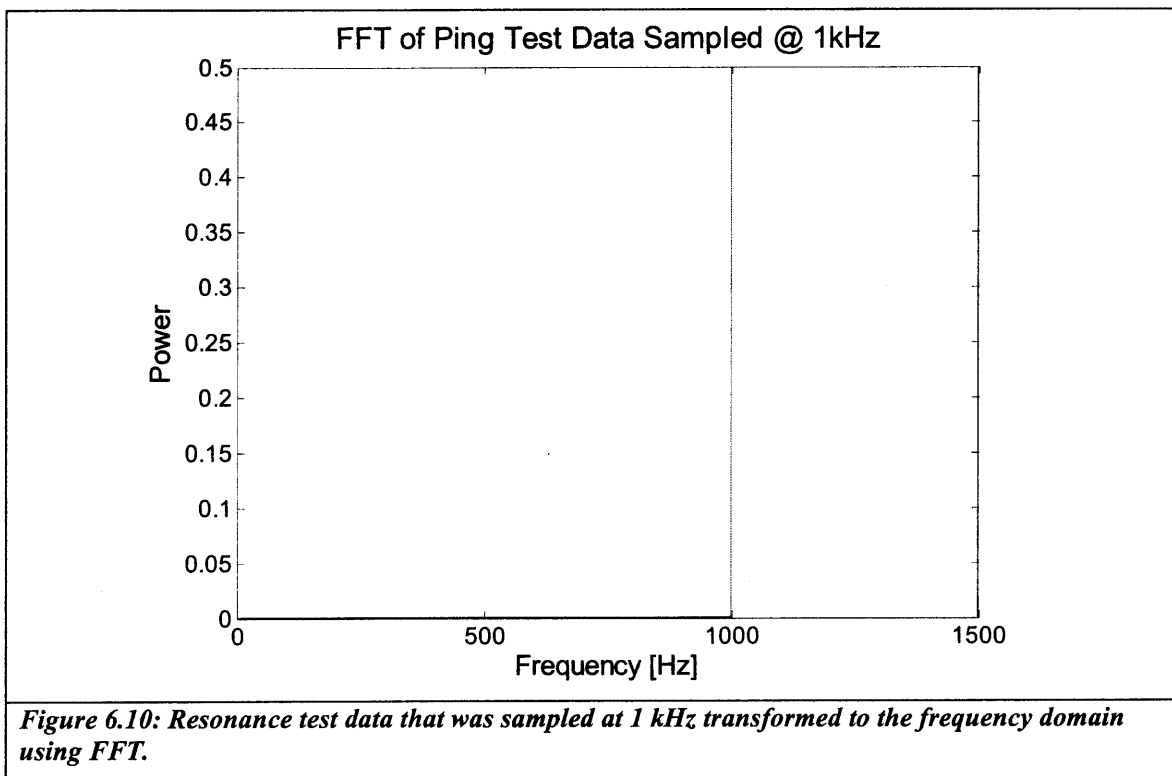


The parasitic displacements in the x and y-directions caused by the taper were evident when actuating the out-of-plane actuator. For the experimental setup, the nanopositioner was oriented as shown in Figure 6.9; therefore, the tilt from the taper caused the parasitic motion in the x-direction to be about 1.73 times that of the y-direction, which is closely matched by the values given in Table 6.1.

The parasitic error due to the taper can be remedied by adding an additional flexure to the half-diamond flexure that would be compliant in the taper direction but stiff in the out-of-plane direction. This would reduce the parasitic errors and allow the actuation to be transmitted more efficiently in the out-of-plane direction. Furthermore, the design for the 6-axis will use three independently controlled half-diamond flexures that will be placed symmetrically about the central axis. The parasitic effect will be reduced if the flexures are assembled with the taper all pointed inward or outward from the central axis.

### 6.4.2 Dynamic Behavior

The dynamic testing was conducted by imparting an impulse to the nanopositioner and measuring its vibrational reaction. The metrology system was limited to 1 kHz sampling rate, which meant that resonance frequencies above 1 kHz, as predicted by the model, would not be detected. This is evident in the large peak at 1 kHz in the data that was fast Fourier transformed into the frequency domain as seen in Figure 6.10. The results show that the resonant frequency of the nanopositioner achieved the 1 kHz functional requirement.





# CHAPTER 7

## 7 Research Contributions and Future Work

This final chapter of the thesis summarizes what was accomplished in the research effort and its impact to other research fields. This chapter also describes what subsequent work is required to further advance the research.

### 7.1 Research Impact

The main reason for this research was a lack of instrumentation that could accomplish multiple modes of CNT testing, which was required to obtain the necessary data in a cost efficient manner. To address this issue, the research mapped out unfulfilled requirements for characterizing integrated CNT structures and developed a new system.

The research's core accomplishment was developing a suitable nanopositioner responsible for the precision motion of the new CNT testing system. Unlike existing nanopositioners, this nanopositioner offered a low cost, compact design that could be installed in the SEM with

minimal modifications to the SEM. The nature of its construction allowed further customized modifications that could suit the user's needs.

In terms of design, the adaptation of the HexFlex, a 6-axis compliant mechanism, to the SEM produced further insight into how to reduce the size of the overall system and actuate the mechanism with piezo-electric actuators. As a by-product, other compliant mechanism designs were also developed, such as the out-of-plane compliant transmission mechanism. The key components of the nanopositioner were tested in a 4-axis version that demonstrated the feasibility of the 6-axis design.

## **7.2 Future Work**

Due to the limited time window for conducting this research, future work is necessary to prepare the nanopositioner for integration with the overall CNT testing system.

First of all, the 6-axis design must be constructed according to the design presented in this work. This involves using the design methodology used to construct the 4-axis prototype and making the proper adjustments to add two additional axes of motion. Then, testing that was conducted on the 4-axis prototype must be conducted on the 6-axis nanopositioner.

After the bench top performance is verified for the 6-axis nanopositioner, it must be tested inside the SEM. To accomplish this, the leads to the actuators must be passed through the chamber wall using a chamber port with electrical leads that connect the inside to the outside. It is important to identify any degradation in SEM performance due to the nanopositioner.

Finally, a sensing system needs to be integrated into the positioner to offer position feedback. The position feedback would be used in a closed loop control algorithm to reduce hysteresis inherent in piezo-electric actuation and inaccuracies that deviate from linear approximations. In addition, the position feedback could also obtain information about the reaction forces involved in mechanical deformation of CNT test samples. One method for sensing position is by using the piezoresistive effect to track mechanical strains in the positioner. The motion of the positioner could be calculated from the measured strain, as well as the amount of force induced onto the positioner in the case of compliant flexures. Piezoresistive technology is already very well understood in the field of micro-sensors. Their relatively new application to the field of compliant mechanisms can be seen in the work done at BYU's Compliant Mechanisms Research Laboratory.

After these three future tasks are accomplished, the nanopositioner can be successfully integrated into the overall CNT testing system to gather multi-axis testing data necessary for building CNT-based compliant mechanisms.

# REFERENCES

1. Anderson, G., *A six-degree of freedom flexural positioning stage* MIT S.M. Thesis M.E., 2003.
2. Mamalis, A.G., L.O.G. Vogtlander, and A. Markopoulos, *Nanotechnology and nanostructured materials: trends in carbon nanotubes*. Precision Engineering, 2004. **28**(1): p. 16-30.
3. *Reprinted from Materials Science and Engineering: C, Vol 15, Cohen, M.L., Nanotubes, Nanoscience, and Nanotechnology, 1-11, Copyright (2001), with permission from Elsevier.*
4. *Reprinted with permission from Iijima, S., et al., Structural flexibility of carbon nanotubes. The Journal of Chemical Physics, 1996. 104(5): p. 2089-2092. Copyright 1996, American Institute of Physics.*
5. Dresselhaus, M.S. and P. Avouris, *Introduction to carbon Materials Research*. Topics in Applied Physics. 2001. 1.
6. Ruoff, R.S., D. Qian, and W.K. Liu, *Mechanical properties of carbon nanotubes: theoretical predictions and experimental measurements*. Comptes Rendus Physique, 2003. **4**(9): p. 993-1008.
7. Yakobson, B.I. and P. Avouris, *Mechanical Properties of Carbon Nanotubes*. Topics in Applied Physics. 2001. 287.
8. Iijima, S., et al., *Structural flexibility of carbon nanotubes*. The Journal of Chemical Physics, 1996. **104**(5): p. 2089-2092.
9. Yakobson, B.I., C.J. Brabec, and J. Bernholc, *Nanomechanics of Carbon Tubes: Instabilities beyond Linear Response*. Physical Review Letters, 1996. **76**(14): p. 2511-2514.
10. Falvo, M.R., et al., *Bending and buckling of carbon nanotubes under large strain*. Nature, 1997. **389**(6651): p. 582-584.
11. Yu, M.-F., et al., *Strength and Breaking Mechanism of Multiwalled Carbon Nanotubes Under Tensile Load*. Science, 2000. **287**(5453): p. 637-640.

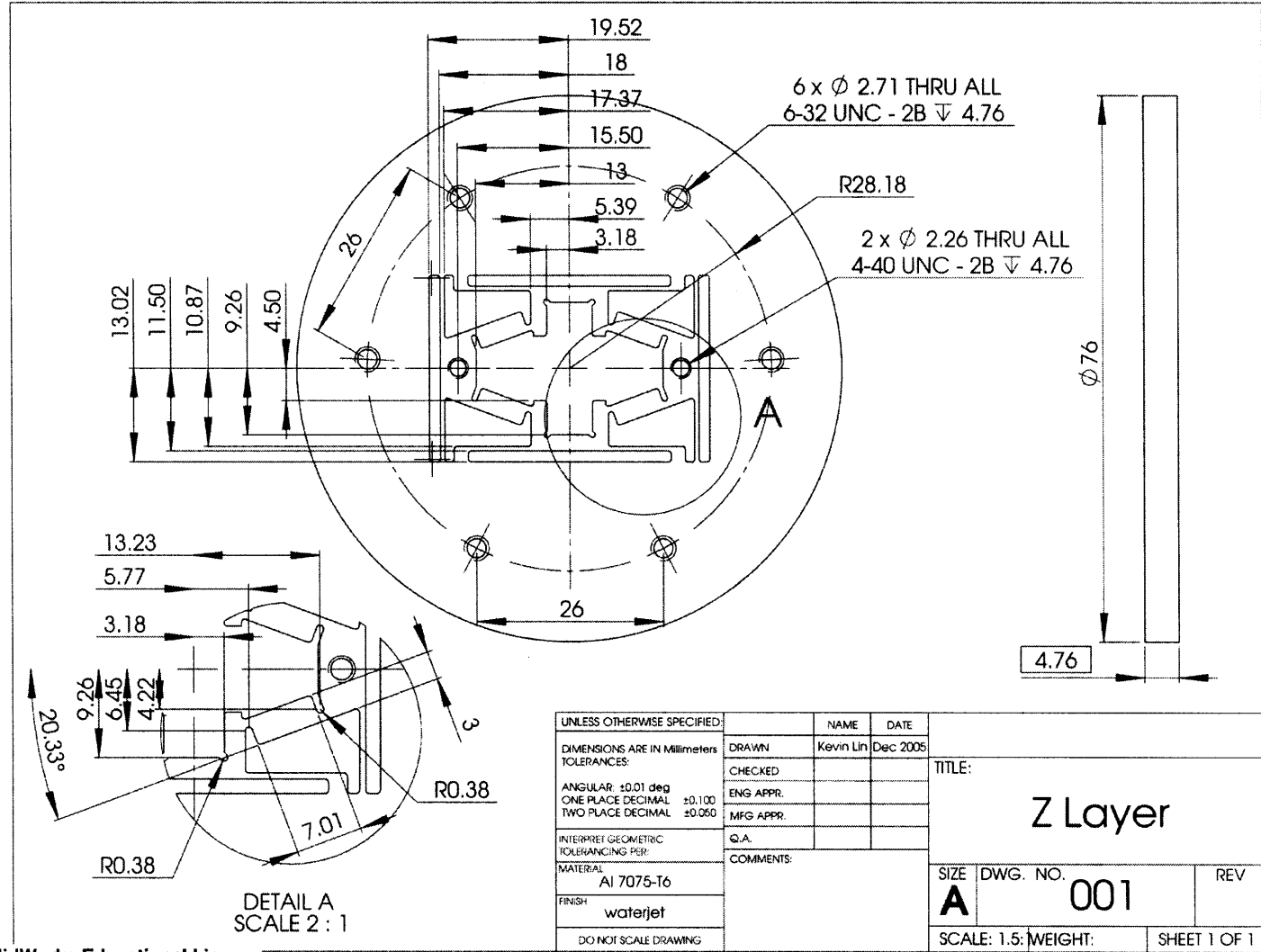
12. Mamedov, A.A., et al., *Molecular design of strong single-wall carbon nanotube/polyelectrolyte multilayer composites*. Nature Materials, 2002. **1**: p. 190-194.
13. Culpepper, M.L. and G. Anderson, *Design of a low-cost nano-manipulator which utilizes a monolithic, spatial compliant mechanism*. Precision Engineering, 2004. **28**(4): p. 469-482.
14. Howell, L.L., *Compliant Mechanisms*. 2001: John Wiley & Sons Inc. 495.
15. Dequesnes, M., S.V. Rotkin, and N.R. Aluru, *Calculation of pull-in voltages for carbon-nanotube-based nanoelectromechanical switches*. Nanotechnology, 2002(1): p. 120-131.
16. Saito, S., et al., *Kinematics of mechanical and adhesional micromanipulation under a scanning electron microscope*. Journal of Applied Physics, 2002. **92**(9): p. 5140-5149.
17. Yu, M., et al., *Three-dimensional manipulation of carbon nanotubes under a scanning electron microscope*. Nanotechnology, 1999(3): p. 244-252.
18. Dong, L., F. Arai, and T. Fukuda, *Destructive constructions of nanostructures with carbon nanotubes through nanorobotic manipulation*. Mechatronics, IEEE/ASME Transactions on, 2004. **9**(2): p. 350-357.
19. Dong, L., F. Arai, and T. Fukuda. *3D nanorobotic manipulations of multi-walled carbon nanotubes*. 2001.
20. Williams, P.A., et al., *Controlled placement of an individual carbon nanotube onto a microelectromechanical structure*. Applied Physics Letters, 2002. **80**(14): p. 2574-2576.
21. Hartman, A.B., et al. *Force-deflection characterization of individual carbon nanotubes attached to MEMS devices*. 2004.
22. Papadakis, S.J., et al., *Resonant Oscillators with Carbon-Nanotube Torsion Springs*. Physical Review Letters, 2004. **93**(14): p. 146101-4.
23. *Reprinted with permission from Williams, P.A., et al., Controlled placement of an individual carbon nanotube onto a microelectromechanical structure. Applied Physics Letters, 2002. 80(14): p. 2574-2576. Copyright 2002, American Institute of Physics.*
24. PI, <http://www.nanopositioners.com/>. Physik Instrumente Nanopositioner Product Catalog, 2005.
25. Wong, E.W., P.E. Sheehan, and C.M. Liebert, *Nanobeam mechanics: Elasticity, strength, and toughness of nanorods and nanotubes*. Science, 1997. **277**(5334): p. 1971-1975

26. Slocum, A., *Precision Machine Design*. 1992, Dearborn, Michigan: Society of Manufacturing Engineers.
27. Petri, P., *A Continuum Mechanics Aid for Non-planar Compliant Mechanisms*, in *Mechanical Engineering*. 2002, Massachusetts Institute of Technology: Cambridge.
28. Johnson, K.L., *Contact Mechanics*. 1985, Cambridge, UK: Cambridge University Press.

# Appendix A

The following are engineering drawings of main components for 4-axis nanopositioner and metrology stage.

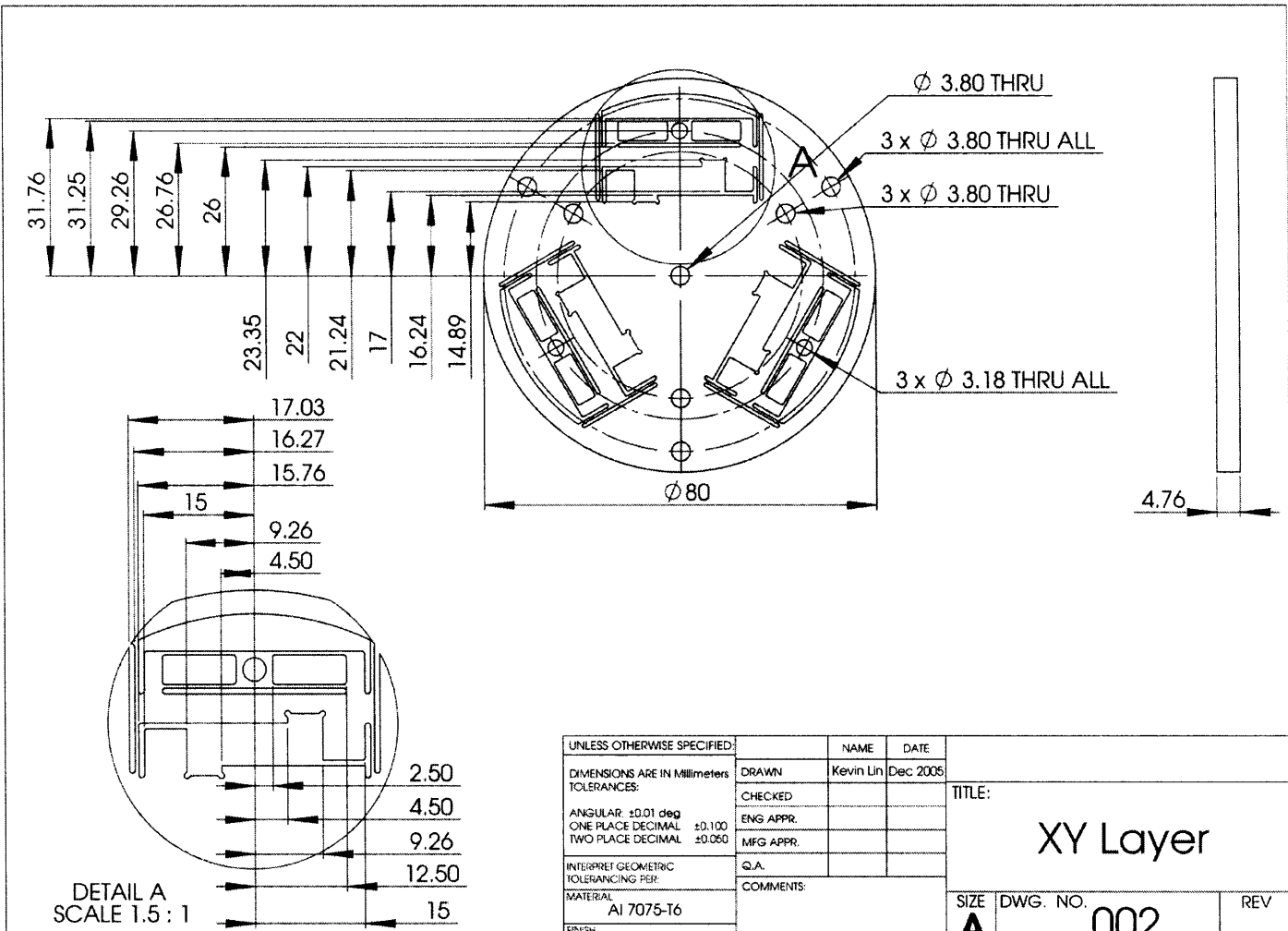
Figure A.1: Engineering drawing of out-of-plane motion component layer.



SolidWorks Educational License  
Instructional Use Only



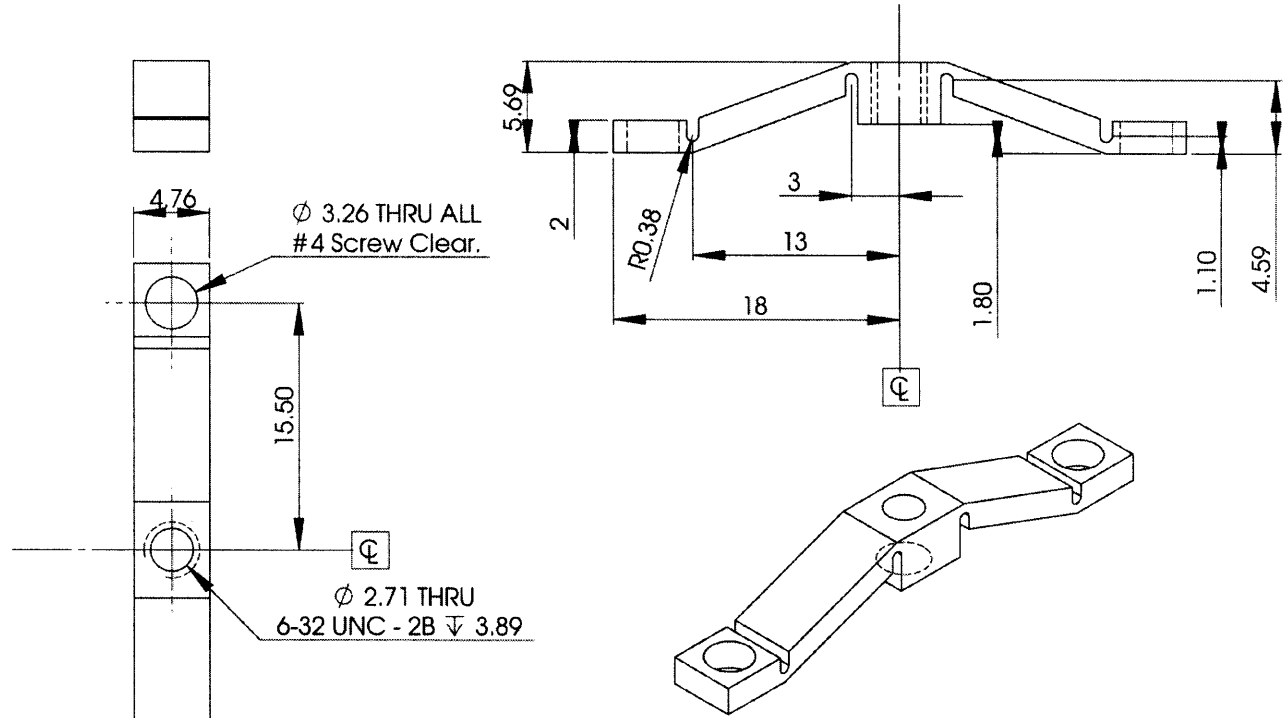
Figure A.2: Engineering drawing of in-plane component layer.



UNLESS OTHERWISE SPECIFIED:	NAME	DATE	
DIMENSIONS ARE IN Millimeters TOLERANCES:	DRAWN	Kevin Lin	Dec 2005
ANGULAR: ±0.01 deg	CHECKED		
ONE PLACE DECIMAL: ±0.100	ENG APPR.		
TWO PLACE DECIMAL: ±0.050	MFG APPR.		
INTERPRET GEOMETRIC TOLERANCING PER:	Q.A.		
MATERIAL	COMMENTS:		
Al 7075-T6			
FINISH		SIZE	DWG. NO.
waterjet		A	002
DO NOT SCALE DRAWING		REV	
		SCALE: 1:1	WEIGHT: SHEET 1 OF 1

SolidWorks Educational License  
Instructional Use Only

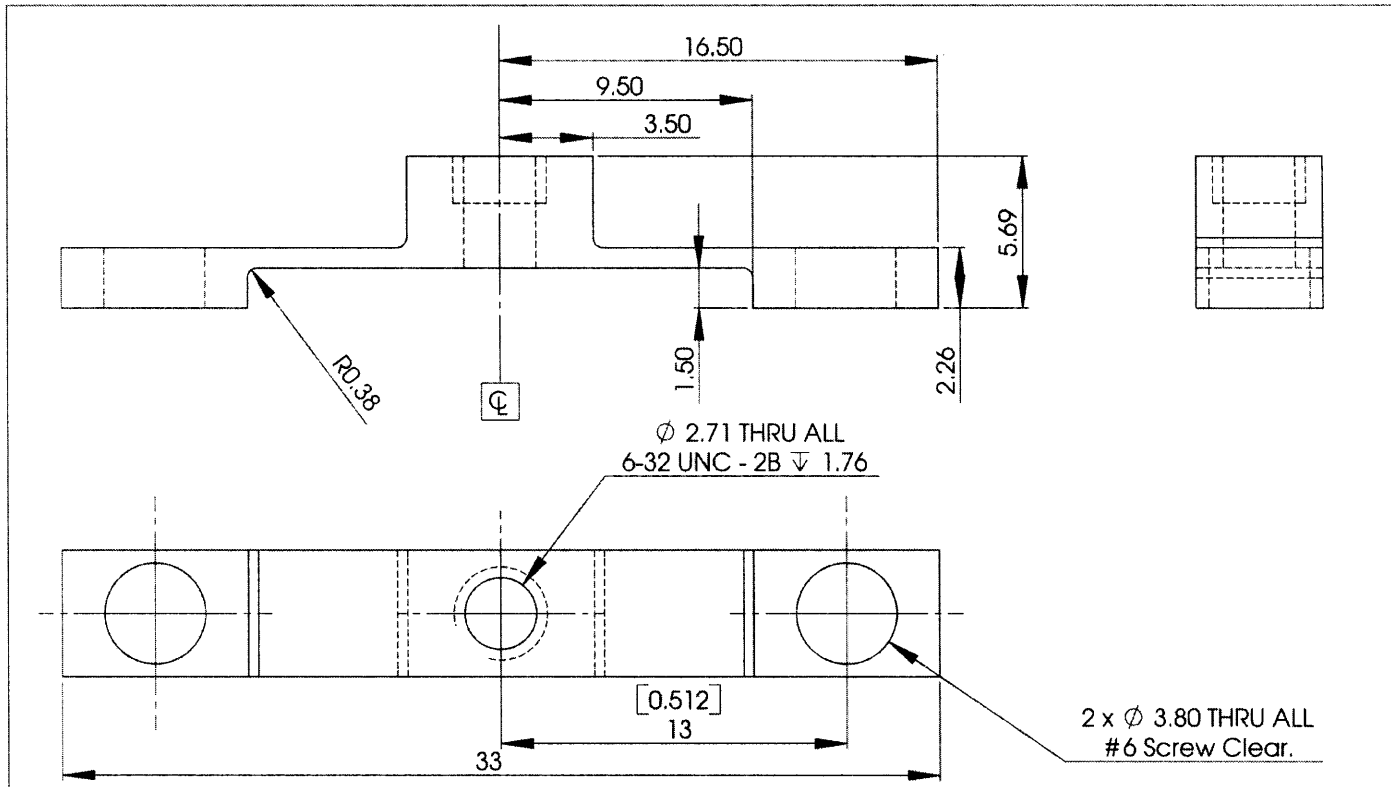
Figure A.3: Engineering drawing of half-diamond flexure used for out-of-plane motion.



UNLESS OTHERWISE SPECIFIED:	NAME	DATE	TITLE:	
DIMENSIONS ARE IN Millimeters	DRAWN	Kevin Lin	Dec 2005	Half-Diamond Flexure
TOLERANCES:	CHECKED			
ANGULAR: ±0.01 deg	ENG APPR.			
ONE PLACE DECIMAL ±0.100	MFG APPR.			
TWO PLACE DECIMAL ±0.050	Q.A.			SIZE DWG. NO. REV
INTERPRET GEOMETRIC TOLERANCING PER:	COMMENTS:			<b>A</b> 003
MATERIAL				SCALE: 3:1 WEIGHT: SHEET 1 OF 1
AI 7075-T6				
FINISH				
waterjet				
DO NOT SCALE DRAWING				

SolidWorks Educational License  
Instructional Use Only

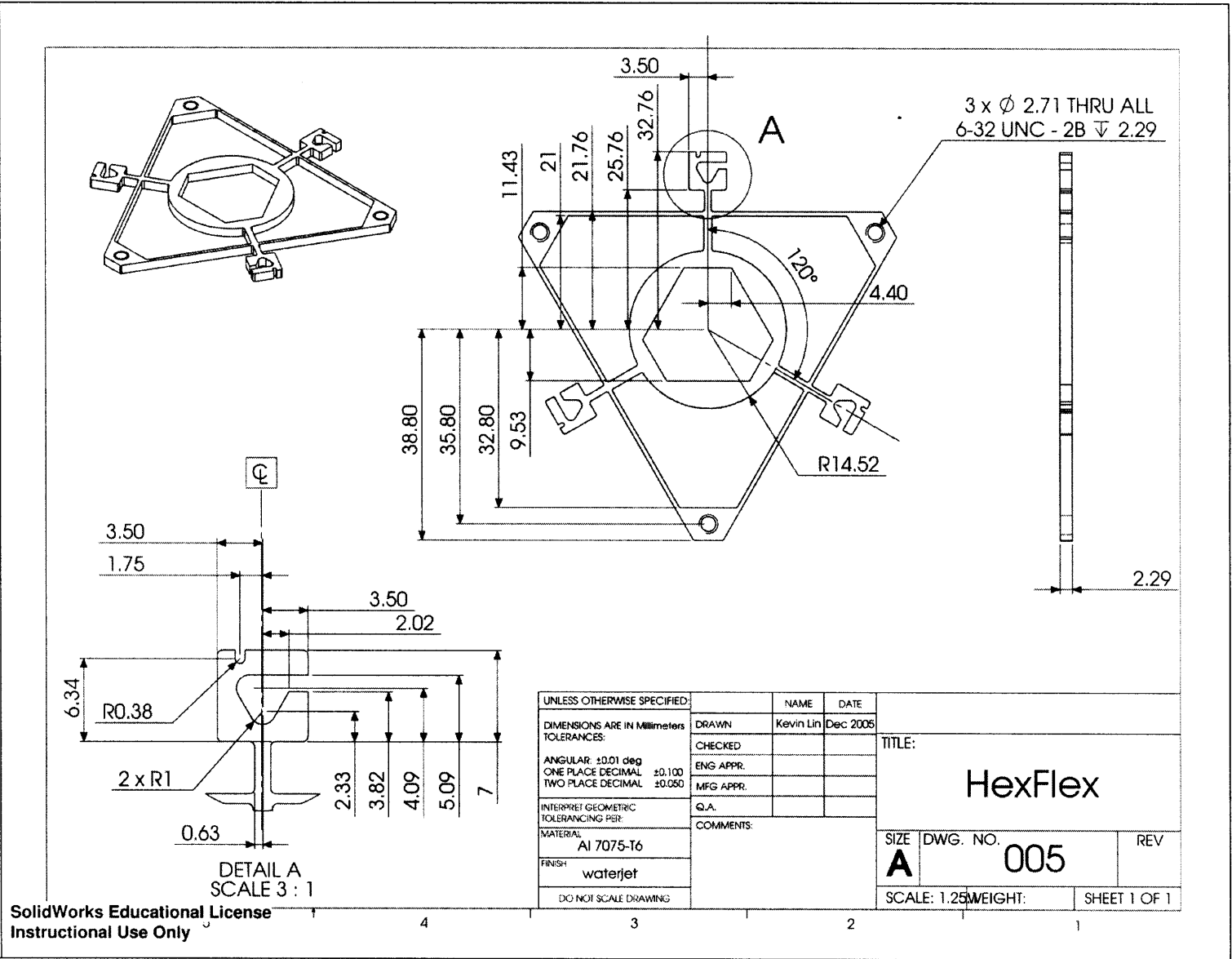
Figure A.4. Engineering drawing of support flexures for guiding out-of-plane motion.



UNLESS OTHERWISE SPECIFIED:	NAME	DATE	TITLE:	
DIMENSIONS ARE IN Millimeters	DRAWN	Kevin Lin	Dec 2008	Support Flexures
TOLERANCES:	CHECKED			
ANGULAR: $\pm 0.01$ deg	ENG APPR.			
ONE PLACE DECIMAL $\pm 0.100$	MFG APPR.			
TWO PLACE DECIMAL $\pm 0.050$	Q.A.			SIZE
INTERPRET GEOMETRIC TOLERANCING PER:	COMMENTS:			DWG. NO.
MATERIAL				004
AI 7075-T6				REV
FINISH				
waterjet				
DO NOT SCALE DRAWING				SCALE: 5:1
				WEIGHT:
				SHEET 1 OF 1

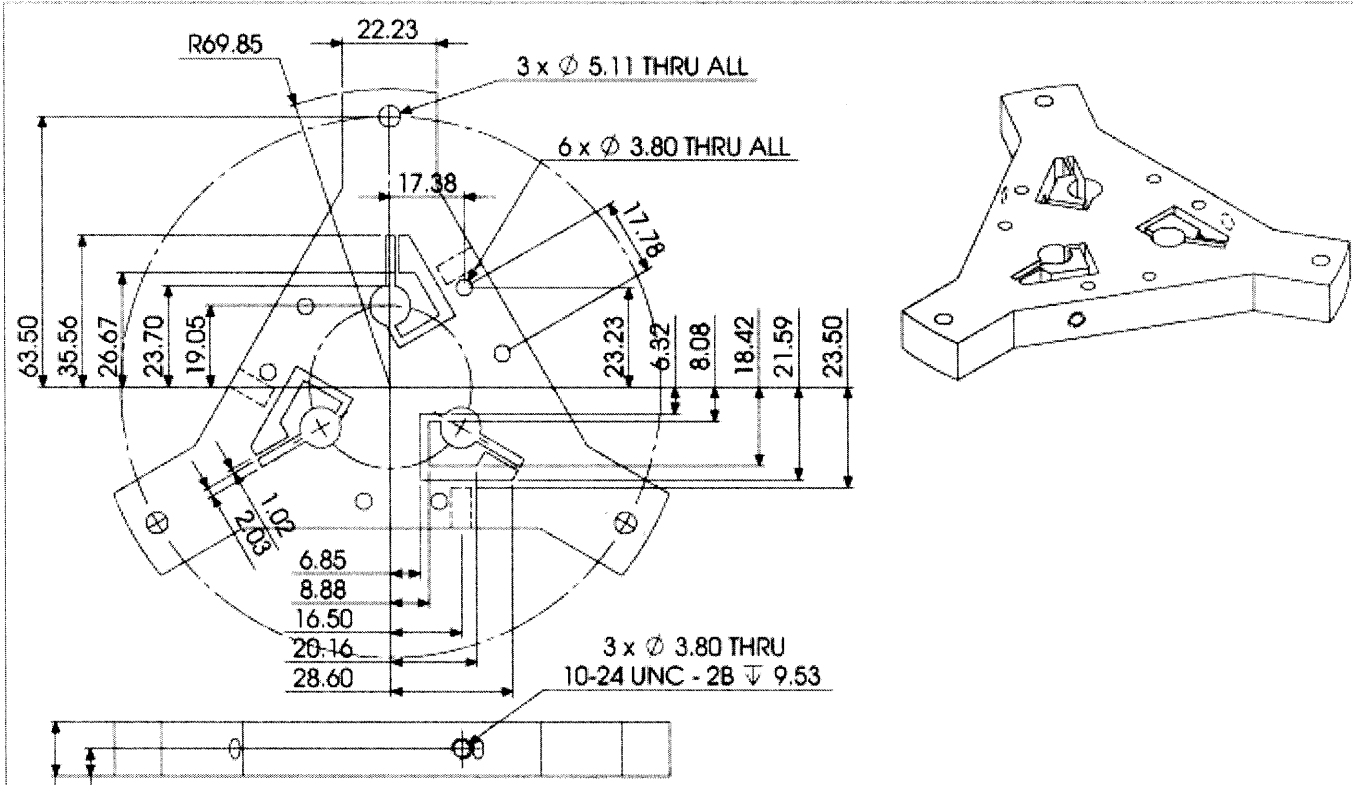
SolidWorks Educational License  
Instructional Use Only

Figure A.5: Engineering drawing for HexFlex device that was adapted for the nanopositioner.



SolidWorks Educational License  
Instructional Use Only

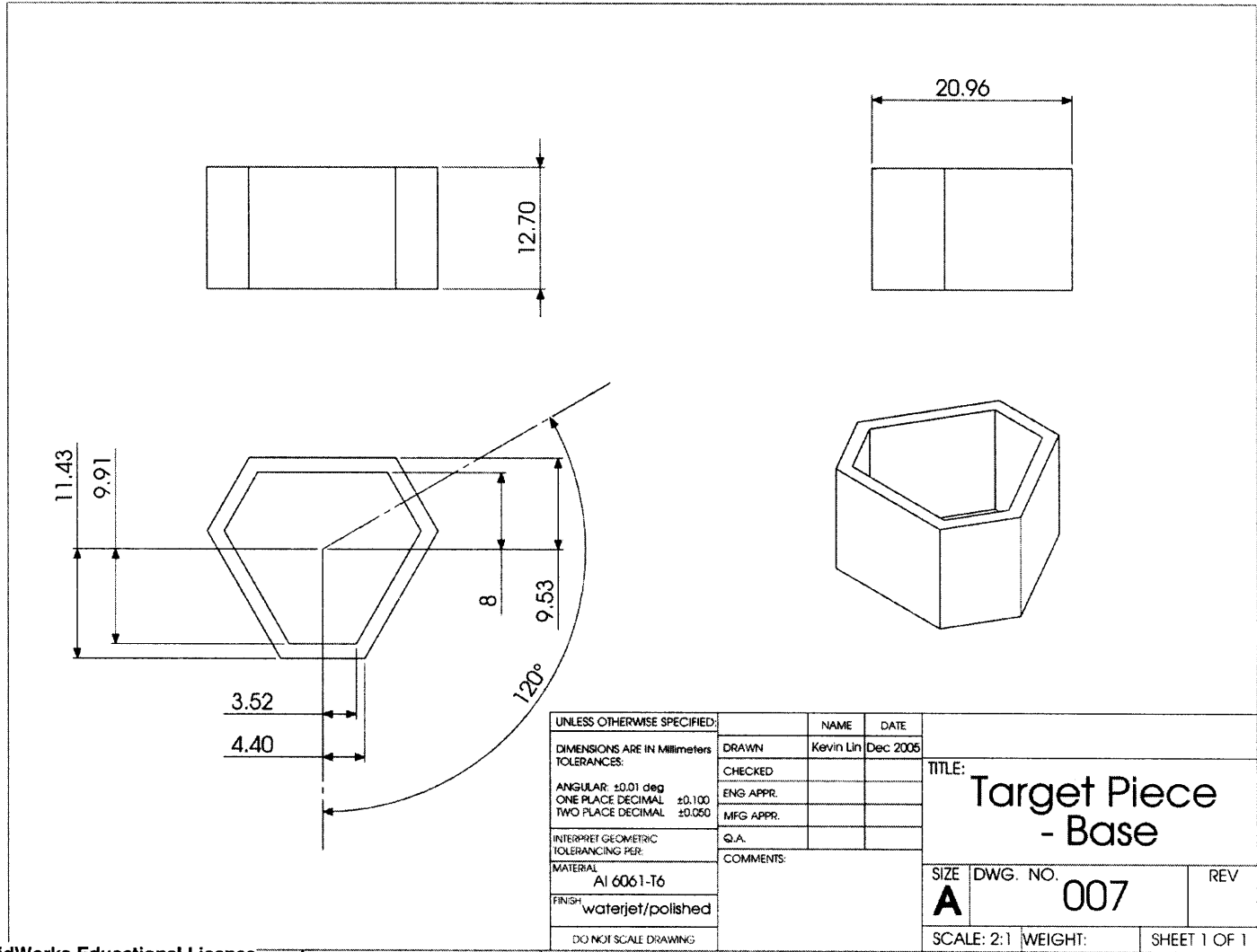
Figure A.6: Engineering drawing of main metrology stage component.



UNLESS OTHERWISE SPECIFIED:	NAME	DATE	TITLE:	
DIMENSIONS ARE IN MILLIMETERS	DRAWN	Kevin Lin	Dec 2006	<b>Metrology Main Plate</b>
TOLERANCES	CHECKED			
ANGULAR: ±0.01 deg	ENG APPR			
ONE PLACE DECIMAL ±0.100	MFG APPR			SIZE DWG. NO. <b>A 006</b> REV
TWO PLACE DECIMAL ±0.050	Q.A.			SCALE: 1:1 WEIGHT: SHEET 1 OF 1
INTERPRET GEOMETRIC TOLERANCING PER	COMMENTS			
MATERIAL:				
Al 6061-T6				
FINISH:				
waterjet				
DO NOT SCALE DRAWING				

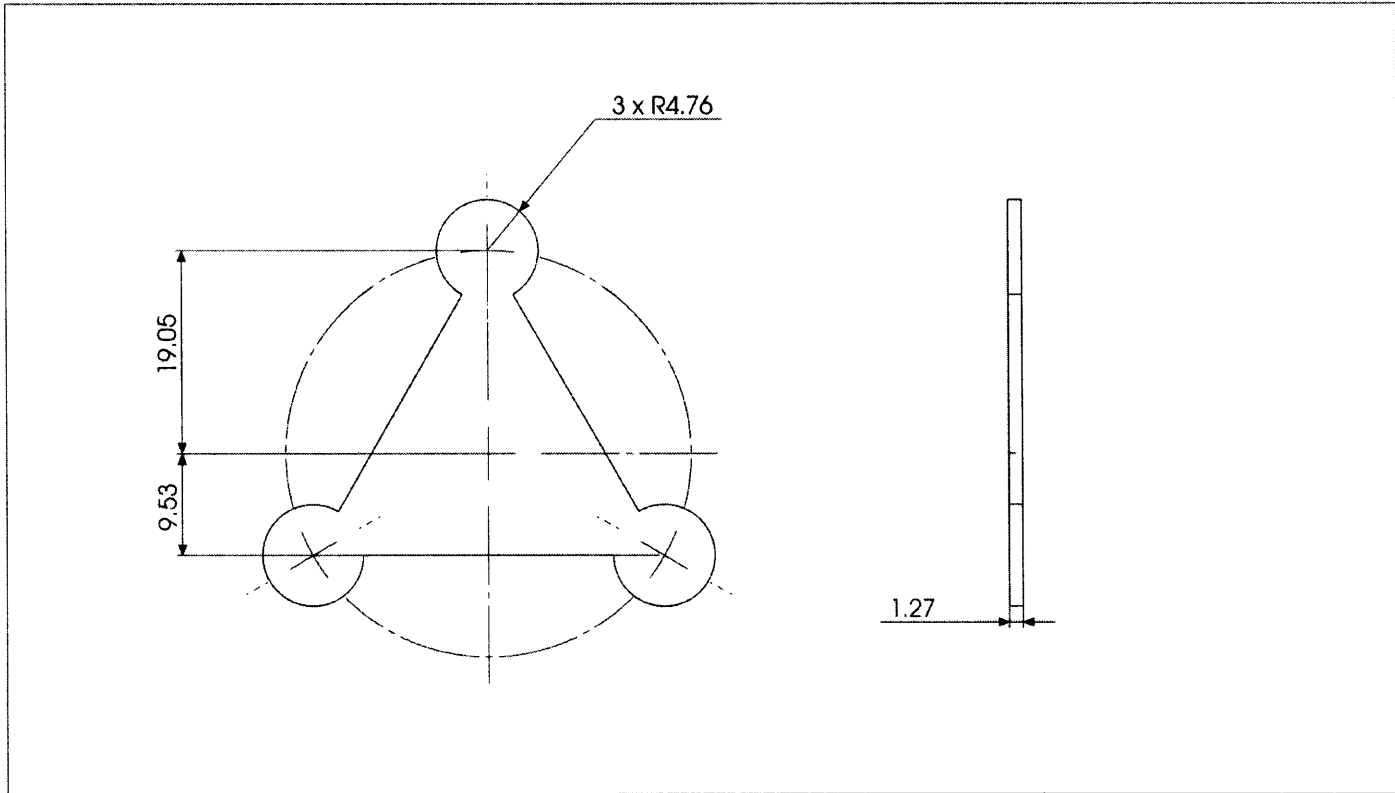
SolidWorks Educational License  
Instructional Use Only

Figure A.7: Engineering drawing of bottom component of target piece.



SolidWorks Educational License  
Instructional Use Only

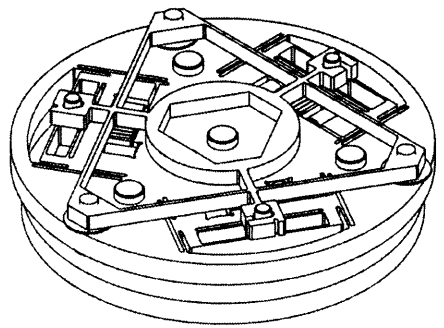
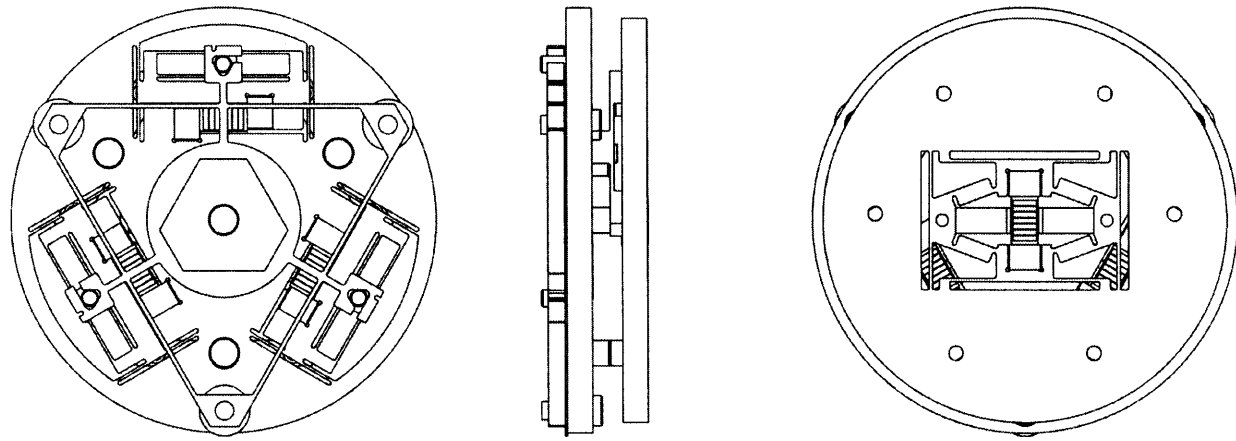
Figure A.8: Engineering drawing of top component of target piece.



UNLESS OTHERWISE SPECIFIED:	NAME	DATE	TITLE:	
DIMENSIONS ARE IN Millimeters	DRAWN	Kevin Lin	Dec 2005	Target Piece - Top
TOLERANCES:	CHECKED			
ANGULAR: ±0.01 deg	ENG APPR.			SIZE
ONE PLACE DECIMAL: ±0.100	MFG APPR.			DWG. NO.
TWO PLACE DECIMAL: ±0.050	Q.A.			008
INTERPRET GEOMETRIC TOLERANCING PER:	COMMENTS:			REV
MATERIAL				
Al 6061-T6				
FINISH				
polished				
DO NOT SCALE DRAWING				
	SCALE: 2:1	WEIGHT:	SHEET 1 OF 1	

SolidWorks Educational License  
Instructional Use Only

Figure A.9: Engineering drawing of assembled nanopositioner.



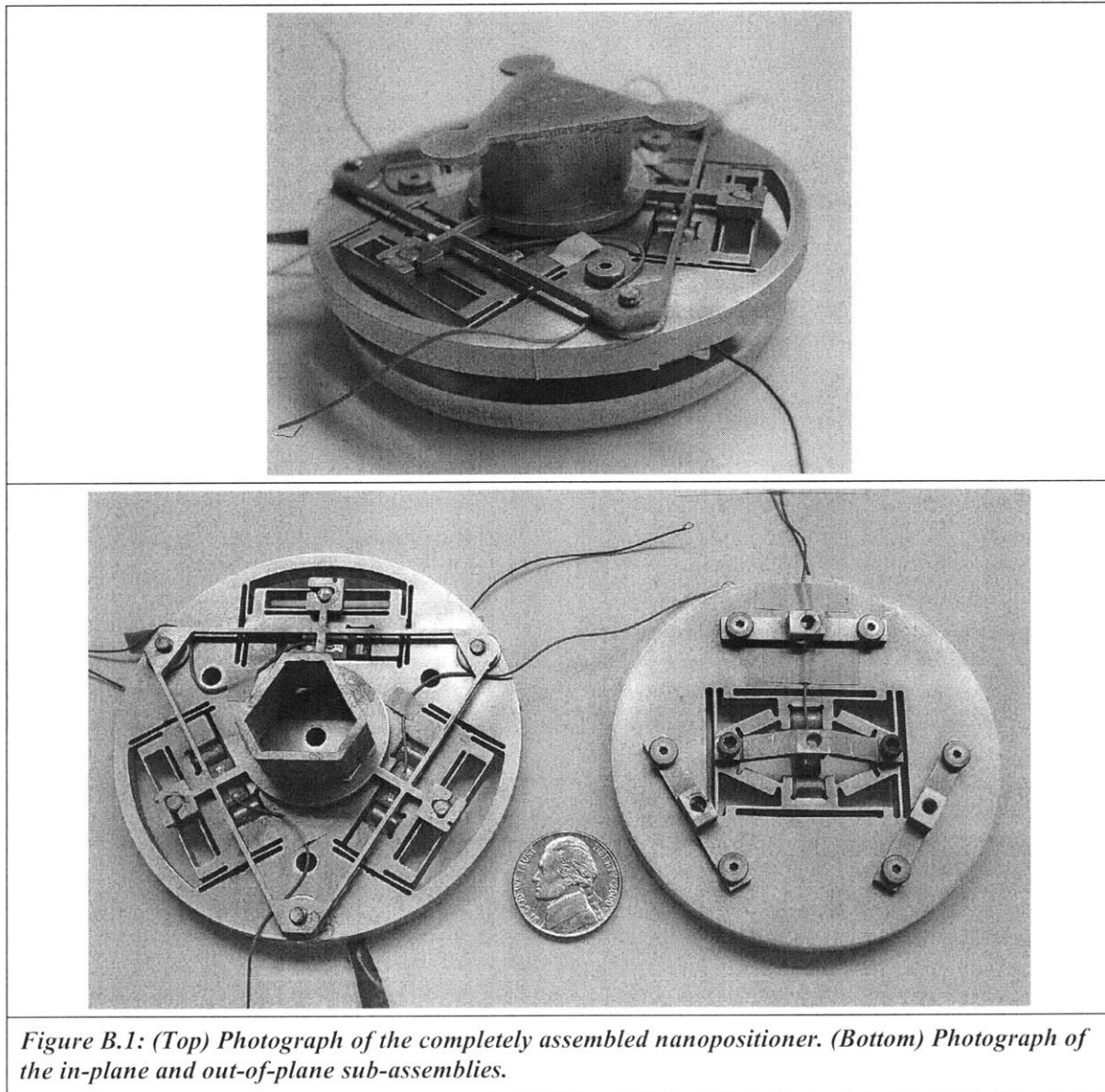
UNLESS OTHERWISE SPECIFIED:	NAME	DATE		
DIMENSIONS ARE IN Millimeters	DRAWN	Kevin Lin	Dec	2005
TOLERANCES:	CHECKED		TITLE:	
ANGULAR: ±0.01 deg	ENG APPR.		Assembled	
ONE PLACE DECIMAL: ±0.100	MFG APPR.		Nanopositioner	
TWO PLACE DECIMAL: ±0.050	Q.A.		SIZE	DWG. NO.
INTERPRET GEOMETRIC TOLERANCING PER:	COMMENTS:		<b>A</b>	009
MATERIAL:				REV
Al 7075-T6				
FINISH:			SCALE: 1:1	WEIGHT:
waterjet				SHEET 1 OF 1
DO NOT SCALE DRAWING				

SolidWorks Educational License  
Instructional Use Only



# Appendix B

The following are photographs of the 4-axis nanopositioner.



*This page is intentionally left blank.*

# Appendix C

The following is Matlab Code that was used for calculating the error budget for the overall system.

**Main script that sets the system parameters and calls on other functions to calculate and plot the error budget due to the input errors.**

```
% Main Error Budget Script
% 1. Sets up system geometry
% 2. Generates random error values
%     a. Thermo (Guassian of Temp flux)
%     b. Assembly Errors (Guassian of relative placement of
components)
%     c. Fabrication Errors (Guassian of fabrication tolerances
like
%         straightness)
% 3. Determine new Geom with error
% 4. Construct new HTM
% 5. Run simulation over several trials
% 6. Plot results to see envelope

% Sets the ideal geometry of system
% Uses only critical dimensions between CSs

% Stage Dimensions
L_wall_left = .200;      % Distance to left chamber wall from E-beam
H_stage_anchor = .0208; % Distance to stage anchor from E-beam
L_stage_mount = .1995;  % Length of stage from cham. wall to cantilvr
load
H_stage_mount = .107;   % Distance from anchor to cantilever load
% Translation Stage Dimensions
H_trans_stage = .085;   % Height from cantilever load to top of stage
% Carriage Dimensions
H_carriage = .0015;     % Height of carriage base
% Positioner Dimensions
H_pos_base = .005;      % Height of positioner base
```

```

H_pos_top = .013;          % Height of positioner top component
% End-effector Dimensions
L_end_effector = .0005; % Length of end effector
H_end_effector = .001;  % Height of end effector

% Sample Stage Dimensions
L_wall_right = .143;     % Distance to right chamber wall from E-beam
H_sample_anchor = .026; % Height from E-beam to sample anchor
L_sample_mount = .1365; % Length to sample cantilever
H_sample_mount = .049;  % Height from sample anchor point to sample
cantilever
L_sample = .0065;       % Length of sample
H_sample = .0007;      % Height of sample

% Map out ideal (base) geometry
[Geom] = ideal_geom(L_wall_left,H_stage_anchor,L_stage_mount, ...
    H_stage_mount,H_trans_stage,H_carriage, H_pos_base,...
    H_pos_top, L_end_effector, H_end_effector, L_wall_right, ...
    H_sample_anchor, L_sample_mount, H_sample_mount,...
    L_sample, H_sample);

% Generate random error values
% Set number of trials
trials = 100;

% TEMP: Set gaussian conditions
T_mean = 22; % room temperature
T_sigma = .5; % + 0.5 C
alpha_Al = 23.6e-6; % 7075-T6 Al
alpha_Stl = 17.3e-6; % 304 Stainless Steel
% Call ERROR_THERMO4 function
[err_therm_Al,err_therm_Stl] = error_thermo(alpha_Al,alpha_Stl,...
    T_mean,T_sigma,trials);

% Fabrication Tolerances Errors: set gaussian conditions
Fab_error_mean = 0; % +/- machining tolerance
Fab_error_3sigma = 7.62e-5; % +/- .003" on surface
straightness/dimensions
% from waterjet

% Call ERROR_FAB function
[err_fab_L,err_fab_index] =
error_fab(Fab_error_mean,Fab_error_3sigma,trials);

% Assembly Errors: set gaussian conditions
% +/- .01" milling (CNC) tolerance x,y
Assem_error_carriage_3sigma = 2.54e-4;
% +/- .01" waterjet/clearance tolerance in x,y,z
Assem_error_pos_anchor_3sigma = 2.54e-4;
% +/- .01" waterjet/clearance tolerance in x,y,z
Assem_error_pos_top_3sigma = 2.54e-4;

```

```

% % TEMP: Set gaussian conditions
% T_mean = 22; % room temperature
% T_sigma = 0; % +/- 0.5 C
% alpha_Al = 23.6e-6; % 7075-T6 Al
% alpha_Stl = 17.3e-6; % 304 Stainless Steel
% % Call ERROR_THERMO4 function
% [err_therm_Al,err_therm_Stl] =
error_thermo(alpha_Al,alpha_Stl,T_mean,T_sigma,trials);
%
% % Fabrication Tolerances Errors: set gaussian conditions
% Fab_error_mean = 0; % +/- machining tolerance
% Fab_error_3sigma = 0; % +/- .003" on surface
straightness/dimensions from waterjet
% % Call ERROR_FAB function
% [err_fab_L,err_fab_index] =
error_fab(Fab_error_mean,Fab_error_3sigma,trials);

% % Assembly Errors: set gaussian conditions
% Assem_error_carriage_3sigma = 0; % +/- .001" milling (CNC)
tolerance x,y
% Assem_error_pos_anchor_3sigma = 0; % +/- .003" waterjet tolerance
in x,y,Z
% Assem_error_pos_top_3sigma = 0; % +/- .003" waterjet tolerance in
x,y,z

% Call ERROR_ASSEM function
[Assem_err_carriage,Assem_err_pos_anchor,Assem_err_pos_top,err_assem_
index]...
= error_assem(...
Assem_error_carriage_3sigma,Assem_error_pos_anchor_3sigma,...
Assem_error_pos_top_3sigma,trials);

Err_vector_Array = []; % array that collects error vectors from
different trials
for i = 1:trials;
% Call THERMO_BUDGET function
[thermo] = thermo_budget(err_therm_Al(i),err_therm_Stl(i),...
L_wall_left,H_stage_anchor,L_stage_mount,H_stage_mount,...
H_trans_stage,H_carriage, H_pos_base,...
H_pos_top, L_end_effector, H_end_effector, L_wall_right,...
H_sample_anchor, L_sample_mount, H_sample_mount,...
L_sample, H_sample);

% Call FAB_BUDGET function
[fab] =
fab_budget(err_fab_L,trials,L_wall_left,H_stage_anchor,...
L_stage_mount,H_stage_mount,H_trans_stage,H_carriage,
H_pos_base,...
H_pos_top, L_end_effector, H_end_effector, L_wall_right, ...
H_sample_anchor, L sample mount, H sample mount,...

```

```

        L_sample, H_sample);

    % Call ASSEM_BUDGET function
    [assem] =
assem_budget(Assem_err_carriage,Assem_err_pos_anchor,...
            Assem_err_pos_top, trials, L_wall_left,H_stage_anchor,...
            L_stage_mount,H_stage_mount,H_trans_stage,H_carriage,
H_pos_base,...
            H_pos_top, L_end_effector, H_end_effector, L_wall_right, ...
            H_sample_anchor, L_sample_mount, H_sample_mount,...
            L_sample, H_sample);

    % create New CS Geometry
    [new_Geom] = new_geom(Geom,thermo,fab,assem);

    % Make HTMs using new CS Geometry and determine the end-effector
to
    % sample vector
    % Call ERROR_VECTOR function
    [err_vector] = error_vector(new_Geom);

    % Collect all the err_vectors
    Err_vector_Array(:,i) = err_vector;
end

% Plot the error vectors in different along different axes
figure
axes('FontSize',12)
plot([1:trials],Err_vector_Array(1,:), 'r+-',[1:trials],...
     Err_vector_Array(2,:), 'bo--
', [1:trials],Err_vector_Array(3,:), 'gx-.');
title('Error Vector Components vs. Simulation Trial','FontSize',16)
xlabel('Simulation Trial Number','FontSize',14)
ylabel('Translation Error (m)','FontSize',14)
legend('x','y','z','FontSize',14)
grid on

% Finding the corresponding rotational angles to align CNTs
% Not concerned with theta_x, because course motion in theta x

theta_z = atan(Err_vector_Array(2,:)./Err_vector_Array(1,:));
del_xp = Err_vector_Array(1,:)./cos(theta_z);
theta_y = atan(Err_vector_Array(3,:)./del_xp);
theta_x = zeros(1,trials);

% Plot Rotation Angles (Degrees) vs. Trial Number
figure
axes('FontSize',12)
plot(1:trials,theta_x, 'r+-',1:trials,theta_y*180/pi, 'bo--',...
     1:trials,theta_z*180/pi, 'gx-.')
title('Rotational Angles for CNT Alignment of CNTh to

```

```

CNTi','FontSize',16)
xlabel('Simulation Trial Number','FontSize',14)
ylabel('Rotation Angles (deg)','FontSize',14)
grid on
legend \thetax \thetay \thetaz

```

**Function that sets up the translational and rotational relationship between coordinate systems.**

```

function [Geom] =
ideal_geom(L_wall_left,H_stage_anchor,L_stage_mount,...
    H_stage_mount,H_trans_stage,H_carriage, H_pos_base, H_pos_top,...
    L_end_effector, H_end_effector, L_wall_right, H_sample_anchor,
    ...
    L_sample_mount, H_sample_mount, L_sample, H_sample)

% Setup the Geometry relating one CS to another

Geom.stage.anchor.delta = [-L_wall_left,0,-H_stage_anchor]';
Geom.stage.anchor.theta = [0 0 0]';

Geom.stage.mount.delta = [L_stage_mount,0,-H_stage_mount]';
Geom.stage.mount.theta = [0 0 0]';

Geom.stage.trans.delta = [0 0 H_trans_stage]';
Geom.stage.trans.theta = [0 0 0]';

Geom.carriage.delta = [0 0 H_carriage]';
Geom.carriage.theta = [0 0 0]';

Geom.positioner.anchor.delta = [0 0 H_pos_base]';
Geom.positioner.anchor.theta = [0 0 0]';

Geom.positioner.top.delta = [0 0 H_pos_top+H_end_effector]';
Geom.positioner.top.theta = [0 0 0]';

Geom.endeffect.delta = [L_end_effector 0 0]';
Geom.endeffect.theta = [0 0 0]';

Geom.sample.anchor.delta = [L_wall_right,0,H_sample_anchor]';
Geom.sample.anchor.theta = [0 0 pi]';

Geom.sample.mount.delta = [L_sample_mount,0,-H_sample_mount]';
Geom.sample.mount.theta = [0 0 0]';

Geom.sample.delta = [L_sample 0 H_sample]';
Geom.sample.theta = [0 0 0]';

```

**Function that constructs the forward and inverse HTM.**

```
function [H_BtoA,H_AtoB] = HTM(Theta,Delta)

% Makes the foward and inverse HomoGeneous Transformation Matrices
% for CS A and CS B
%           [H_AtoB,H_BtoA] = HTM(Theta,Delta)
%
% Input: "Theta" = Column Vector of Thetas from CS A to CS B
(O_x,O_y,O_z)'
%       "Delta" = Column Vector of Displacements from CS A to CS B
%       (del_x,del_y,del_z)
% Output: "H_AtoB" = HTM to map CS B vector in CS A
%         "H_BtoA" = HTM to map CS A vector in CS B

% Define variables
O_x = Theta(1);
O_y = Theta(2);
O_z = Theta(3);
% Rotational Matrices
Rx = [1 0 0; 0 cos(O_x) -sin(O_x); 0 sin(O_x) cos(O_x)];
Ry = [cos(O_y) 0 sin(O_y); 0 1 0; -sin(O_y) 0 cos(O_y)];
Rz = [cos(O_z) -sin(O_z) 0; sin(O_z) cos(O_z) 0; 0 0 1];

% Trans Matrix from CS B to CS A
R_BtoA = Rz*Ry*Rx;      % Rotational Matrix
H_BtoA = [R_BtoA,Delta; [0 0 0 1]];
% Trans Matrix from Centroid to CS1, H_Ctocs1
R_AtoB = Rx'*Ry'*Rz';  % Rotational Matrix
del_AtoB = R_AtoB*Delta; % new displacement in CS1 CS
H_AtoB = [R_AtoB,-del_AtoB; [0 0 0 1]];
```

**Function that generates the distribution of thermal errors according to given parameters.**

```
function [err_therm_Al,err_therm_Stl] = error_thermo4(alpha_Al,...
alpha_Stl,T_mean,T_sigma,trials)

% Function that calculates the thermal error associated with each CS.
% Errors are estimated using Gaussian distribution.
% %%% Assume thermal error is same throughout the structure %%%
% Input: alpha_stage = coef. of expansion of Al
%        alpha_cndl = coef. of expansion of Stainless Steel
%        T_mean = mean Temp. during operation
%        T_sigma = stardard deviation of Temp
%        trials = # of elements in the distribution
% Output: err_therm_Al = thermal error [m/m]
%         err_therm_Stl = thermal error [m/m]
%%%%%%%%%%%%%%%%%%%%%%%%%%%%%%%%%%%%%%%%%%%%%%%%%%%%%%%%%%%%%%%%%%%%%%%%
%
```



```

% Estimate thermal errors (assume uniform expansion)
Temp = normrnd(T_mean,T_sigma,[1 trials]);
err_therm_Al = (Temp - T_mean)*alpha_Al; % growth of Al
err_therm_Stl = (Temp - T_mean)*alpha_Stl; % growth of Stl

```

**Function that generates the distribution of fabrication errors.**

```

function [err_fab_L,err_fab_index] = error_fab(Fab_error_mean,...
    Fab_error_3sigma, trials)

% Function that caculates the fabrication error associated with each
CS.
% Errors are estimated using Gaussian distribution in accordance with
stock
% material and machining tolerances.
% Input: Fab_error_mean = mean tolerance value
%       Fab_error_3sigma = first standard deviation for tolerance
% Output: err_fab_L = gaussian distribution of fabrication error
%         err_fab_index = array of random trial number to index for
%                         different component dimensions
%%%%%%%%%%%%%%%%%%%%%%%%%%%%%%%%%%%%%%%%%%%%%%%%%%%%%%%%%%%%%%%%%%%%%%%%
%%%%%%%%

% Estimate fabrication errors
err_fab_L = normrnd(Fab_error_mean,Fab_error_3sigma/3,[1 trials]);

% Generate random trial number index
err_fab_index = round(rand(1, trials)*( trials-1))+1;

```

**Function that generates the distribution of assembly errors.**

```

function
[Assem_err_carriage,Assem_err_pos_anchor,Assem_err_pos_top,...
    err_assem_index] = error_assem(Assem_error_carriage_3sigma,...
    Assem_error_pos_anchor_3sigma,Assem_error_pos_top_3sigma, trials)

% Function that generates the assembly errors given the assembly
% tolerances. Assume that the mean is Zero for the errors.
% Input: Assem_error_carriage_3sigma = errors associated with
carriage
%
%           attachment to the SEM stage.
%       Assem_error_pos_anchor_3sigma = errors associated with
mounting
%
%           the positioner to the
carriage.
%       Assem_error_pos_top_3sigma = errors associated with
assembling the

```

```

%                               top layer of positioner to base
layer
% Ouput: Randomly generate errors according to different tolerances

% Estimate carriage assembly errors
Assem_err_carriage = normrnd(0,Assem_error_carriage_3sigma/3,[1
trials]);
% Estimate positioner anchor layer assembly errors
Assem_err_pos_anchor = normrnd(0,Assem_error_pos_anchor_3sigma/3,[1
trials]);
% Estimate positioner anchor layer assembly errors
Assem_err_pos_top = normrnd(0,Assem_error_pos_top_3sigma/3,[1
trials]);

% Generate random trial number index
err_assem_index = round(rand(1,trials)*(trials-1))+1;

```

**Function that adjusts the relationship between coordinate systems according to the thermal errors.**

```

function [Thermo] = thermo_budget(err_therm_A1,err_therm_St1,...
    L_wall_left,H_stage_anchor,L_stage_mount,H_stage_mount,...
    H_trans_stage, H_carriage, H_pos_base, H_pos_top, L_end_effector,
    H_end_effector, L_wall_right, H_sample_anchor, L_sample_mount,
    H_sample_mount,L_sample, H_sample);

% Calculate the dimensional changes due to thermal expansion
% Apply thermal expansion on critical dimensions of the device

Thermo.stage.anchor.delta = [-L_wall_left,0,-
H_stage_anchor]'.*err_therm_St1;
Thermo.stage.anchor.theta = [0 0 0]';

Thermo.stage.mount.delta = [L_stage_mount,0,-
H_stage_mount]'.*err_therm_St1;
Thermo.stage.mount.theta = [0 0 0]';

Thermo.stage.trans.delta = [0 0 H_trans_stage]'.*err_therm_St1;
Thermo.stage.trans.theta = [0 0 0]';

Thermo.carriage.delta = [0 0 H_carriage]'.*err_therm_A1;
Thermo.carriage.theta = [0 0 0]';

Thermo.positioner.anchor.delta = [0 0 H_pos_base]'.*err_therm_A1;
Thermo.positioner.anchor.theta = [0 0 0]';

Thermo.positioner.top.delta = [0 0 H_pos_top]'.*err_therm_A1;
Thermo.positioner.top.theta = [0 0 0]';

```

```

Thermo.endeffect.delta = [L_end_effector 0
H_end_effector]'.*err_therm_St1;
Thermo.endeffect.theta = [0 0 0]';

Thermo.sample.anchor.delta =
[L_wall_right,0,H_sample_anchor]'.*err_therm_St1;
Thermo.sample.anchor.theta = [0 0 0]';

Thermo.sample.mount.delta = [L_sample_mount,0,-
H_sample_mount]'.*err_therm_A1;
Thermo.sample.mount.theta = [0 0 0]';

Thermo.sample.delta = [L_sample 0 H_sample]'.*err_therm_St1;
Thermo.sample.theta = [0 0 0]';

```

**Function that adjusts the relationship between coordinate systems according to the fabrication errors.**

```

function [fab] =
fab_budget(err_fab_L, trials, L_wall_left, H_stage_anchor, ...
    L_stage_mount, H_stage_mount, H_trans_stage, H_carriage,
H_pos_base, ...
    H_pos_top, L_end_effector, H_end_effector, L_wall_right, ...
    H_sample_anchor, L_sample_mount, H_sample_mount, ...
    L_sample, H_sample);

% Calculate new fab geometry based on fabrication errors derived from
machining
% tolerances and stock material tolerances
% Will apply fabrication error to critical dimensions and will
approximate
% sine errors.

fab.stage.anchor.delta = [0,0,0]';
theta_anchor = [0,0,0];
%sin(err_fab_L(round(rand(1,3)*(trials-1)+1))/H_stage_mount/2);
fab.stage.anchor.theta = [theta_anchor]';

fab.stage.mount.delta = [0,0,0]';
theta_mount = [0,0,0];
%sin(err_fab_L(round(rand(1,3)*(trials-1)+1))/L_stage_mount);
fab.stage.mount.theta = [theta_mount]';

fab.stage.trans.delta = [0 0 0]';
theta_trans = [0,0,0];
% sin(err_fab_L(round(rand(1,3)*(trials-1)+1))/0.125);
fab.stage.trans.theta = [theta_trans]';

fab.carriage.delta = [err_fab_L(round(rand(1,3)*(trials-1)+1))]';

```

```

theta_carriage = [0,0,0];
%sin(err_fab_L(round(rand(1,3)*(trials-1)+1))/0.03);
fab.carriage.theta = [theta_carriage]';

fab.positioner.anchor.delta = [err_fab_L(round(rand(1,3)*(trials-1)+1))]';
theta_positioner = [0,0,0];
%sin(err_fab_L(round(rand(1,3)*(trials-1)+1))/0.076);
fab.positioner.anchor.theta = [theta_positioner]';

fab.positioner.top.delta = [err_fab_L(round(rand(1,3)*(trials-1)+1))]';
fab.positioner.top.theta = [0 0 0]';

fab.endeffect.delta = [0 0 0]';
fab.endeffect.theta = [0 0 0]';

fab.sample.anchor.delta = [0,0,0]';
theta_sample_anchor = [0,0,0];
%sin(err_fab_L(round(rand(1,3)*(trials-1)+1))/H_sample_mount);
fab.sample.anchor.theta = [theta_sample_anchor]';

fab.sample.mount.delta = [err_fab_L(round(rand(1,3)*(trials-1)+1))]';
theta_sample = [0,0,0];
%atan(err_fab_L(round(rand(1,3)*(trials-1)+1))/L_sample_mount);
fab.sample.mount.theta = [theta_sample]';

fab.sample.delta = [0 0 0]';
fab.sample.theta = [0 0 0]';

```

**Function that adjusts the relationship between coordinate systems according to the assembly errors.**

```

function [assem] =
assem_budget(Assem_err_carriage,Assem_err_pos_anchor,...
    Assem_err_pos_top,trials, L_wall_left,H_stage_anchor,...
    L_stage_mount,H_stage_mount,H_trans_stage,H_carriage,
H_pos_base,...
    H_pos_top, L_end_effector, H_end_effector, L_wall_right,...
    H_sample_anchor, L_sample_mount, H_sample_mount,...
    L_sample, H_sample)

% Calculate new assem geometry based on assembly errors derived from
machining
% and waterjet cutting tolerances.
% Will apply specific assembly errors to critical dimensions and will
% approximate sine errors.

assem.stage.anchor.delta = [0,0,0]';

```

```

assem.stage.anchor.theta = [0,0,0]';

assem.stage.mount.delta = [0,0,0]';
assem.stage.mount.theta = [0,0,0]';

assem.stage.trans.delta = [0 0 0]';
assem.stage.trans.theta = [0,0,0]';

assem.carriage.delta = [Assem_err_carriage(round(rand(1,3)*(trials-
1)+1))]';
theta_carriage = [0,0,0];
%sin(Assem_err_carriage(round(rand(1,3)*(trials-1)+1))/0.03);
assem.carriage.theta = [theta_carriage]';

assem.positioner.anchor.delta =
[Assem_err_pos_anchor(round(rand(1,3)...
*(trials-1)+1))]';
theta_positioner = [0,0];
%sin(Assem_err_pos_anchor(round(rand(1,2)*(trials-1)+1))/0.076);
assem.positioner.anchor.theta = [theta_positioner 0]';

assem.positioner.top.delta = [Assem_err_pos_top(round(rand(1,3)...
*(trials-1)+1))]';
theta_positioner_top = [0,0];
%sin(Assem_err_pos_top(round(rand(1,2)*(trials-1)+1))/0.05);
assem.positioner.top.theta = [theta_positioner_top 0]';

assem.endeffect.delta = [0 0 0]';
assem.endeffect.theta = [0 0 0]';

assem.sample.anchor.delta = [0,0,0]';
assem.sample.anchor.theta = [0,0,0]';

assem.sample.mount.delta = [0,0,0]';
assem.sample.mount.theta = [0,0,0]';

assem.sample.delta = [0 0 0]';
assem.sample.theta = [0 0 0]';

```

**Function that generates the new system geometry taking into account the changes due to the three types of error.**

```

function [new_Geom] = new_geom(Geom,thermo,fab,assem)

% Function that adds all the errors to the original ideal Geometry to
% obtain new CS geometry that reflects the errors.
% Input: Geom = ideal geometry
%         thermo = thermal errors
%         fab = fabrication/tolerance errors

```

```

%       assem = assembly errors
%
% Output: new_Geom = CS geomtery that includes possible errors
%       (delta, theta)
%%%%%%%%%%%%%%%%%%%%%%%%%%%%%%%%%%%%%%%%%%%%%%%%%%%%%%%%%%%%%%%%%%%%%%%%
%%%%%%%%

new_Geom.stage.anchor.delta = Geom.stage.anchor.delta + ...
                             thermo.stage.anchor.delta + ...
                             assem.stage.anchor.delta + ...
                             fab.stage.anchor.delta;
new_Geom.stage.anchor.theta = Geom.stage.anchor.theta + ...
                              thermo.stage.anchor.theta + ...
                              assem.stage.anchor.theta + ...
                              fab.stage.anchor.theta;

new_Geom.stage.mount.delta = Geom.stage.mount.delta + ...
                             thermo.stage.mount.delta + ...
                             assem.stage.mount.delta + ...
                             fab.stage.mount.delta;
new_Geom.stage.mount.theta = Geom.stage.mount.theta + ...
                              thermo.stage.mount.theta + ...
                              assem.stage.mount.theta + ...
                              fab.stage.mount.theta;

new_Geom.stage.trans.delta = Geom.stage.trans.delta + ...
                             thermo.stage.trans.delta + ...
                             assem.stage.trans.delta + ...
                             fab.stage.trans.delta;
new_Geom.stage.trans.theta = Geom.stage.trans.theta + ...
                              thermo.stage.trans.theta + ...
                              assem.stage.trans.theta + ...
                              fab.stage.trans.theta;

new_Geom.carriage.delta = Geom.carriage.delta + ...
                          thermo.carriage.delta + ...
                          assem.carriage.delta + ...
                          fab.carriage.delta;
new_Geom.carriage.theta = Geom.carriage.theta + ...
                          thermo.carriage.theta + ...
                          assem.carriage.theta + ...
                          fab.carriage.theta;

new_Geom.positioner.anchor.delta = Geom.positioner.anchor.delta + ...
                                   thermo.positioner.anchor.delta +
...
                                   assem.positioner.anchor.delta +
...
                                   fab.positioner.anchor.delta;
new_Geom.positioner.anchor.theta = Geom.positioner.anchor.theta + ...
                                   thermo.positioner.anchor.theta +

```

```

...
                                assem.positioner.anchor.theta +
...
                                fab.positioner.anchor.theta;

new_Geom.positioner.top.delta = Geom.positioner.top.delta + ...
                                thermo.positioner.top.delta + ...
                                assem.positioner.top.delta + ...
                                fab.positioner.top.delta;
new_Geom.positioner.top.theta = Geom.positioner.top.theta + ...
                                thermo.positioner.top.theta + ...
                                assem.positioner.top.theta + ...
                                fab.positioner.top.theta;

new_Geom.endeffect.delta = Geom.endeffect.delta + ...
                            thermo.endeffect.delta + ...
                            assem.endeffect.delta + ...
                            fab.endeffect.delta;
new_Geom.endeffect.theta = Geom.endeffect.theta + ...
                            thermo.endeffect.theta + ...
                            assem.endeffect.theta + ...
                            fab.endeffect.theta;

new_Geom.sample.anchor.delta = Geom.sample.anchor.delta + ...
                                thermo.sample.anchor.delta + ...
                                assem.sample.anchor.delta + ...
                                fab.sample.anchor.delta;
new_Geom.sample.anchor.theta = Geom.sample.anchor.theta + ...
                                thermo.sample.anchor.theta + ...
                                assem.sample.anchor.theta + ...
                                fab.sample.anchor.theta;

new_Geom.sample.mount.delta = Geom.sample.mount.delta + ...
                                thermo.sample.mount.delta + ...
                                assem.sample.mount.delta + ...
                                fab.sample.mount.delta;
new_Geom.sample.mount.theta = Geom.sample.mount.theta + ...
                                thermo.sample.mount.theta + ...
                                assem.sample.mount.theta + ...
                                fab.sample.mount.theta;

new_Geom.sample.delta = Geom.sample.delta + ...
                        thermo.sample.delta + ...
                        assem.sample.delta + ...
                        fab.sample.delta;
new_Geom.sample.theta = Geom.sample.theta + ...
                        thermo.sample.theta + ...
                        assem.sample.theta + ...
                        fab.sample.theta;

```

**Function that takes new system geometry and calculates the resulting error vector used to calculate translational and rotational displacement due to errors.**

```

function [err_vector] = error_vector(new_Geom)

% Function uses new_new_Geom to create HTMs that include potential
errors
% Input: new_new_Geom = new CS new_Geometry that includes errors
% Output: err_vector = vector from Sample CS to End-effector
%%%%%%%%%%%%%%%%%%%%%%%%%%%%%%%%%%%%%%%%%%%%%%%%%%%%%%%%%%%%%%%%%%%%%%%%
%%%%%%%%%%%%%%%%%%%%%%%%%%%%%%%%%%%%%%%%%%%%%%%%%%%%%%%%%%%%%%%%%%%%%%%%

% Get new_Geom in term of Global CS
htm.stage.anchor = HTM(new_Geom.stage.anchor.theta,...
    new_Geom.stage.anchor.delta);

htm.stage.mount = HTM(new_Geom.stage.mount.theta,...
    new_Geom.stage.mount.delta);

htm.trans = HTM(new_Geom.stage.trans.theta,...
    new_Geom.stage.trans.delta);

htm.carriage = HTM(new_Geom.carriage.theta,...
    new_Geom.carriage.delta);

htm.positioner.anchor = HTM(new_Geom.positioner.anchor.theta,...
    new_Geom.positioner.anchor.delta);

htm.positioner.top = HTM(new_Geom.positioner.top.theta,...
    new_Geom.positioner.top.delta);

htm.endeffect =
HTM(new_Geom.endeffect.theta,new_Geom.endeffect.delta);

[htm.sample.anchor.Fwd,htm.sample.anchor.Rvr] = ...
    HTM(new_Geom.sample.anchor.theta,new_Geom.sample.anchor.delta);

[htm.sample.mount.Fwd,htm.sample.mount.Rvr] = ...
    HTM(new_Geom.sample.mount.theta,new_Geom.sample.mount.delta);

[htm.sample.sample.Fwd,htm.sample.sample.Rvr] = ...
    HTM(new_Geom.sample.theta,new_Geom.sample.delta);

% Map out ideal End-effector CS new_Geometry in Global CS
% End-effector_G Vector = H_G2PosTop*[0 0 H_end_effector]'
End_effect_vect_G = htm.stage.anchor*htm.stage.mount*htm.trans*...
    htm.carriage*htm.positioner.anchor...
    *htm.positioner.top*[new_Geom.endeffect.delta;1];

% Map out ideal End-effector CS new_Geometry in Sample CS
% End-effector_Sam Vector = H_Sample2G*End_effect_vect_G
End_effect_vect_Sam = htm.sample.sample.Rvr*htm.sample.mount.Rvr*...

```



```
    htm.sample.anchor.Rvr*End_effect_vect_G;  
err vector = End effect vect Sam;
```

*This page is intentionally left blank.*

*This page is intentionally left blank.*